

Nonlinear Dynamics in Multimode Optical Waveguide Arrays

Dissertation

zur Erlangung des akademischen Grades
doctor rerum naturalium (Dr. rer. nat.)

vorgelegt dem Rat der Physikalisch-Astronomischen Fakultät
der Friedrich-Schiller-Universität Jena

von Dipl.-Phys. Frank Setzpfandt,
geboren am 31. Oktober 1981 in Oranienburg

Gutachter

1. Prof. Dr. Thomas Pertsch, Friedrich-Schiller-Universität Jena
2. Prof. Dr. Costatino De Angelis, Università di Brescia, Italy
3. Dr. Alain Barthelemy, XLIM Research Institute Limoges, France

Tag der Disputation: 17.08.2012

Contents

1	Introduction	3
1.1	The current state of knowledge	5
1.2	The aim of this thesis	7
2	Basic considerations	10
2.1	The single waveguide	11
2.1.1	Guided modes	12
2.1.2	Dynamics of the mode amplitude	13
2.1.3	Linear perturbations	16
2.1.4	Nonlinear perturbations	16
2.2	Linear dynamics in waveguide arrays	19
2.2.1	The coupling of multimode waveguides	19
2.2.2	Mode mixing effects	20
2.3	Normalized coupled mode equations	22
2.4	Experimental methods	24
2.4.1	Tunable high power light source	24
2.4.2	Optical setup and detection tools	26
3	Second harmonic generation	30
3.1	The isolated waveguide	31
3.1.1	Properties of guided modes	31
3.1.2	Second harmonic generation in a single waveguide	33
3.2	Waveguide arrays	37
3.2.1	Transverse phasematching	39
3.2.2	Second harmonic generation	41
3.2.3	Band characterization	42
4	Multiple mode interactions	48
4.1	Linear propagation of finite beams	49
4.2	Stationary solutions	51
4.2.1	Stationary solutions for single waveguides	53

4.2.2	Discrete spatial solitons	56
4.3	Spatial dynamics	60
4.3.1	Simulations with fundamental wave excitation	61
4.3.2	Experimental realization	64
5	Linearly coupled second harmonic modes	69
5.1	Stationary solutions	71
5.1.1	The structure of the soliton tails	71
5.1.2	Parameter regions for soliton existence	74
5.2	Soliton transition in multimode systems	77
5.2.1	Stationary solutions	78
5.2.2	Experimental demonstration	80
5.3	Spatio-temporal dynamics	86
5.3.1	Simulation of pulse dynamics	87
5.3.2	Experimental demonstration	92
6	Conclusions and Outlook	95
	Bibliography	101
	List of own publications	115
A	Symbols and conventions	120
B	Sample characterization	123
C	Acknowledgements	127
D	Curriculum Vitae	129
E	Ehrenwörtliche Erklärung	130

Chapter 1

Introduction

In this thesis, nonlinear effects of light propagation in waveguide arrays (WGAs) supporting multiple guided modes are studied. Though this topic seems rather specialized, it is rooted in very general concepts which are significant in many branches of physics and other sciences, namely discreteness and nonlinearity. A discrete system consists of several individual elements, which are coupled allowing for the exchange of energy. The properties of the elements are independent of the coupling mechanism, however, the dynamics of an excitation in the system depends on both the individual properties of the elements and their coupling. A simple discrete system is sketched in Fig. 1.1(a), consisting of masses connected by mechanical springs. The second important concept, nonlinearity, describes the nonlinear dependence of one quantity on another. Albeit not always obvious, nonlinearity is part of almost all processes. In most cases the mutual linear dependence of two quantities is merely an approximation, valid only for limited parameter ranges. Examples of discrete nonlinear systems appear in very diverse fields like mechanics [1, 2], solid state physics [3–5], condensed particle physics [6–8], chemistry and biology [9–11], electronics [12], and different branches of optics [13–15]. Since the mathematical description of the various discrete nonlinear phenomena is very similar even for seemingly different systems, effects occurring in one system can often also be confirmed in others. In recent years, optical WGAs have been used frequently as a discrete model system to experimentally verify effects predicted in other discrete systems [16–19]. Using the analogies between WGAs and other systems, also the results of this work may be extrapolated to other fields.

In optical WGAs, several waveguides are placed in a regular grid as shown in Fig. 1.1(b). The proximity between the waveguides allows for the overlap of the evanescent fields of their guided eigenmodes. Thus, energy exchange between the different waveguides is enabled, as shown schematically in Fig. 1.1(c). The WGAs considered in this work consist of waveguides which support several guided modes. These waveguide eigenmodes have different properties and are coupled with different coupling strengths. To conform with the definition of a discrete system, the mode properties have to be

independent of the evanescent coupling. This is approximately fulfilled for weak coupling strengths. Then, light propagation in a WGA can be described with the discrete model of the coupled mode equations [20].

In the discrete model, the eigenmodes of the complete WGA are superpositions of the eigenmodes of all its waveguides. For infinite numbers of waveguides, the eigenvalues of these so-called supermodes form a continuous band. In WGAs, the eigenvalues are the longitudinal wavenumbers of the supermodes, which form a band in dependence on the transverse wavenumbers. These transverse wavenumbers correspond to the phase difference between the oscillations of the modes in the individual waveguides. Each guided mode of the single waveguide forms a separate band in the WGA. If the condition of weak coupling is met, the dynamics of multiple bands can still be described with the coupled mode approach [21, 22], which is not generally the case. A more exact approach to describe the bands of a periodic system is the Floquet-Bloch analysis [23, 24]. The result of the Floquet-Bloch analysis are the Floquet-Bloch modes, which in weakly coupled discrete systems are similar to the supermodes. This method is more general and exact than the coupled mode approach, however, it is not suited to treat nonlinearity and therefore not generally applicable in this thesis.

The optical nonlinearities utilized in this work are a property of the optical media. Because nonlinear optical coefficients are usually very small, optics was considered purely linear for a very long time. The necessary power levels to change this notion became available only after the invention of the laser [25, 26]. The first observed nonlinear optical effect was second-harmonic generation (SHG) [27, 28], the process of doubling the frequency of a laser beam by propagating through a nonlinear medium. Nonlinear coupling between the different frequency components was mediated by the second order nonlinearity of the used crystal. Later, other fast nonlinearities [29, 30] and stronger slow types of nonlinear interactions [31] have been explored as well. Nevertheless, the second order nonlinearity has a very large scientific and industrial relevance. Usually, it is the strongest of the instantaneous types of nonlinearity, allowing for applications like all-optical switching and routing with moderate power levels [32]. Second order

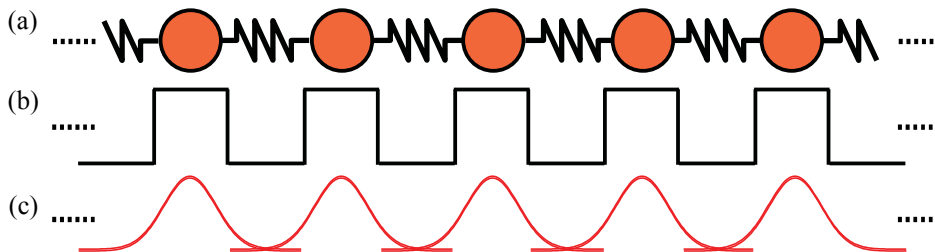


Figure 1.1: (a) Abstract discrete system consisting of masses connected by springs. (b) Refractive index profile of a WGA with (c) field profiles of the waveguide eigenmodes.

processes also allow for the coupling between waves of different frequencies, as in the first nonlinear experiment, which is widely used for the generation of laser light in broad wavelength ranges [33]. The latter advantage makes the second order nonlinearity the prime mechanism considered here. A waveguide mode at a chosen frequency is excited, which then nonlinearly interacts with one or more modes at a different frequency. In WGAs, where the modes at each frequency are also linearly coupled as described above, this corresponds to the exchange of energy between several linear discrete chains by means of a nonlinear coupling mechanism. In this work, wavelengths of around 1500 nm are considered for the initial excitation, which is in the wavelength range used by tele-com applications and hence conveniently available. The nonlinear interaction takes place between modes at this frequency, named the fundamental wave (FW) and modes at the doubled frequency, called second harmonic (SH), with a wavelength of around 750 nm.

In linear WGAs light propagation can sufficiently be described by the supermodes due to the possibility to construct every beam as a superposition of the supermodes. In general, this is not possible in nonlinear systems, since the superposition principle is no longer applicable. Nevertheless, even in the case of nonlinear propagation, stationary solutions are meaningful. They represent the fundamental fixed points of a complicated propagation dynamics that may be attracted by, repelled from or oscillating around the stationary states. In WGAs with quadratic nonlinearity, such stationary solutions can form if FW and SH are phase-locked to each other and travel with the same phase velocity. The simplest stationary solutions are nonlinear discrete plane waves, where the amplitudes of FW and SH components are the linear supermodes. However, more attention is paid to localized stationary solutions, so-called discrete solitons. Here the nonlinearity counteracts the energy spreading induced by linear coupling. Today the term soliton is used in a rather broad context, whereas strictly it applies only to the localized stationary solutions of integrable equations and all others were called solitary waves. The equations considered in this thesis are non-integrable, however, following the informal convention we will equally use both terms when we refer to the stationary solutions. Even if they are no solitons in a strict mathematical sense, the obtained solutions, both here and in the literature, are often rather robust and allow for a deep physical insight into otherwise very complex nonlinear propagation behavior.

1.1 The current state of knowledge

WGAs, in the form of evanescently coupled optical fibers, were first studied theoretically in 1965 [20]. Their first experimental realization was undertaken in 1973 in gallium arsenide [34]. The peculiar linear properties of WGAs have been first considered for their imaging properties [35], the potential to mimic electron transport in

periodic lattices [16], and their ability to alter beam diffraction [36], before a more comprehensive study was undertaken [37]. The linear properties of higher order bands were studied in WGAs consisting of multimode waveguides [38–40]. Recently, the invention of the fs-laser writing technique [41] allowed for a large freedom in the design of longitudinally varying WGAs, resulting in complete control of the linear properties over wide spectral ranges as described in Refs. [18, 42] and references therein.

In the first works on nonlinearity in these systems, the simplest WGA, a two core coupler, was studied theoretically [43, 44]. These studies were driven by the desire to obtain an all-optical switching device and considered an intensity dependent nonlinearity, as was used in the corresponding experiments [45, 46]. WGAs were proposed first in 1988, when the third-order Kerr nonlinearity was predicted to counteract discrete diffraction and thus enable self-focusing [47]. This triggered a flurry of theoretical publications concerning solitons in WGAs with intensity dependent nonlinearities (see e.g. Ref. [48] and references therein). The first experimental realization of discrete solitons was carried out in aluminum-gallium-arsenide WGAs [49–51]. In the view of the topic of this thesis, there are some notable works with third-order nonlinearities where components with different properties interacted to form a discrete soliton. In vector solitons [52–54], two polarization components are mutually locked to form a coherent soliton. However, both components usually stem from the same band and thus have similar properties. Discrete solitons of single higher bands have been excited by angled excitation at the edge of the array [38, 55, 56] with properties qualitatively similar to conventional discrete solitons. Beams from several bands can also form a localized state [57]. Here one beam creates a nonlinear defect, whereas the second component is guided in the created index modulation. The same can be achieved due to incoherent interaction of multicolor beams [58–60].

In materials with second-order nonlinearity, different frequency components are coherently coupled due to the nonlinear interaction. It was shown rather early, that this interaction leads to nonlinear phase shifts due to subsequent frequency mixing processes, so-called cascaded interactions [61–64]. Sign and strength of these phase shifts depend on the sign and magnitude of the phase velocity mismatch between the participating waves. The phase shifts have been considered as a means for all optical manipulation of the FW wave in SHG processes [65–75], which was put to practical realization in the first discrete optical elements, namely nonlinearly tunable two waveguide couplers [32, 76]. In the waveguide couplers, the first order waveguide modes of both FW and SH were employed. However, in 1995 it was noted in a single waveguide, that one guided mode of the FW can interact simultaneously with several SH modes of higher mode order [77].

Already in the 70’s it was reported, that cascading induced phase shifts may enable the generation of spatial solitons [78], which was followed by many theoretical works

about solitons in continuous geometries [70, 79–85]. They showed that spatial solitons could exist for either positive or negative phase velocity mismatch and also for higher-dimensional systems. This was confirmed experimentally in bulk lithium niobate [86, 87] and in film waveguides of the same material [88]. Spatio-temporal solitons, which are localized in space and time, have also been studied extensively for bulk quadratic media. Solutions have been found theoretically both neglecting the group velocity mismatch (GVM) of the propagating pulses [79, 89–92] and taking it into account [93–98]. Experimentally, these studies have been confirmed for fs pulses [99].

In WGAs with quadratic nonlinearity, spatial solitons were first predicted in Ref. [100] and studied in more detail in Refs. [22, 101–103] for one component of FW and SH, respectively. It was shown that these solitons can exist for propagation constants in the gaps above and below the linear bands [101, 104]. These predictions were verified experimentally in lithium niobate WGAs [105, 106]. Also the existence of spatio-temporal solitons in WGAs with second-order nonlinearity was reported [107, 108], however, without experimental verification up to now.

Commonly, discrete solitons in WGAs are classified by two schemes. First, they are distinguished based on the symmetry of their intensity distributions. Odd solitons have their intensity maximum at the central waveguide, whereas even solitons have the same intensity in the two centering waveguides. Generally, the difference in the Hamiltonian of these two kinds of solutions, the Peierls-Nabarro-barrier, prevents solitons from moving in the transverse direction [109, 110]. The second classification is according to the phase profile of the solitons. If all excited waveguides have the same phase, the solitons are called unstaggered, in contrast to staggered solitons, where the phase difference between adjacent waveguides is always π . For the solitons considered in the literature, this classification is determined by the FW wave. Additionally, also the individual waves in any SHG process can be termed staggered or unstaggered, depending on their phase profile. Other, more complicated soliton profiles not described by the mentioned classifications include front [111] and twisted [112] solitons.

As can be seen, the topic of this thesis originates from a well developed field of optical sciences. Hence, a number of review articles already exist, where different subtopics are conveniently summarized, e.g. on solitons and other effects with second order nonlinearities [113, 114], discrete optics in WGAs [19, 42], and discrete solitons [48, 115–118].

1.2 The aim of this thesis

All experimental studies on channel waveguides or WGAs with second order nonlinearity have utilized the fundamental guided modes of both frequency components, with the notable exception being Ref. [77]. The latter work showed, that the first guided

FW mode can interact with several SH modes with higher mode order, and that these interactions take place simultaneously, influencing each other in dependence on the input power. However, this study used only a single waveguide, thus was not able to reveal new spatial effects. In the present thesis the interaction of an FW mode with higher order SH modes and its ramifications on nonlinear propagation in WGAs are studied. A special focus is put on the existence and properties of spatial discrete solitons as the limiting case for nonlinear propagation. Furthermore, nonlinear dynamics is investigated in conjunction with experimental works to explore the practical realization of the theoretical results.

Taking into account higher order SH modes leads to considerable changes in the investigated nonlinear discrete system, compared to the case of only the first SH mode studied experimentally before. The linear properties in the individual waveguides are different, since the propagation constants of higher order modes differ from that of the first order mode. Additionally, the coupling properties of the WGA change, since the evanescent field overlap of the higher order modes is usually much larger than for the first order mode. This leads to increased energy exchange between different waveguides which is especially significant for the SH modes, since the first order SH mode shows no linear coupling for experimentally available sample lengths. Due to different mode shapes of the SH modes also the nonlinear coupling strength between FW and SH modes in each waveguide depends on the SH mode order. In WGAs, where the use of the first order SH modes yielded only nonlinear effects comparable to that encountered in systems with Kerr-nonlinearity, the utilization of linearly coupled SH modes in nonlinear interactions can qualitatively change the nature of the observed effects. Finally, the use of higher order SH modes implies the existence of several modes. This introduces different pairs of nonlinear interactions, adding a new degree of freedom not possible in systems which are limited to the first SH mode. All these consequences of the participation of higher order SH modes in discrete nonlinear propagation are investigated in this work. Resulting effects are studied both theoretically and experimentally. The mathematical foundations and the experimental tools to undertake these studies in discrete WGAs with several modes are developed in Chapter 2.

The best known nonlinear effect in optical systems with quadratic nonlinearity is SHG, which also takes place in WGAs [119]. Hence, it is natural to study the effects of higher order SH modes on the generation of SH. Investigations of SHG are conducted in Chapter 3 with a focus on the dependence of the phasematching on the mode properties. The investigations are restricted to the case of low input powers and plane wave excitations to avoid spatial effects and high power interplay between different SH modes [77]. The results of the studies on SHG lead to a convenient method for the experimental characterization of the higher order SH modes under test.

Nonlinear propagation in WGAs with several SH modes is discussed in Chapter 4.

Already in Ref. [77] the simultaneous interaction of an FW mode with different SH modes was studied. The authors concluded, that all FW-SH interactions induce phase shifts. Due to the nature of quadratic nonlinear interactions the induced phase shifts may have different signs, depending on the frequencies of the participating optical signals. This opens up the possibility to utilize SH processes with the same or opposite signs of the induced phase shifts, thus having co- or counter-acting nonlinear interactions. In this work, the spatial effects triggered by these different phase shifts in finite beams are explored. First, discrete quadratic solitons are studied theoretically in WGAs with two SH modes and the unique effects caused by the multimode SH are displayed. The results of these studies are used to explain dynamic beam propagation in the experiment.

The influence of the distinct properties of the higher order SH modes is investigated in Chapter 5. Again, spatial solitons are discussed, with a focus on the topology of the propagating waves in dependence on the SH mode properties. A distinct transition of the soliton topology caused by the interplay of beam localization and synchronization of the parametrically interacting waves is described. This effect, which is possible only with higher order SH modes, is demonstrated experimentally. To further analyze the experimental findings, a thorough analysis of spatio-temporal beam dynamics is conducted. This allows for the identification of pulse reshaping effects leading to the occurrence of the topology transition also in the non-stationary experimental environment.

The thesis is closed with a summary of its main findings in Chapter 6. The impact of the results of this work is discussed and further research directions are disclosed.

In the appendix an overview of specific methods to characterize the samples used in the experiments is given.

The present thesis is the result of a close collaboration with Dr. Dragomir N. Neshev and Dr. Andrey A. Sukhorukov from the Australian National University, Canberra and Prof. Roland Schiek from the Fachhochschule Regensburg who helped in finding ideas, with the theoretical part of the work and performing the experiments. The samples used in all experiments during this thesis were developed and fabricated by Prof. Wolfgang Sohler and his co-workers at the University of Paderborn.

Chapter 2

Basic considerations

In this thesis, the propagation of higher order modes in nonlinear WGAs is studied in two different ways. First, possible new effects should be identified theoretically, which requires a simplified mathematical model allowing for analytical treatment. Later, the theoretical predictions are verified experimentally. Besides a suitable experimental apparatus, this also calls for a model taking into account all impacting effects to accurately simulate and control the experiment. This requirement can be achieved, if the mathematical description starts from a physical model of the system, allowing to take into account all necessary effects.

These two seemingly conflicting demands on a model can be fulfilled with the well known coupled-mode formalism [120–125]. Here each waveguide mode in each waveguide taking part in the interactions is represented by a separate equation, where all physical effects are described by separate terms either coupling the different equations or acting on just one. This enables the sought after flexibility, allowing for inclusion or neglect of terms, and hence physical effects, according to the experimental needs or mathematical possibilities.

In this chapter a concise derivation of the used coupled mode equations will be given, to show how the resulting formulas originate from physical notions. The derivation closely follows Ref. [126] but includes multiple waveguide eigenmodes. In Section 2.1 light propagation in a single waveguide is treated, where local linear and nonlinear effects are explained. Section 2.2 is devoted to interactions between the neighboring waveguides in the array. Here especially the additional assumptions necessary to describe multimode waveguides with the coupled mode theory are explained. Section 2.3 deals with the complete set of equations, describing the normalizations used in the theoretical part of this work. Finally, an experimental scheme developed to study light propagation described by the derived set of equations is presented in Section 2.4.

2.1 The single waveguide

We will start our discussion with the vector wave equation for source-free dielectric media

$$\text{rot rot } \tilde{\mathbf{E}}(\mathbf{r}, \omega) - \omega^2 \varepsilon_0 \mu_0 \tilde{\mathbf{E}}(\mathbf{r}, \omega) = \mu_0 \omega^2 \tilde{\mathbf{P}}(\mathbf{r}, \omega), \quad (2.1)$$

which can be easily derived from Maxwell's equations [127]. Here \mathbf{r} is the coordinate vector in space, ω the angular frequency, $\tilde{\mathbf{E}}$ and $\tilde{\mathbf{H}}$ the electric and magnetic field vectors, $\tilde{\mathbf{P}}$ the polarization, and ε_0 and μ_0 the dielectric constant and magnetic permeability of vacuum. The vector fields in frequency space, as used in Eq. (2.1), are connected to the fields in real space by a Fourier transform, given here for the electric field as an example

$$\mathbf{E}(\mathbf{r}, t) = \int_{-\infty}^{\infty} \tilde{\mathbf{E}}(\mathbf{r}, \omega) \exp(-i\omega t) d\omega; \quad \tilde{\mathbf{E}}(\mathbf{r}, \omega) = \frac{1}{2\pi} \int_{-\infty}^{\infty} \mathbf{E}(\mathbf{r}, t) \exp(i\omega t) dt. \quad (2.2)$$

The interaction of an electric field $\tilde{\mathbf{E}}(\mathbf{r}, \omega)$ with a dielectric medium is mediated by the polarization $\tilde{\mathbf{P}}(\mathbf{r}, \omega)$. For optical frequencies far from transition frequencies of the atoms or molecules the medium consists of, the polarization can be written as a series [30]

$$\tilde{\mathbf{P}}(\mathbf{r}, \omega) = \sum_{n=1}^{\infty} \tilde{\mathbf{P}}^{(n)}(\mathbf{r}, \omega). \quad (2.3)$$

The n th element in this series is proportional to the n th power of the electric field. This thesis will only be concerned with the first two elements of the series Eq. (2.3). Additionally, it is assumed that the considered media have only a local response, which is important for the actual form of the polarization terms [30]. The first element of the series describes the linear anisotropic response of the material to low intensity electric fields by a complex second rank tensor, $\tilde{\mathbf{P}}^{(1)}(\mathbf{r}, \omega) = \varepsilon_0 \hat{\chi}(\mathbf{r}, -\omega; \omega) \tilde{\mathbf{E}}(\mathbf{r}, \omega)$. The two frequency arguments of the susceptibility tensor $\hat{\chi}(\mathbf{r}, -\omega; \omega)$ denote the frequencies of the polarization and the driving electric field. In the linear case these frequencies have to be the same to fulfill energy conservation. Hence we use a simplified notation with only one frequency argument. Usually, the susceptibility is expressed in terms of the dielectric function $\hat{\varepsilon}(\mathbf{r}, \omega) = 1 + \hat{\chi}(\mathbf{r}, \omega)$. The important higher order polarization term will be discussed in Section 2.1.4.

Up to now no assumptions strongly limiting the generality of Eq. (2.1) have been proposed. However, to arrive at a description which can be actually analyzed with respect to certain experimental situations, some simplifications are necessary and justified.

First, for transparent dielectric materials and non-resonant nonlinear processes as discussed here, the 2nd order susceptibility $\tilde{\mathbf{P}}^{(2)}(\mathbf{r}, \omega)$ is much smaller than the linear

spatial inhomogeneity $\Delta\hat{\epsilon}(\mathbf{r}, \omega)$, which defines the waveguides and is part of $\tilde{\mathbf{P}}^{(1)}(\mathbf{r}, \omega)$. Hence the nonlinear effects are a minor influence, which can be treated later by a perturbation theory.

Also, the waveguides of the array are weakly coupled, meaning fields in one waveguide are only weakly influenced by the $\Delta\hat{\epsilon}(\mathbf{r}, \omega)$ distributions of neighboring waveguides. Furthermore, linear losses in all waveguides are assumed to be small. Hence we can treat the generally complex tensor $\hat{\epsilon}(\mathbf{r}, \omega)$ as real.

Finally, we propose that the waveguides are essentially translational invariant in the longitudinal z-direction, $\Delta\hat{\epsilon}(\mathbf{r}, \omega) = \Delta\hat{\epsilon}(x, y, \omega)$. This enables the propagation of guided modes in the z-direction.

The assumptions described above allow for the separation of the properties of a guided mode of a single waveguide from all other effects in the system. The guided modes are then determined by the real-valued, z-independent tensor $\hat{\epsilon}(x, y, \omega)$, which describes the profile of one waveguide and induces the polarization $\tilde{\mathbf{P}}(\mathbf{r}, \omega) = \epsilon_0 [\hat{\epsilon}(x, y, \omega) - 1] \tilde{\mathbf{E}}(\mathbf{r}, \omega)$. In the next section the propagation equation Eq. (2.1) will be solved for the linear guided modes. The influence of linear inhomogeneities, losses, and nonlinear polarizations will later be treated within a perturbation theory as additional polarization components $\Delta\tilde{\mathbf{P}}(\mathbf{r}, \omega)$. However, these perturbations do not change the linear mode properties.

2.1.1 Guided modes

The wave equation for a homogeneous linear waveguide reads like

$$\text{rot rot } \tilde{\mathbf{E}}(\mathbf{r}, \omega) - \omega^2 \epsilon_0 \mu_0 \hat{\epsilon}(x, y, \omega) \tilde{\mathbf{E}}(\mathbf{r}, \omega) = 0. \quad (2.4)$$

Eigenmodes of this equation have the form

$$\tilde{\mathbf{E}}(\mathbf{r}, \omega) = \mathbf{e}^\mu(x, y, \omega) \exp[i\beta^\mu(\omega)z]. \quad (2.5)$$

The insertion of Eq. (2.5) into Eq. (2.4) leads to a generalized eigenvalue problem for the waveguide modes $\mathbf{e}^\mu(x, y, \omega)$ as eigenfunctions and the propagation constants $\beta^\mu(\omega)$ as eigenvalues. In general, this eigenvalue problem has to be solved numerically, although approximate analytical solutions exist for some waveguides with circular [128] or step index profiles [129]. Numerical solutions for the waveguides investigated in this thesis are presented in Section 3.1 of Chapter 3. To obtain these solutions, the Finite Element method [130, 131] and the Plane Wave Expansion method [132] have been used in this thesis.

All eigenmodes of a given dielectric waveguide fulfill the orthogonality relation

$$\int_{-\infty}^{\infty} \int_{-\infty}^{\infty} [\mathbf{e}_t^\mu(x, y, \omega) \times \mathbf{h}_t^{\mu*}(x, y, \omega)] \mathbf{z} dx dy = 0, \quad (2.6)$$

with t denoting the transverse components of the electric field \mathbf{e}^μ and the magnetic field \mathbf{h}^μ . The asterisk $*$ denotes the complex conjugate. Additionally, all eigenmodes are assumed to be normalized like

$$\frac{1}{2} \Re \left[\int_{-\infty}^{\infty} \int_{-\infty}^{\infty} [\mathbf{e}_t^\mu(x, y, \omega) \times \mathbf{h}_t^{\mu*}(x, y, \omega)] \mathbf{z} dx dy \right] = P_0 = 1 \text{ W}, \quad (2.7)$$

which simplifies the following equations.

In the unperturbed waveguide the derived modes propagate without change. However, a longitudinal dynamics, reviewed in the next section, is introduced by virtue of the small perturbations described in the initial assumption of Section 2.1.

2.1.2 Dynamics of the mode amplitude

The derivation of the propagation dynamics starts from a harmonic wave of a single mode μ

$$\mathbf{E}(\mathbf{r}, t) = \frac{1}{2} \tilde{\varphi}^\mu(z, \omega) \mathbf{e}^\mu(x, y, \omega) \exp(-i\omega t) + \text{c.c.}, \quad (2.8)$$

where the mode profile $\mathbf{e}^\mu(x, y, \omega)$ is constant along z . In experiments, the amplitude $\tilde{\varphi}^\mu(z=0, \omega)$ is determined by the transverse part of the exciting magnetic field $\tilde{\mathbf{H}}_t^{\text{ext}}$ via the overlap integral

$$\tilde{\varphi}^\mu(z=0, \omega) = \frac{1}{2P_0} \int_{-\infty}^{\infty} \int_{-\infty}^{\infty} [\mathbf{e}_t^{\mu*}(x, y) \times \tilde{\mathbf{H}}_t^{\text{ext}}(x, y, z=0, \omega)] \mathbf{z} dx dy. \quad (2.9)$$

In the unperturbed waveguide, only the phase of the mode amplitude evolves harmonically with $\tilde{\varphi}^\mu(z, \omega) = \tilde{\varphi}^\mu(0, \omega) \exp[i\beta^\mu(\omega)z]$. However, this changes when a small perturbing polarization $\Delta\tilde{\mathbf{P}}(\mathbf{r}, \omega)$ induces longitudinal dynamics. Here we will utilize perturbation theory, in particular making use of the reciprocal theorem, to describe the dynamics of the modal amplitude $\tilde{\varphi}^\mu(z, \omega)$ in dependence on $\Delta\tilde{\mathbf{P}}(\mathbf{r}, \omega)$ [133, 134].

The derivation starts from the field of an unperturbed waveguide $\tilde{\mathbf{E}}_1(\mathbf{r}, \omega)$ and the field $\tilde{\mathbf{E}}_2(\mathbf{r}, \omega)$ of a waveguide subject to a small perturbation $\Delta\tilde{\mathbf{P}}(\mathbf{r}, \omega)$. Both fields

have to fulfill Maxwell's equations

$$\text{rot } \tilde{\mathbf{E}}_1 = i\omega\mu_0\tilde{\mathbf{H}}_1 \quad (2.10)$$

$$\text{rot } \tilde{\mathbf{H}}_1 = -i\omega\varepsilon_0\hat{\varepsilon}\tilde{\mathbf{E}}_1 \quad (2.11)$$

$$\text{rot } \tilde{\mathbf{E}}_2 = i\omega\mu_0\tilde{\mathbf{H}}_2 \quad (2.12)$$

$$\text{rot } \tilde{\mathbf{H}}_2 = -i\omega\left(\varepsilon_0\hat{\varepsilon}\tilde{\mathbf{E}}_2 + \Delta\tilde{\mathbf{P}}\right). \quad (2.13)$$

Now we subtract the complex conjugate of Eq. (2.11), multiplied by $\tilde{\mathbf{E}}_2$ from Eq. (2.12) multiplied by $\tilde{\mathbf{H}}_1^*$ and arrive at

$$\text{div}\left(\tilde{\mathbf{E}}_2 \times \tilde{\mathbf{H}}_1^*\right) = i\omega\left(\mu_0\tilde{\mathbf{H}}_2\tilde{\mathbf{H}}_1^* - \varepsilon_0\hat{\varepsilon}\tilde{\mathbf{E}}_2\tilde{\mathbf{E}}_1^*\right). \quad (2.14)$$

Similarly we subtract the complex conjugate of Eq. (2.10) multiplied by $\tilde{\mathbf{H}}_2$ from Eq. (2.13) multiplied by $\tilde{\mathbf{E}}_1^*$. The latter result is subtracted from Eq. (2.14) and we obtain

$$\text{div}\left(\tilde{\mathbf{E}}_2 \times \tilde{\mathbf{H}}_1^* + \tilde{\mathbf{E}}_1^* \times \tilde{\mathbf{H}}_2\right) = i\omega\tilde{\mathbf{E}}_1^*\Delta\tilde{\mathbf{P}}. \quad (2.15)$$

Integrating over the transverse cross section of Eq. (2.15) yields

$$\begin{aligned} & \int_{-\infty}^{\infty} \int_{-\infty}^{\infty} \nabla_t \cdot \left(\tilde{\mathbf{E}}_2 \times \tilde{\mathbf{H}}_1^* + \tilde{\mathbf{E}}_1^* \times \tilde{\mathbf{H}}_2\right)_t dx dy + \\ & \int_{-\infty}^{\infty} \int_{-\infty}^{\infty} \frac{\partial}{\partial z} \left(\tilde{\mathbf{E}}_2 \times \tilde{\mathbf{H}}_1^* + \tilde{\mathbf{E}}_1^* \times \tilde{\mathbf{H}}_2\right)_z dx dy = i\omega \int_{-\infty}^{\infty} \int_{-\infty}^{\infty} \tilde{\mathbf{E}}_1^* \Delta\tilde{\mathbf{P}} dx dy, \end{aligned} \quad (2.16)$$

where the first integral can be transformed into a line integral at infinity using Gauss's law and thus vanishes.

The unperturbed field is now assumed to propagate in the guided mode μ

$$\tilde{\mathbf{E}}_1(\mathbf{r}, \omega) = \mathbf{e}^\mu(x, y, \omega) \exp[i\beta^\mu(\omega)z], \quad \tilde{\mathbf{H}}_1(\mathbf{r}, \omega) = \mathbf{h}^\mu(x, y, \omega) \exp[i\beta^\mu(\omega)z]. \quad (2.17)$$

In contrast to this the perturbed field may consist of several modes,

$$\tilde{\mathbf{E}}_2(\mathbf{r}, \omega) = \sum_{\mu'} \tilde{\varphi}^{\mu'} \mathbf{e}^{\mu'}(x, y, \omega), \quad \tilde{\mathbf{H}}_2(\mathbf{r}, \omega) = \sum_{\mu'} \tilde{\varphi}^{\mu'} \mathbf{h}^{\mu'}(x, y, \omega). \quad (2.18)$$

Here only forward propagating modes are taken into account since we assume that the polarization $\Delta\tilde{\mathbf{P}}(\mathbf{r}, \omega)$ does not couple modes of different propagation directions. Taking into account the orthogonality relation Eq. (2.6) and the mode normalization Eq. (2.7), the integration of the remaining left side term of Eq. (2.16) can be carried out. We arrive at an equation describing the evolution of the amplitude of mode μ

$$\left[\frac{\partial}{\partial z} - i\beta^\mu(\omega) \right] \tilde{\varphi}^\mu(z, \omega) = \frac{i\omega}{4P_0} \int_{-\infty}^{\infty} \int_{-\infty}^{\infty} \mathbf{e}^{\mu*}(x, y, \omega) \Delta \tilde{\mathbf{P}}(\mathbf{r}, \omega) dx dy. \quad (2.19)$$

This equation takes into account the dispersion of the mode's propagation constant across the whole spectral range. However, the assumption of a constant mode profile cannot be sustained for largely different frequencies. Thus, the applicability of Eq. (2.19) is limited to excitations with small spectral width $\Delta\omega$, where the modal field can be considered frequency independent, $\mathbf{e}_0^\mu(x, y) = \mathbf{e}^\mu(x, y, \omega_0)$. Here $\omega_0 \gg \Delta\omega$ is the center frequency of the signal spectrum. Assuming a smooth variation, the propagation constant $\beta^\mu(\omega)$ can be written as a Taylor expansion for frequencies close to ω_0

$$\beta^\mu(\omega) \approx \beta_0^\mu + \frac{1}{v_g^\mu} (\omega - \omega_0) + \frac{D^\mu}{2} (\omega - \omega_0)^2. \quad (2.20)$$

where v_g^μ is the group velocity and D^μ the group velocity dispersion (GVD) of the mode μ . The coefficients in Eq. (2.20) are determined by

$$\beta_0^\mu = \beta^\mu(\omega_0), \quad \frac{1}{v_g^\mu} = \left. \frac{d\beta^\mu}{d\omega} \right|_{\omega_0}, \quad \text{and} \quad D^\mu = \left. \frac{d^2\beta^\mu}{d\omega^2} \right|_{\omega_0}. \quad (2.21)$$

Additionally, all frequency arguments ω in Eq. (2.19) are fixed to ω_0 . Thus, the dispersion of the induced polarization term $\Delta \mathbf{P}$ is neglected, assuming an instantaneous response. The effects induced by the perturbing polarizations are determined only at ω_0 . Now an inverse Fourier transformation of Eq. (2.19) can be performed. If we finally assume that the temporal change of the field envelope is slow compared to the fast phase oscillation of the carrier wave, the fast phase term $\exp(i\beta_0^\mu z - i\omega_0 t)$ can be eliminated, which is the well known slowly varying envelope approximation [135]. Thus, we arrive at a propagation equation for the slowly varying amplitude $u^\mu(z, t) = \varphi(z, t) \exp(-i\beta_0^\mu z)$ of the waveguide mode

$$\left[i \frac{\partial}{\partial z} + \frac{i}{v_g^\mu} \frac{\partial}{\partial t} - \frac{D^\mu}{2} \frac{\partial^2}{\partial t^2} \right] u^\mu(z, t) = -\frac{\omega_0}{4P_0} \int_{-\infty}^{\infty} \int_{-\infty}^{\infty} \mathbf{e}_0^{\mu*}(x, y) \Delta \bar{\mathbf{P}}(\mathbf{r}, t) dx dy \exp(-i\beta_0^\mu z). \quad (2.22)$$

Here $\Delta \bar{\mathbf{P}}(\mathbf{r}, t)$ is the slowly varying envelope of the polarization in the time domain, $\Delta \mathbf{P}(\mathbf{r}, t) = \frac{1}{2} \Delta \bar{\mathbf{P}}(\mathbf{r}, t) \exp(-i\omega_0 t) + \text{c.c.}$.

Since all perturbing polarizations are small and do not strongly change the properties of the waveguide modes, the linear and nonlinear local perturbations or nonlocal perturbations from other waveguides act independently. Hence, in the further treatment they can be linearly superimposed. Terms in the coupled mode equations resulting from these perturbations can be taken into account or be neglected without affecting the validity of other terms.

2.1.3 Linear perturbations

Linear perturbations acting only locally on one waveguide are introduced through changes in the distribution of the dielectric function defining a waveguide, $\Delta\hat{\epsilon}(\mathbf{r})$. These, generally complex, inhomogeneities result in the local polarization

$$\Delta\mathbf{P}^{\text{linear}} = \frac{1}{2}\varepsilon_0\Delta\hat{\epsilon}(\mathbf{r})u^\mu(z,t)\mathbf{e}_0^\mu(x,y)\exp(i\beta_0^\mu z - i\omega_0 t) + \text{c.c.}, \quad (2.23)$$

which results in the propagation equation

$$\left[i\frac{\partial}{\partial z} + \frac{i}{v_g^\mu}\frac{\partial}{\partial t} - \frac{D^\mu}{2}\frac{\partial^2}{\partial t^2} + \Delta\beta_{\text{lin}}^\mu(z) + i\frac{\alpha^\mu}{2} \right] u^\mu(z,t) = 0, \quad (2.24)$$

obtained by splitting $\Delta\hat{\epsilon}(\mathbf{r})$ into real and imaginary parts. The coefficients $\Delta\beta_{\text{lin}}^\mu(z)$ and $\alpha^\mu(z)$ are defined as

$$\begin{aligned} \Delta\beta_{\text{lin}}^\mu(z) &= \frac{\omega_0\varepsilon_0}{4P_0} \int_{-\infty}^{\infty} \int_{-\infty}^{\infty} \Re[\Delta\hat{\epsilon}(\mathbf{r})] \mathbf{e}_0^{\mu*}(x,y)\mathbf{e}_0^\mu(x,y) dx dy, \\ \alpha^\mu(z) &= \frac{2\omega_0\varepsilon_0}{4P_0} \int_{-\infty}^{\infty} \int_{-\infty}^{\infty} \Im[\Delta\hat{\epsilon}(\mathbf{r})] \mathbf{e}_0^{\mu*}(x,y)\mathbf{e}_0^\mu(x,y) dx dy. \end{aligned} \quad (2.25)$$

The physical meaning of $\Delta\beta_{\text{lin}}^\mu(z)$ is a local detuning of the propagation constant, whereas $\alpha^\mu(z)$ describes the linear loss of the waveguide.

2.1.4 Nonlinear perturbations

The higher order polarization terms in the expansion Eq. (2.3) also contribute to the locally perturbing polarizations. In this thesis only the effect of the quadratic term is considered. This and all other even terms exist only in media not possessing inversion symmetry, like the lithium niobate crystals used to manufacture the samples investigated here. The i th vector component of the 2nd order polarization term depends on the electric field like

$$\tilde{\mathbf{P}}_i^{(2)}(\mathbf{r},\omega) = \varepsilon_0 \sum_{\theta_1,\theta_2} \int_{-\infty}^{\infty} \int_{-\infty}^{\infty} \hat{\chi}_{i\theta_1\theta_2}^{(2)}(\mathbf{r},-\omega^\sigma;\omega^1\omega^2) \tilde{\mathbf{E}}_{\theta_1}(\mathbf{r},\omega^1) \tilde{\mathbf{E}}_{\theta_2}(\mathbf{r},\omega^2) \delta(\omega - \omega^\sigma) d\omega^1 d\omega^2, \quad (2.26)$$

where the 2nd order susceptibility tensor couples three fields of different frequencies and polarizations [30]. However, the frequencies have to obey energy conservation, expressed by the δ -term in Eq. (2.26) which demands $\omega^\sigma = \omega^1 + \omega^2$. This also follows from the Manley-Rowe-relations [136]. Here only two frequencies are considered, a low

frequency fundamental wave (FW) and a high frequency second harmonic (SH), which have to obey

$$\omega^{\text{SH}} = 2\omega^{\text{FW}}. \quad (2.27)$$

In general, the two FW fields may stem from two different waveguide modes. In the following, interactions where both FW fields are propagating in the same mode are called degenerate interactions, in contrast to non-degenerate interactions with two different FW modes. We note, that in other works the distinction between degenerate and non-degenerate interactions is usually based on the frequencies of the long wavelength photons, which are always the same here. Since we consider just one particular experimental system, we can make another simplification without losing the validity of our approach. In lithium niobate, the largest coefficient of the $\hat{\chi}^{(2)}$ tensor is $\chi_{333}^{(2)}$, coupling the electric field components polarized along the crystal's optical axis [137]. At a wavelength of $1.55 \mu\text{m}$ this coefficient is $\chi_{333}^{(2)} = -20.6 \frac{\text{pm}}{\text{V}}$ [138]. In the coordinate system used here, the optical axis of the crystal is directed along the y -direction. Since the used samples are designed to only utilize the $\chi_{333}^{(2)}$ coefficient, the mathematical description will be restricted to the y -components of the electric field and polarization. Consequently, all fields will be considered only as scalar variables in the following.

However, not only the magnitude of the susceptibility dictates the efficiency of 2nd order nonlinear processes. Since two field components with vastly different frequencies interact, a matching of the phase velocity of all participating components is necessary. To achieve this, several techniques are available, e.g. birefringent phasematching [139] and quasi-phasematching (QPM) [28] by periodic poling of the crystal structure [140]. The latter method is employed here, since it enables the use of the $\chi_{333}^{(2)}$ coefficient. In a periodically poled sample the optical axis of the crystal is flipped periodically with the period Λ^{QPM} along the light propagation direction. In each of this alternating domains the susceptibility is either $\chi_{333}^{(2)}$ or $-\chi_{333}^{(2)}$. To deal with this rectangular grid mathematically, it is expanded into a Fourier series and we keep only the first order terms

$$\chi(z) = \pm\chi_{333}^{(2)} \approx \frac{2}{\pi}\chi_{333}^{(2)} \left(\exp\left(i\frac{2\pi}{\Lambda^{\text{QPM}}}z\right) + \exp\left(-i\frac{2\pi}{\Lambda^{\text{QPM}}}z\right) \right). \quad (2.28)$$

Taking into account also higher order terms has been discussed elsewhere [141–143] and it was shown that they may have the same effect as higher order nonlinear polarizations of the series Eq. (2.3). However, the impact of these terms is restricted to special parameter ranges and generally much smaller than the first order QPM term.

The electric field in the waveguide can be written as a superposition of all modes

propagating at the two frequencies taken into account

$$E_y = \sum_{\mu} \frac{1}{2} [u^{\mu} e_0^{\mu} \exp(i\beta_0^{\mu} z - i\omega_0^{\mu} t) + \text{c.c.}] \quad (2.29)$$

Then, according to Eq. (2.26) the y -component of the induced polarization reads like

$$P_y^{(2)} = \varepsilon_0 \sum_{\mu, \mu'} \chi_{333}^{(2)}(-\omega_{\sigma}; \omega_0^{\mu}, \omega_0^{\mu'}) \left[\frac{1}{2} u^{\mu} e_0^{\mu} e^{(i\beta_0^{\mu} z - i\omega_0^{\mu} t)} + \text{c.c.} \right] \left[\frac{1}{2} u^{\mu'} e_0^{\mu'} e^{(i\beta_0^{\mu'} z - i\omega_0^{\mu'} t)} + \text{c.c.} \right], \quad (2.30)$$

where μ and μ' are running over all modes at all frequencies [30]. Using this polarization as the perturbing polarization in Eq. (2.22), a system of coupled mode equations for the amplitudes of several FW and SH modes propagating together is obtained, which for the FW mode ξ and the SH mode ν is

$$\begin{aligned} \left(i \frac{\partial}{\partial z} + \frac{i}{v_g^{\xi}} \frac{\partial}{\partial t} - \frac{D^{\xi}}{2} \frac{\partial^2}{\partial t^2} \right) u^{\xi} &= -\omega_0^{\text{FW}} \sum_{\xi'} \sum_{\nu'} \chi_{\text{eff}}^{\nu' \xi \xi'} u^{\nu'*} u^{\nu'} \exp[-i\Delta\beta^{\nu' \xi \xi'} z], \\ \left(i \frac{\partial}{\partial z} + \frac{i}{v_g^{\nu}} \frac{\partial}{\partial t} - \frac{D^{\nu}}{2} \frac{\partial^2}{\partial t^2} \right) u^{\nu} &= -\omega_0^{\text{FW}} \sum_{\xi' \xi''} \chi_{\text{eff}}^{\nu \xi' \xi''} u^{\xi'} u^{\xi''} \exp[i\Delta\beta^{\nu \xi' \xi''} z]. \end{aligned} \quad (2.31)$$

Here the ξ' and ξ'' are running over all modes at the FW frequency, whereas ν' denotes modes at the SH frequency. The phase mismatch between interacting modes is determined by

$$\Delta\beta^{\nu \xi \xi'} = \beta_0^{\xi} + \beta_0^{\xi'} - \beta_0^{\nu} + \frac{2\pi}{\Lambda_{\text{QPM}}} \quad (2.32)$$

and the strength of the nonlinear interaction is given by the effective susceptibility

$$\chi_{\text{eff}}^{\nu \xi \xi'} = \frac{\varepsilon_0}{2\pi P_0} \int_{-\infty}^{\infty} \int_{-\infty}^{\infty} \chi_{333}^{(2)} e_0^{\nu} e_0^{\xi*} e_0^{\xi'*} dx dy. \quad (2.33)$$

In the propagation equations Eqs. (2.31) the power is conserved as

$$P = \sum_{\mu} \int_{-\infty}^{\infty} |u^{\mu}(z, t)|^2 dt = \sum_{\xi} \int_{-\infty}^{\infty} |u^{\xi}(z, t)|^2 dt + \sum_{\nu} \int_{-\infty}^{\infty} |u^{\nu}(z, t)|^2 dt. \quad (2.34)$$

In most of the available waveguides and WGAs only one guided FW mode exists, whereas at the SH frequency always several modes are guided. In this case the nonlinear interaction is always degenerated, i.e. both FW fields are propagating in the same mode

denoted by the index FW. This allows to simplify Eqs. (2.31) to

$$\begin{aligned} \left(i \frac{\partial}{\partial z} + \frac{i}{v_g^{\text{FW}}} \frac{\partial}{\partial t} - \frac{D^{\text{FW}}}{2} \frac{\partial^2}{\partial t^2} \right) u^{\text{FW}} &= -\omega_0^{\text{FW}} \sum_{\nu'} \chi_{\text{eff}}^{\nu'} u^{\text{FW}*} u^{\nu'} \exp \left[-i \Delta \beta^{\nu'} z \right], \\ \left(i \frac{\partial}{\partial z} + \frac{i}{v_g^{\nu}} \frac{\partial}{\partial t} - \frac{D^{\nu}}{2} \frac{\partial^2}{\partial t^2} \right) u^{\nu} &= -\omega_0^{\text{FW}} \chi_{\text{eff}}^{\nu} \left[u^{\text{FW}} \right]^2 \exp \left[i \Delta \beta^{\nu} z \right]. \end{aligned} \quad (2.35)$$

Also the used coefficients take a simpler form, with the mismatch being

$$\Delta \beta^{\nu} = 2\beta_0^{\text{FW}} - \beta_0^{\nu} + \frac{2\pi}{\Lambda_{\text{QPM}}} \quad (2.36)$$

and the effective susceptibility

$$\chi_{\text{eff}}^{\nu} = \frac{\varepsilon_0}{2\pi P_0} \int_{-\infty}^{\infty} \int_{-\infty}^{\infty} \chi_{333}^{(2)} e_0^{\nu} e_0^{\text{FW}*} e_0^{\text{FW}*} dx dy. \quad (2.37)$$

2.2 Linear dynamics in waveguide arrays

In the preceding section the locally induced perturbing polarizations have been discussed. They have been differentiated in linear and nonlinear perturbations. Nonlocal perturbations, induced to a certain waveguide by the neighboring waveguides placed in regular distances d within the WGA, can be categorized in the same way. However, in this thesis only linear nonlocal perturbations are considered. Nonlinear effects between neighboring waveguides are in general much weaker than local nonlinear effects and are neglected throughout this thesis.

2.2.1 The coupling of multimode waveguides

The linear nonlocal interactions between the individual waveguides of a WGA can be attributed to the evanescent overlap of the fields in the waveguides and lead to a coherent exchange of energy between the guided modes in different waveguides at one frequency. To describe this mathematically, the dielectric functions of the whole WGA $\hat{\varepsilon}(x, y)$ and the n th waveguide $\Delta \hat{\varepsilon}_n(x, y)$ are used. Again, our considerations are restricted to the polarization components along the optical axis of the lithium niobate crystal. The y -component of the polarization induced in a waveguide n by all other waveguides n' reads as

$$\Delta P_{y,n} = \frac{\varepsilon_0}{2} \sum_{\mu} \sum_{n' (n' \neq n)} [\hat{\varepsilon}_{33}(x, y) - \Delta \hat{\varepsilon}_{n,33}(x, y)] u_{n'}^{\mu} e_{n'}^{\mu} e^{(i\beta_{0n'}^{\mu} z - i\omega_{0n'} t)} + \text{c.c.} \quad (2.38)$$

Here we treat only modes of a single frequency which are denoted by the index μ . The sum over all waveguides excludes the interaction of the n th waveguide with itself, which would lead to a small correction of the phase velocity due to the existence of other waveguides. This contribution is very weak compared to the propagation constant in the single waveguide and therefore is neglected, which is in accordance with the initial assumptions. The polarization Eq. (2.38) leads to the following propagation equation for the waveguide mode μ

$$\left[i \frac{\partial}{\partial z} + \frac{i}{v_g^\mu} \frac{\partial}{\partial t} - \frac{D^\mu}{2} \frac{\partial^2}{\partial t^2} \right] u_n^\mu + \sum_{\mu'} \sum_{n' (n' \neq n)} c_{nn'}^{\mu\mu'} u_{n'}^{\mu'} \exp \left[i \left(\beta_0^{\mu'} - \beta_0^\mu \right) z \right] = 0. \quad (2.39)$$

The energy exchange between the modes μ and μ' in the waveguides n and n' , respectively, is characterized by the scalar coupling constants

$$c_{nn'}^{\mu\mu'} = \frac{\varepsilon_0 \omega_0}{4P_0} \int_{-\infty}^{\infty} \int_{-\infty}^{\infty} [\hat{\varepsilon}_{33} - \Delta \hat{\varepsilon}_{n,33}] e_n^{\mu*} e_{n'}^{\mu'} dx dy. \quad (2.40)$$

Eq. (2.39) and Eq. (2.40) are valid only for identical waveguides with $\Delta \hat{\varepsilon}_n(x, y) = \Delta \hat{\varepsilon}_{n'}(x, y)$. For waveguide systems where this does not hold, more involved formalisms to describe the propagation have been developed [144–147]. From Eq. (2.39) and Eq. (2.40) we also see, that in general different modes from different waveguides can exchange energy [21, 148], which is in contrast to a single waveguide where the individual modes have to fulfill the orthogonal relation Eq. (2.6). For identical lossless waveguides the coupling constants Eq. (2.40) are symmetric, $c_{nn'}^{\mu\mu'} = c_{n'n}^{\mu'\mu} = c_{nn'}^{\mu'\mu}$. Under the assumption of small perturbations, only the nearest neighbor interaction needs to be taken into account, leading to the simplified equation

$$\left[i \frac{\partial}{\partial z} + \frac{i}{v_g^\mu} \frac{\partial}{\partial t} - \frac{D^\mu}{2} \frac{\partial^2}{\partial t^2} \right] u_n^\mu + \sum_{\mu'} c^{\mu'\mu} \left[u_{n+1}^{\mu'} + u_{n-1}^{\mu'} \right] \exp \left[i \left(\beta_0^{\mu'} - \beta_0^\mu \right) z \right] = 0 \quad (2.41)$$

with $c^{\mu'\mu} = c_{n n+1}^{\mu'\mu}$.

2.2.2 Mode mixing effects

The coupled mode equations Eqs. (2.41) describe light propagation in an array of equal multimode waveguides, where different modes in adjacent waveguides couple. However, due to different propagation constants, with the exception of the case $\mu = \mu'$, all coupling processes are phase mismatched. Phase-mismatched coupling is generally rather inefficient, as is well known from other coupled phenomena depending on phasematching, like two-core couplers of non-identical waveguides or SHG. The energy transfer from mode μ to μ' is usually negligible. However, additional effects appear due to

so-called cascading processes, which take place if light from mode μ is coupled to mode μ' in the next waveguide and then back to μ . To analyze this, a WGA with only two modes is considered, as we also find later in our experiments. This system is described by the coupled mode equations

$$i \frac{\partial}{\partial z} u_n^1 + c^{11} [u_{n+1}^1 + u_{n-1}^1] + c^{12} [u_{n+1}^2 + u_{n-1}^2] \exp [i (\beta_0^2 - \beta_0^1) z] = 0, \quad (2.42)$$

$$i \frac{\partial}{\partial z} u_n^2 + c^{22} [u_{n+1}^2 + u_{n-1}^2] + c^{21} [u_{n+1}^1 + u_{n-1}^1] \exp [i (\beta_0^1 - \beta_0^2) z] = 0, \quad (2.43)$$

where the temporal degrees of freedom are neglected for simplicity. Only the first mode is excited and $u_n^2(z=0) = 0$. Due to the phase mismatched linear coupling, the energy is oscillating between both modes during propagation. In the stationary regime, the amplitudes of the 2nd mode can be described with the ansatz

$$u_n^2(z) = \Phi_n \exp [i (\beta_0^1 - \beta_0^2) z]. \quad (2.44)$$

Inserting this ansatz into Eq. (2.43) leads to

$$\Phi_n (\beta_0^2 - \beta_0^1) = c^{22} [\Phi_{n+1} + \Phi_{n-1}] + c^{21} [u_{n+1}^1 + u_{n-1}^1] = 0, \quad (2.45)$$

which can be solved using the discrete Fourier transform

$$\Phi_n = \sum_{\kappa} \tilde{\Phi}_{\kappa} e^{i\kappa n}; u_n^1 = \sum_{\kappa} \tilde{u}_{\kappa}^1 e^{i\kappa n}. \quad (2.46)$$

In the Fourier space the equation for Φ_n reads as

$$\tilde{\Phi}_{\kappa} (\beta_0^2 - \beta_0^1) = 2 \cos(\kappa) \left(c^{22} \tilde{\Phi}_{\kappa} + c^{21} \tilde{u}_{\kappa}^1 \right) \quad (2.47)$$

and can be solved straightforwardly

$$\tilde{\Phi}_{\kappa} = \frac{2 \cos(\kappa) c^{21} \tilde{u}_{\kappa}^1}{(\beta_0^2 - \beta_0^1) - 2c^{22} \cos(\kappa)} \approx \frac{2 \cos(\kappa) c^{21} \tilde{u}_{\kappa}^1}{(\beta_0^2 - \beta_0^1)}. \quad (2.48)$$

Here we assume, that the mismatch $(\beta_0^2 - \beta_0^1)$ between two waveguide modes is much larger than the coupling constant c^{22} , which is justified for the WGAs used in this thesis. After transforming back to real space this results in an equation for mode 2

$$u_n^2(z) = \frac{c^{21}}{(\beta_0^2 - \beta_0^1)} [u_{n+1}^1 + u_{n-1}^1] \exp [i (\beta_0^1 - \beta_0^2) z] \quad (2.49)$$

which can be inserted into Eq. (2.42) and leads to

$$i \frac{\partial}{\partial z} u_n^1 + 2C_{\text{mix}} u_n^1 + c^{11} [u_{n+1}^1 + u_{n-1}^1] + C_{\text{mix}} [u_{n+2}^1 + u_{n-2}^1] = 0 \quad (2.50)$$

with

$$C_{\text{mix}} = \frac{c^{12} c^{21}}{(\beta_0^2 - \beta_0^1)}. \quad (2.51)$$

The obtained result in Eq. (2.50) depends now only on one mode. Compared with the well known coupled mode equations for a monomode WGA [37], two additional terms appear. The term $2C_{\text{mix}} u_n^1$ results in a shift of the phase velocity and can be treated as part of the local perturbations described in Section 2.1.3. The term $C_{\text{mix}} [u_{n+2}^1 + u_{n-2}^1]$ is similar to the next-nearest neighbor coupling terms appearing in specially designed WGAs [149–152] or when the assumption of weak linear coupling is dropped [153]. The linear mode mixing effects are weak if the linear mismatch $(\beta_0^2 - \beta_0^1)$ between the waveguide modes is large, as we already assumed. For the WGAs and modes under investigation in this thesis, C_{mix} is always more than 20 times smaller than the coupling constant between similar modes and is neglected. However, this cannot be assumed in general and has to be questioned separately for each WGA.

2.3 Normalized coupled mode equations

The complete set of equations describing the propagation of one FW mode u_n^{FW} and the ν th of several SH modes u_n^ν in the n th waveguide of a large WGA under the influence of a second order nonlinearity is

$$\begin{aligned} \left(i \frac{\partial}{\partial z} + \frac{i}{v_g^{\text{FW}}} \frac{\partial}{\partial t} - \frac{D^{\text{FW}}}{2} \frac{\partial^2}{\partial t^2} + \Delta\beta_{\text{lin}}^{\text{FW}}(z) + i \frac{\alpha^{\text{FW}}}{2} \right) u_n^{\text{FW}} + c^{\text{FW}} [u_{n+1}^{\text{FW}} + u_{n-1}^{\text{FW}}] & \quad (2.52) \\ = -\omega^{\text{FW}} \sum_{\nu} \chi_{\text{eff}}^{\nu} u_n^{\text{FW}*} u_n^{\nu} \exp[-i\Delta\beta^{\nu} z], \\ \left(i \frac{\partial}{\partial z} + \frac{i}{v_g^{\nu}} \frac{\partial}{\partial t} - \frac{D^{\nu}}{2} \frac{\partial^2}{\partial t^2} + \Delta\beta_{\text{lin}}^{\nu}(z) + i \frac{\alpha^{\nu}}{2} \right) u_n^{\nu} + c^{\nu} [u_{n+1}^{\nu} + u_{n-1}^{\nu}] & \\ = -\omega^{\text{FW}} \chi_{\text{eff}}^{\nu} [u_n^{\text{FW}}]^2 \exp[i\Delta\beta^{\nu} z]. & \end{aligned}$$

Although these equations reflect the physical roots of the different effects, they are not well suited for numerical treatment due to the vastly different magnitudes of the various coefficients. This can be improved by a set of normalizations. First the coefficient of the group velocity mismatch (GVM) for the SH mode ν is expressed as the difference

between the inverse group velocities of FW and SH

$$\delta^\nu = \frac{1}{v_g^\nu} - \frac{1}{v_g^{FW}}. \quad (2.53)$$

The nonlinear interaction strengths between the various SH modes and the FW mode are normalized to that of a distinct mode SH1

$$\chi_{\text{eff}}^\nu = \gamma^\nu \chi_{\text{eff}}^{\text{SH1}}, \quad (2.54)$$

which results in $\gamma^{\text{SH1}} = 1$. If the propagation length is rescaled by a scaling length $z = \bar{z}L_0$, the coupling constants, propagation constants, and losses can be readjusted like

$$c^\mu = \frac{C^\mu}{L_0}, \Delta\beta^\nu = \frac{\Delta^\nu}{L_0}, \Delta\beta_{\text{lin}}^\mu(z) = \frac{\Delta_{\text{lin}}^\mu(z)}{L_0}, \text{ and } \alpha^\mu = \frac{2\bar{\alpha}^\mu}{L_0}, \quad (2.55)$$

with ν applying only for SH modes. Now the amplitudes are normalized according to

$$u_n^{FW} = A_n^{FW} \frac{1}{L_0 \chi_{\text{eff}}^{\text{SH1}} \omega^{FW}}, \quad u_n^\nu = A_n^\nu \frac{\exp(i\Delta\beta^\nu z)}{L_0 \chi_{\text{eff}}^{\text{SH1}} \omega^{FW}}. \quad (2.56)$$

Finally, the time is scaled by applying a coordinate frame moving with the FW pulse and normalizing with a fixed scaling time $t = \tau T_0 - \frac{z}{v_g^{FW}}$. Thus, the dispersion coefficients can be set as

$$\delta^\nu = \bar{\delta}^\nu \frac{T_0}{L_0}, \quad D^\nu = \bar{D}^\nu \frac{T_0^2}{L_0}. \quad (2.57)$$

The substitution of all the equations given above in Eqs. (2.52) leads to a set of normalized equations

$$\begin{aligned} \left(i \frac{\partial}{\partial \bar{z}} - \frac{\bar{D}^{\text{FW}}}{2} \frac{\partial^2}{\partial \tau^2} + \Delta_{\text{lin}}^{\text{FW}}(z) + i\bar{\alpha}^{\text{FW}} \right) A_n^{\text{FW}} + C^{\text{FW}} [A_{n+1}^{\text{FW}} + A_{n-1}^{\text{FW}}] \\ = - \sum_\nu \gamma^\nu A_n^{\text{FW}*} A_n^\nu, \\ \left(i \frac{\partial}{\partial \bar{z}} + \bar{\delta}^\nu \frac{\partial}{\partial \tau} - \frac{\bar{D}^\nu}{2} \frac{\partial^2}{\partial \tau^2} - \Delta^\nu + \Delta_{\text{lin}}^\nu(z) + i\bar{\alpha}^\nu \right) A_n^\nu + C^\nu [A_{n+1}^\nu + A_{n-1}^\nu] \\ = -\gamma^\nu [A_n^{\text{FW}}]^2, \end{aligned} \quad (2.58)$$

which can now be treated numerically with great efficiency. Both sets of equations Eqs. (2.52) and Eqs. (2.58) describe the same phenomena and will both be used equally throughout this thesis.

2.4 Experimental methods

In the preceding sections it was explained how nonlinear light propagation in WGAs is described within the framework of the coupled mode theory. The following chapters of this thesis are devoted to particular effects described by these general equations. However, the aim of this thesis is not only to theoretically account for new effects connected to higher order modes, but also to demonstrate them experimentally. To this end now a versatile set of experimental tools to monitor light propagation is described, which is used later on to prove our predictions. First, the generation of the high power input radiation necessary to study nonlinear effects is introduced in detail, afterwards the complete setup will be explained.

2.4.1 Tunable high power light source

Some requirements for the laser light used in the experiments can already be extracted from the physical fundamentals of the effects occurring in the WGA. To probe beam propagation for different values of the phase mismatch defined in Eq. (2.32), the light source needs to be tunable. To avoid strong dispersion of the wavelength dependent phase mismatch across the spectrum of the measurement signal, the spectral width of the used laser source should be small. Furthermore, the nonlinear coefficient χ_{eff}^{ν} is very small and large powers are necessary to produce detectable nonlinear effects. High peak powers are usually achieved by using pulsed lasers with pulse durations in the range of ps or fs. However, to not contradict with the small bandwidth required, the pulses should not be shorter than a few ps. Finally, to enable efficient beam shaping and coupling to an optical waveguide, the beam profile of the laser should be close to an ideal Gaussian beam.

A very wide tuning range in the sought after near-infrared (NIR) wavelength band can be provided by tunable diode lasers, which are available with tuning ranges from 1260 nm to 1640 nm [154]. These lasers are usually fiber coupled, hence provide a very good beam profile. Nevertheless, the output powers are limited to a few mW, not enough to observe most of the effects discussed in this thesis. Fiber amplifiers, which could provide higher powers, are limited by the small amplification bandwidth of the usually employed Erbium doped fibers [155, 156]. The required spectral ranges are supported by optical parametric amplifiers (OPAs), which use non-degenerated three-photon mixing to transfer energy from a pump frequency to the amplified frequency [33, 157]. In the laser system used to perform the experiments described in this thesis, the fiber and OPA approaches are combined. A fiber coupled tunable diode laser provides the controllable large wavelength range and an excellent beam profile. The beam from the fiber is then amplified in a specially designed OPA.

The OPA used here, whose operation principle is shown in Fig. 2.1, was designed

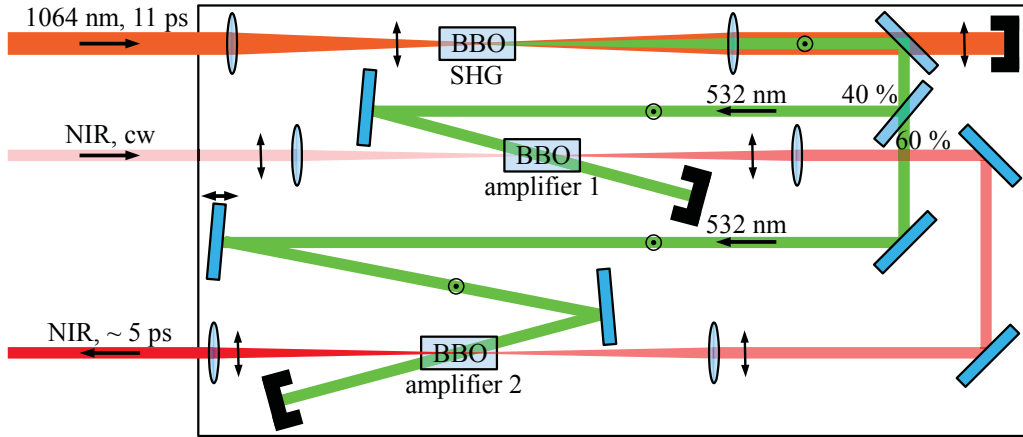


Figure 2.1: Scheme of the operation principle of the two stage, cw-seeded noncollinear optical parametric amplifier (NOPA). The arrows and \odot symbols on the beams in the sketch denote the beam polarization.

and built at the Ludwig-Maximilians-Universität Munich [158] and is a noncollinear optical parametric amplifier (NOPA) [159–161]. The amplifier is pumped by pulses with a full-width half-maximum (FWHM) length of 11 ps. The pump pulse energy is $\approx 400 \mu\text{J}$ with a repetition rate of 5 kHz and a central wavelength of 1064 nm. In a first step the pump light is frequency doubled by SHG in a β -barium borate (BBO) crystal. The resulting light beam with a wavelength of 532 nm (green in Fig. 2.1) is divided with a ratio of 40:60 by a beam splitter to pump the two amplification stages. The amplification stages again consist of BBO crystals. Here the pump beam is split by noncollinear difference-frequency generation (DFG) into signal and idler frequencies, which have to fulfill the energy conservation relation $\omega^{\text{pump}} = \omega^{\text{signal}} + \omega^{\text{idler}}$. The amplification of signal and idler is determined by the phasematching properties of the BBO crystal, which allow for several pairs of frequencies and directions to be generated. To control the amplified signal, the desired NIR frequency is seeded, thus fixing also the propagation direction and the idler properties. The cw seed light is generated in a standard tunable diode laser, allowing for computer controlled wavelength tuning over a wide range. After the BBO amplifier stages the idler photons generated in the DFG process are filtered out. Since only short pulses of the cw-seed are amplified, the two amplification stages need to be synchronized to always overlap a pump pulse with a seed pulse. This is achieved by placing one of the pump beam folding mirrors onto a linear stage, thus enabling to change the propagation distance of the pump pulses.

The output pulses of the described NOPA are characterized temporally with an autocorrelator and spectrally with an optical spectrum analyzer. The laser system generates ≈ 5 ps long pulses with a repetition rate of 5 kHz and a pulse energy of $\approx 4 \mu\text{J}$ for the complete tuning range of the used tunable diode lasers. The spectral FWHM bandwidth of the generated pulses is always 0.11 THz, which corresponds to

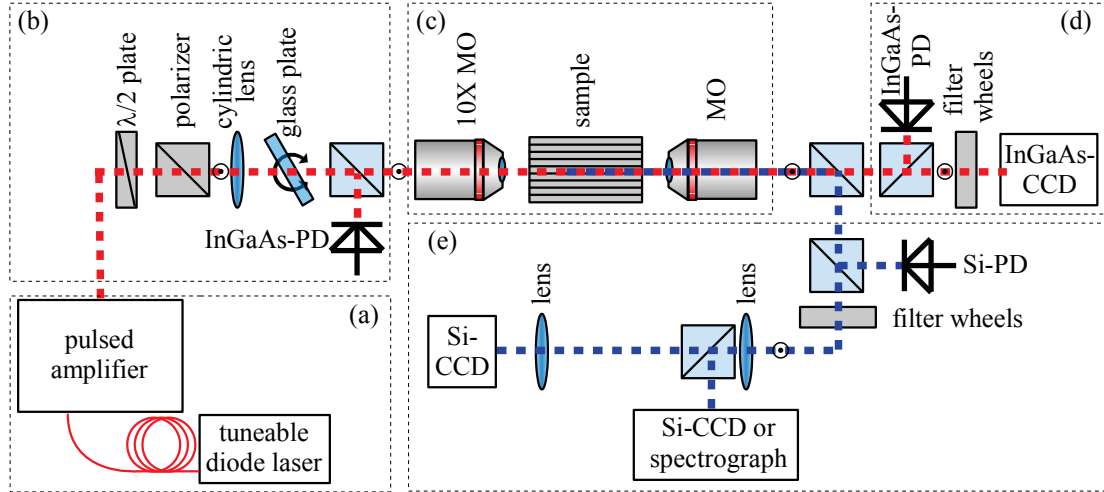


Figure 2.2: Sketch of the setup including (a) laser and amplifier, (b) beam shaping, (c) sample coupling and detection instruments for (d) the FW and (e) the SH frequency components. The beam paths of FW and SH light are drawn in red and blue, respectively. The abbreviations mean MO - microscope objective and PD - photodetector. The TM polarization is denoted by the \odot symbol.

0.85 nm at a wavelength of 1500 nm. Computer controlled wavelength changes within a bandwidth of 20 nm can be achieved without changing the amplifier setup due to the large phasematching bandwidth of the BBO crystals. Only the seed laser wavelength needs to be adjusted. However, the BBO crystals have to be readjusted when tuning across a larger spectral range is necessary. The low power cw-beam of the seed laser is always part of the NOPA output as a weak background signal. Consequently, the laser system can also be used as a low power cw source by switching off the pump pulse.

2.4.2 Optical setup and detection tools

The central part of the experimental apparatus used here is the investigated WGA sample. Since the described laser system generates a light beam with diameters of several mm, suitable optical elements are employed to couple light in and out of the sample. These coupling devices and the sample stage form the core part of the setup described here. To probe the various aspects of light propagation in dependence on the characteristic parameters of the coupled light, e.g. power, wavelength, beam shape, beam tilt and beam position, these parameters have to be tunable. They are set in a separate building block between laser system and sample coupling. Finally, the light coupled out of the sample has to be detected and evaluated. Since we use two distinct wavelength ranges, FW and SH, two separate detection systems are necessary, which form the last building blocks of a flexible setup.

Fig. 2.2 shows a sketch of the experimental apparatus used for the measurements described throughout this thesis. The general building blocks described above are

marked by the dashed labeled boxes. The beam manipulation system is shown in Fig. 2.2(b). The polarization is fixed by a polarizer to TM (vertical) to be parallel to the optical axis of the sample crystals and thus use the $\chi_{333}^{(2)}$ element of the nonlinear susceptibility tensor. To set the laser beam power, a rotating half-waveplate in front of the polarizer is used. The waveplate controls the polarization of the incoming beam and hence determines the power fraction transmitted by the polarizer. The position of the waveplate is changed computer controlled according to the desired input power. Feedback is provided by an Indium-Gallium-Arsenide (InGaAs) photodetector measuring the power of a fixed small fraction of the beam, which is split off after all optical elements but in front of the coupling objective. According to the desired experimental conditions also the beam width has to be adjusted. If just a single waveguide of the WGA needs to be excited, after the coupling objective a round focus spot with a full-width at half-maximum (FWHM) of $\approx 4\ \mu\text{m}$ should be realized. For this purpose, the lens coupling to the sample is chosen such that it forms the necessary focal spot out of the existing laser beam, which has a FWHM of 2 mm and a negligible diffraction at a wavelength of 1500 nm. To excite several waveguides in the 1D WGA, the horizontal beam width needs to be adjusted accordingly, with a maximum FWHM in the range of 100 μm . To form an elliptic focal spot after the coupling objective a cylindric lens is introduced in the beam path in front of it. Together they form a telescope for only the horizontal direction of the beam. To ensure that both horizontal and vertical focus positions of the coupling spot are in the same longitudinal position, the focus of the cylindric lens has to be in the backside focal point of the objective. The horizontal beam width can now be chosen by using an appropriate cylindric lens. A smaller focus (and smaller focal length) of the cylindric lens leads to a wider ellipse of the coupling spot after the microscope objective. In the experiments presented here, two different cylindric lenses are used. In Chapter 3, a lens with a focal length of 200 mm is used to create an elliptic focus with a horizontal FWHM of 110 μm , whereas in Chapter 4 and Chapter 5 the desired horizontal FWHM of 60 μm is achieved with a cylindric lens of 400 mm focal length.

Finally, the angle of the exciting beam with respect to the front facet of the sample has to be changed in order to achieve phase differences between adjacent excited waveguides. If only a single angle is necessary to perform the measurement, as is the case in Chapter 4 and Chapter 5, this task is solved by inserting a rotating glass plate in front of the coupling stage which slightly shifts the beam away from the center of the microscope objective (see Fig. 2.2(b)). This leads to a tilt of the beam after the objective, shown schematically in Fig. 2.3(a). However, since the available rotating stages are not motorized, this method is not feasible if the beam angle has to be scanned continuously, as in Chapter 3. Hence, the beam shaping part needs to be modified to fulfill this task. To this end, a moving mirror on a computer controlled linear stage as

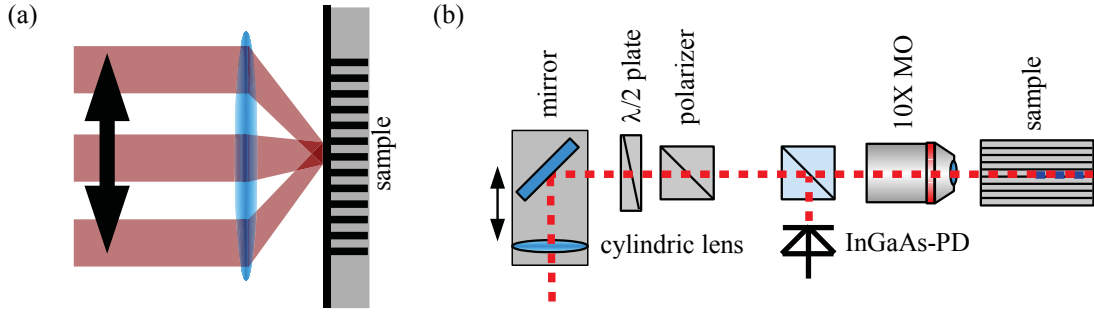


Figure 2.3: (a) Scheme of the coupling to the sample with laterally shifted beams. (b) Beam shaping and coupling parts of the setup used in Chapter 3.

shown in Fig. 2.3(b) was utilized to move the beam laterally. The part of the setup shown in Fig. 2.3(b) is used instead of the elements in Fig. 2.2(b). To achieve an input spot width and phase profile independent of the mirror position the cylindrical lens is also placed on the linear stage.

The coupling system of the setup depicted in Fig. 2.2(c) consists of two microscope objectives and the sample holder. For the coupling into the sample a Newport F-L10B laser diode objective was used. This 10X objective has a very high transmission of 0.94 for wavelengths in the near infrared. The output coupling and imaging onto the detection units is performed with different microscope objectives, depending on the measurement task. For most of the measurements presented throughout this thesis, also a 10X microscope objective is employed. The sample itself is placed in an oven and usually heated to 220 °C to prevent SH induced photorefraction [31].

Behind the output coupling objective a dichroic beamsplitter is installed, which transmits the FW and reflects the SH components. This is necessary to divide the beam between the detection systems for both wavelengths. In the FW detection system in Fig. 2.2(d), first a beamsplitter separates a small part of the FW power and guides it to a power measuring indium-gallium-arsenide (InGaAs) photodetector. The FW is measured by an InGaAs charge-coupled-device (CCD) camera, which allows to record the 2D output intensity profiles of the WGA. The used camera is a Xenics Xeva-1.7-640 with a resolution of 640×512 pixels. The camera is read out by a computer, which, based on the illumination level, automatically sets filter wheels to always provide the best possible dynamic range without camera saturation.

The SH detection system in Fig. 2.2(e) works in a similar a fashion. First, a small part is split off and routed to a power detector. Again a computer controlled filter wheel is installed to set the excitation levels for the used cameras. However, not only spatial information needs to be obtained for the SH but also the spatial spectrum. A 4f-setup with two lenses of 75 mm focal length is utilized to achieve this. The length of four times this focal distance starts at the image plane of the microscope objective

coupling out of the sample, which is fixed since an FW image has to be generated on the FW camera. Here also a spatial filter is installed, which allows for the selection of certain waveguides for further evaluation. A beamsplitter is integrated in the 4-f setup to allow for simultaneous detection of spatial and spatio-spectral intensity. The spatial intensity of the SH is detected after the 4f-setup with a Hamamatsu ORCA silicon (Si) CCD with a resolution of 1344×1024 pixels. The SH spatial spectrum is monitored in the Fourier plane of the 4f-setup. Here either a Yobin-Yvon iHR320 spectrometer, which allows also for spectral decomposition of the SH signal, or a Basler A102f Si-CCD with 1392×1040 pixels resolution is used.

The presented setup allows for a great flexibility in exciting the sample under test. It enables computer controlled scans of the input power, wavelength, and, with the modification presented in Fig. 2.3, input angle. For each set of excitation parameters, the powers and output profiles of both frequency components can be measured automatically under optimized measurement conditions. Hence, automated parameter scans are possible.

Chapter 3

Second harmonic generation

SHG is one of the most studied and applied nonlinear optical processes. The generation of light at the SH frequency ω^{SH} by frequency doubling of an input FW frequency ω^{FW} is the first experimentally observed nonlinear optical effect [27]. It is widely used to generate laser wavelengths not available otherwise. Additionally, since the SHG is well understood theoretically, it can be used for structural investigation of optical crystals [162].

One of the peculiarities of SHG is the necessity of phasematching between FW and SH fields to achieve a high conversion efficiency. With the QPM technique, phase-matching can be only achieved for singular wavelengths due to dispersion. This leads to a resonance-like dependence of the SH output power on the FW input frequency. In this chapter the basic properties of SHG and phasematching in WGAs are reviewed and it is shown that due to the SHG resonances specific SHG modes can be excited precisely. This ability is used to characterize the properties of SHG modes in WGAs, which is important for the modeling of later experiments. In these characterization experiments, changes of the phasematching properties due to nonlinear interactions with several modes [77] must be avoided. To achieve this, the lowest FW input powers sufficient to generate detectable SH are used. The necessary power can already be delivered by a cw laser, hence our mathematical description is restricted to the cw case and the dispersion terms in Eqs. (2.52) are dropped.

Already in Chapter 2 it was shown, that the guided modes of all frequencies are determined by the single waveguide and that the nonlinear effects act only locally. Consequently, in Section 3.1 first the linear and nonlinear properties of single waveguides are studied. In Section 3.2 the focus will be on SHG in a WGA. Here, the influence of the transverse degree of freedom in WGAs on the phasematching for SHG will be investigated and methods using the peculiarities of SHG to characterize the linear states of the WGA are discussed.

3.1 The isolated waveguide

The majority of the characteristic coefficients in the full set of propagation equations Eqs. (2.52) are derived from properties of the linear eigenmodes of a separated waveguide. Hence, in Section 3.1.1 the relevant eigenmodes and their respective propagation constants are introduced for both FW and SH frequencies. SHG between several pairs of FW and SH modes is investigated in Section 3.1.2 to get insight into the dependence on the mode propagation constants, mode symmetries and excitation conditions.

3.1.1 Properties of guided modes

Lithium niobate, which is the host material for all WGAs used in this thesis, is a uniaxial crystal [137]. Hence, the extraordinary permittivity $\hat{\epsilon}_{33}$ in the dielectric tensor in the crystal coordinate system differs from the two similar ordinary values of $\hat{\epsilon}_{11}$ and $\hat{\epsilon}_{22}$. In this thesis only electric fields polarized linearly in the y -direction are taken into account. Hence, only the wavelength dependent extraordinary permittivity $\hat{\epsilon}_{33}(\lambda)$ and the refractive index $n_{\text{host}}(\lambda) = \sqrt{\hat{\epsilon}_{33}(\lambda)}$ will be used from now on to characterize the material.

The waveguides and WGAs used for the experiments described in this thesis were fabricated at the University of Paderborn using titanium indiffusion [163–165]. This technique uses thin stripes of titanium, which are deposited on and then indiffused into the lithium niobate wafer to generate the locally increased refractive index needed to guide light. The resulting profile of the refractive index in the lithium niobate crystal is $n(x, y, \lambda) = n_{\text{host}}(\lambda) + \Delta n_{\text{Ti}}(x, y, \lambda)$, where $n_{\text{host}}(\lambda)$ is the refractive index of bulk lithium niobate and $\Delta n_{\text{Ti}}(x, y, \lambda)$ is the change of the refractive index induced by the indiffused titanium. The latter can be calculated with $\Delta n_{\text{Ti}}(\lambda, x, y) = f_e(\lambda) F_e \rho(x, y)$, where $F_e = 1.2 \cdot 10^{-23} \text{ cm}^3$ is a concentration constant and $f_e(\lambda) = (0.839\lambda^2) / (\lambda^2 - 0.0645)$ accounts for the dispersion. The concentration of titanium in the lithium niobate crystal $\rho(x, y)$ is described by [166–168]

$$\rho(x, y) = \frac{1}{2} \rho_0 \left(\operatorname{erf} \left[\frac{w_{\text{Ti}}}{2D_x} \left(1 + \frac{2x}{w_{\text{Ti}}} \right) \right] + \operatorname{erf} \left[\frac{w_{\text{Ti}}}{2D_x} \left(1 - \frac{2x}{w_{\text{Ti}}} \right) \right] \right) \exp \left(-\frac{y^2}{D_y^2} \right). \quad (3.1)$$

Here $\rho_0 = 6.412 \cdot 10^{22} \text{ cm}^{-3} d_{\text{Ti}}/D_y$ is the concentration at the surface of the substrate with the thickness of the titanium stripe r_{Ti} . w_{Ti} is the width of the titanium stripe and D_x and D_y are the diffusion constants parallel and perpendicular to the surface of the lithium niobate substrate, respectively. The determination of the diffusion constants is crucial to describe the index profile in the samples. Although they have been measured in bulk lithium niobate [169, 170], for the samples used in the experiments presented here they vary [171]. The diffusion constants of each sample are determined experimentally by fitting simulated mode profiles for the refractive index profile calculated

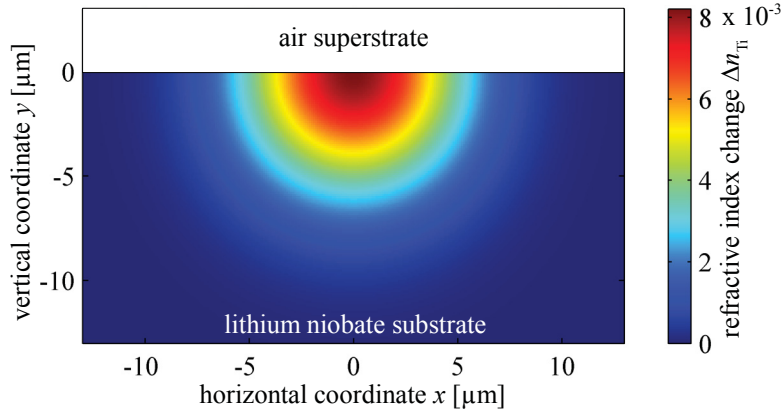


Figure 3.1: Typical change of refractive index due to titanium indiffusion in a Ti:LiNbO₃ waveguide. The waveguide parameters are $D_x = 4.5 \mu\text{m}$, $D_y = 5.78 \mu\text{m}$, $r_{\text{Ti}} = 100 \text{ nm}$, $w_{\text{Ti}} = 7 \mu\text{m}$, and $\lambda = 1550 \text{ nm}$. The upper edge of the substrate is localized at $y = 0$.

with Eq. (3.1) to the measured mode profiles, as is described in detail in Appendix B.

Fig. 3.1 shows Δn_{Ti} calculated with the concentration profile Eq. (3.1) with $D_x = 4.5 \mu\text{m}$ and $D_y = 5.78 \mu\text{m}$. The titanium thickness $r_{\text{Ti}} = 100 \text{ nm}$ and width $w_{\text{Ti}} = 7 \mu\text{m}$ will be the same for all samples described in this thesis. The refractive index of the lithium niobate substrate can be calculated for a large range of wavelengths and temperatures [172].

With the refractive index profile $n(x, y, \lambda)$ the eigenmodes of a waveguide are defined as solutions of the wave equation Eq. (2.4) for the y -components of the electric field in the form of Eq. (2.5). The eigenmode field profiles $e_y^\mu(x, y, \lambda)$ of the waveguide described with the parameters mentioned above were calculated with FEM and are shown in Fig. 3.2. For a wavelength of 1500 nm the waveguide supports two guided modes shown in Fig. 3.2(a). The number of guided modes at smaller wavelengths is much higher, in Fig. 3.2(b) the eight modes with the highest propagation constants for a wavelength of 750 nm are plotted. The modes are labeled FW or SH, according to their frequency, followed by the numbers of sign changes of the electric field in y - and x -direction, e.g. SH00 for the first order mode of the SH frequency. An important characteristic of the modes is their symmetry with respect to the $x = 0$ axis. Even modes with $e_y^\mu(x, y, \lambda) = e_y^\mu(x, -y, \lambda)$ must have an even number of zero crossings in x -direction, while odd solutions have $e_y^\mu(x, y, \lambda) = -e_y^\mu(x, -y, \lambda)$ and an odd number of zero crossings.

The eigenvalues $\beta^\mu(\lambda)$ of the eigenvalue problem introduced by ansatz Eq. (2.5) and Eq. (2.4) are the propagation constants of the eigenmodes. However, the phase velocity of the guided modes is often described with the effective index $n_{\text{eff}}^\mu(\lambda)$ of the mode, which is defined by

$$\beta^\mu(\lambda) = \frac{2\pi}{\lambda} n_{\text{eff}}^\mu(\lambda). \quad (3.2)$$

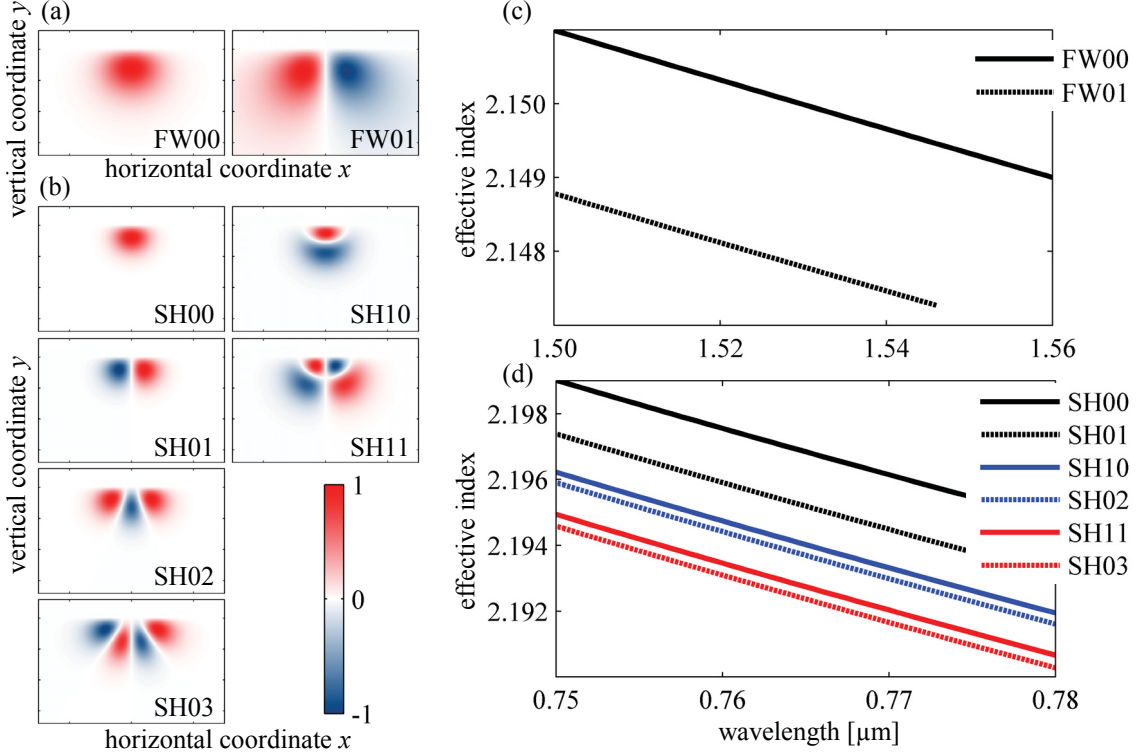


Figure 3.2: (a) Normalized y -component of the electric field of the eigenmodes with mode indices for the refractive index profile shown in Fig. 3.1 for a wavelength of 1500 nm and a temperature of 220°C. (b) Same as (a) for a wavelength of 750 nm. (c,d) Wavelength dependence of the effective indices for (c) FW and (d) SH modes.

In Figs. 3.2(c) and (d) the wavelength dependence of the effective indices of the calculated modes is plotted. All effective indices decrease monotonically with increasing wavelength. Their dispersion is mainly determined by the material dispersion and is almost independent from the mode index. Notably, the FW01 mode has its long wavelength cut-off at around 1545 nm and is not guided for larger wavelengths.

After the introduction of the eigenmodes and propagation constants and a review of their basic properties, in the next section SHG of the eigenmodes of different frequencies will be analyzed in a single waveguide.

3.1.2 Second harmonic generation in a single waveguide

The nonlinear propagation of harmonic waves of an FW mode ξ and an SH mode ν in a homogeneous lossless waveguide is described by

$$\begin{aligned}
 i \frac{\partial}{\partial z} u^\xi(z) &= -\omega^{\text{FW}} \sum_{\xi'} \sum_{\nu'} \chi_{\text{eff}}^{\nu' \xi \xi'} u^{\xi'^*}(z) u^{\nu'}(z) \exp[-i \Delta \beta^{\nu' \xi \xi'} z], \\
 i \frac{\partial}{\partial z} u^\nu(z) &= -\omega^{\text{FW}} \sum_{\xi' \xi''} \chi_{\text{eff}}^{\nu \xi' \xi''} u^{\xi'}(z) u^{\xi''}(z) \exp[i \Delta \beta^{\nu \xi' \xi''} z],
 \end{aligned} \tag{3.3}$$

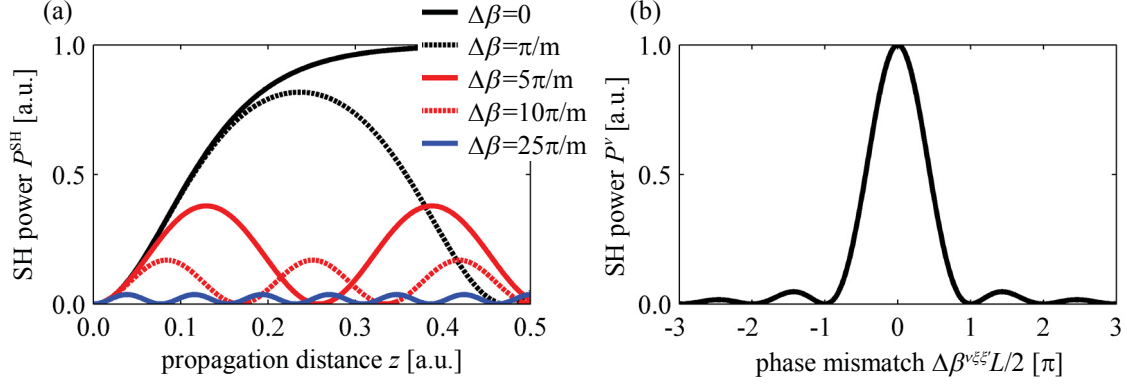


Figure 3.3: (a) SH power P^{SH} in dependence on the mismatch and the propagation distance. (b) Mismatch dependence of the SH power for a fixed sample length L .

derived from Eqs. (2.31) by omitting inhomogeneity, loss and dispersion. ξ' and ξ'' index the FW modes whereas ν' denotes the SH modes. Eqs. (3.3) can be solved analytically for only one FW and SH mode and $u^{\text{SH}}(0) = 0$ [28]. In Fig. 3.3(a) the analytically calculated SH power $P^{\text{SH}}(z) = |u^{\text{SH}}(z)|^2$ for this case is plotted for different mismatches in dependence on the propagation distance. The total power in the waveguide is conserved (if losses are neglected), $P^{\text{SH}} + P^{\text{FW}} = \text{const.}$ For $\Delta\beta = 0$ the FW is completely depleted and converted to SH. For increasing mismatch the maximum conversion efficiency decreases, and the energy oscillates between FW and SH.

For the multimode case the dependence of the SH output power on the phase mismatch for a fixed propagation length L can be calculated in the undepleted pump approximation, i.e. the FW modes fulfill $|u^\xi(z)|^2 \approx |u^\xi(0)|^2 \forall \xi$. These assumption implies, that only a negligible part of the energy of the FW field is transferred to the SH field. In this case the amplitude of any SH mode ν is [135, 173]

$$u^\nu(L) = -\omega^{\text{FW}} \sum_{\xi\xi'} \frac{\chi_{\text{eff}}^{\nu\xi\xi'} u^\xi(0) u^{\xi'}(0)}{\Delta\beta^{\nu\xi\xi'}} \left[\exp(i\Delta\beta^{\nu\xi\xi'} L) - 1 \right]. \quad (3.4)$$

The power of the generated SH field is $P^\nu(L) = |u^\nu(L)|^2$ and in general is dependent on the interference of SH generated by several FW mode pairs $\xi\xi'$. However, in realistic systems the mismatches $\Delta\beta^{\nu\xi\xi'}$ differ much for different FW mode pairs. Thus, in the vicinity of the SHG maximum for a particular pair of FW modes at $\Delta\beta^{\nu\xi\xi'} = 0$, the interference terms are neglected. The resulting power in the ν th SH mode is

$$P^\nu(L) = \frac{1}{2} \sum_{\xi\xi'} \left(\omega^{\text{FW}} \chi_{\text{eff}}^{\nu\xi\xi'} \right)^2 P^\xi(0) P^{\xi'}(0) \text{sinc}^2 \left(\frac{\Delta\beta^{\nu\xi\xi'} L}{2\pi} \right), \quad (3.5)$$

with $\text{sinc}(x) = \sin(\pi x)/\pi x$. The normalized SH output power of an SHG process with

one pair of FW modes is shown in Fig. 3.3(b). The maximum conversion efficiency is obtained for vanishing mismatch and the SH output power quickly drops for increasing $\Delta\beta^{\nu\xi\xi'}$. If different terms of the sum in Eq. (3.4) are taken into account, the SH output power in dependence on the mismatch shows several separated maxima.

Fig. 3.3(b) shows that significant SHG for a certain mode combination can only be achieved if the corresponding phase mismatch Eq. (2.32) vanishes. This can be controlled by either employing the temperature dependence of the refractive index of lithium niobate [172] or the dispersion of the mode propagation constants [see Figs. 3.2(c,d)]. In the second case, used here, the wavelength of the interacting fields is adjusted and the temperature is kept constant.

SHG depends on the phase mismatch, but the maximum output power is determined by the effective nonlinearity $\chi_{\text{eff}}^{\nu\xi\xi'}$ defined in Eq. (2.33). This quantity depends on the overlap integral

$$K^{\nu\xi\xi'} = \int_{-\infty}^{\infty} \int_{-\infty}^{\infty} e_0^\nu e_0^{\xi'*} e_0^{\xi'*} dx dy \quad (3.6)$$

of the mode profiles participating in the nonlinear interaction. The absolute value of $K^{\nu\xi\xi'}$ depends sensitively on the specific mode profiles and hence on the fabrication parameters of the investigated waveguide. However, since the mode profiles e_0^μ are real, universal rules with respect to the mode symmetry can be formulated. For degenerate interactions ($\xi = \xi'$) the overlap integral with odd SH modes is always 0 since the product of two functions with equal symmetry is always even. The same holds true for any two FW modes with the same symmetry. Hence, the only way to achieve a non-vanishing overlap integral with an odd SH mode is to utilize interactions with one even and one odd FW mode.

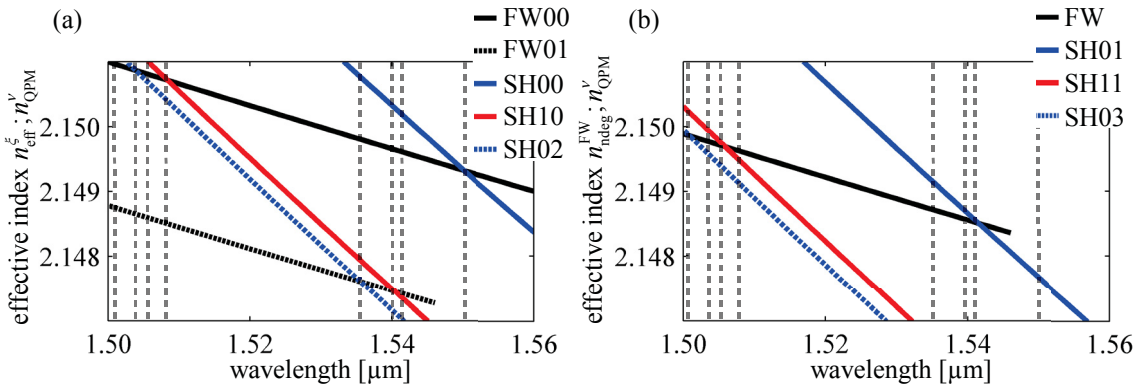


Figure 3.4: Phasematching condition for a single waveguide. (a) Effective refractive indices of the FW and even SH modes, where the SH indices include the contributions of the QPM grating. (b) Effective indices for odd SH modes accounting for the QPM grating and mean effective index of both FW modes. The dashed lines mark all phasematching wavelengths.

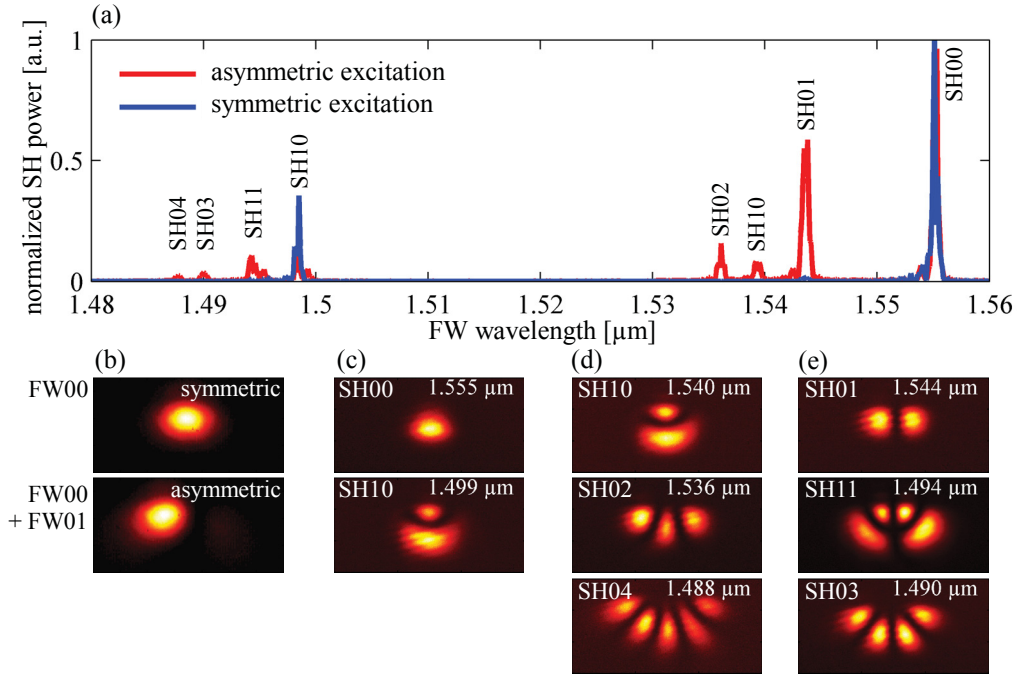


Figure 3.5: (a) Tuningcurve measurements in a single waveguide with centered and shifted excitation. The FW input power is 3 mW for the complete spectral range. (b) FW output of the waveguide for both excitations. (c) SH modes for symmetric FW excitation. The given wavelengths correspond to the peaks in the tuningcurve. (d) Even and (e) odd SH modes appearing only for detuned excitation.

For the SH waveguide modes calculated in Section 3.1 the possible nonlinear interactions are visualized in Fig. 3.4. In Fig. 3.4(a) the effective indices of the FW modes n^ξ and the quantity $n_{\text{QPM}}^\nu = n_{\text{eff}}^\nu + \lambda^{\text{FW}}/2\Lambda^{\text{QPM}}$, accounting also for the periodic poling, are shown for even SH modes. Each intersection designates a wavelength where the corresponding phase mismatch vanishes. In Fig. 3.4(b) the same information is plotted for the non-degenerate interactions possible in this waveguide, where two different FW modes of the same wavelength interact with one SH mode. For the FW $n_{\text{ndeg}}^{\text{FW}} = (n_{\text{eff}}^{\text{FW00}} + n_{\text{eff}}^{\text{FW01}})/2$ is plotted to account for the mixing of both FW modes. All phasematching wavelengths are denoted by the dashed lines in Fig. 3.4(a) and (b). Again, the cut-off of the FW01 mode imposes a long wavelength limit for possible nonlinear interactions involving this mode.

SHG in a single waveguide is studied experimentally by coupling an FW beam with 3 mW power into a lithium niobate waveguide and measuring the SH output power in dependence on the FW wavelength. The spectrum obtained by this type of measurement is called a tuningcurve. The Gaussian input spot can be adjusted and hence the overlap integrals Eqs. (2.9) with the FW modes can be influenced. Tuningcurves of the single waveguide for two different adjustments of the input spot are presented in Fig. 3.5(a). The blue curve is measured for a symmetric excitation in the waveguide center, whereas the red curve is measured with an asymmetric excitation

shifted horizontally by $\approx 3 \mu\text{m}$. Both curves show a number of characteristic peaks, which correspond to the resonances obtained for low efficiency SHG. However, in the experiment these maxima differ from the sinc-function Eq. (3.5) because of sample inhomogeneities. Fig. 3.5(b) shows the profiles of the FW wave at the sample output. For the symmetric excitation only the overlap with the symmetric fundamental mode FW00 is large, which consequently is detected at the array output [see Fig. 3.2 for comparison]. In the asymmetric case, the overlap integrals with both propagating FW modes have similar values, and hence the FW output is a superposition of the FW00 and FW01 mode profiles. As is expected from the symmetry considerations, the FW excitation has a profound influence on the measured tuning curves. If the FW00 mode is excited exclusively, only even SH modes can be generated. This is verified by measuring the mode profiles of the SH with a CCD camera at the wavelength of maximum SHG. Fig. 3.5(c) shows the SH mode profiles measured for the symmetric (FW00) excitation. As expected, both modes are even. These two SH modes are excited at the same wavelengths also for detuned input field. Additional peaks appear, which are due to the excitation of the FW01 mode in the detuned case. Figs. 3.4(d,e) show the corresponding even and odd SH mode profiles, respectively. According to the argument given above, the odd modes can be only generated if both FW modes are excited. The position of the phasematching wavelengths is qualitatively in good agreement with the predictions from the FEM simulations Fig. 3.4. The deviations are in the range of a few nm and are a result of the influence of very small variations of the actual refractive index profile on the properties of the modes. The measurements show, that higher order SH modes can be precisely excited by SHG. Thus, suitable modes and clusters of phasematching resonances for the experiments in Chaps. 4 and 5 can be identified.

3.2 Waveguide arrays

After we explored the properties of SHG in a single waveguide in the preceding section we will now focus on WGAs. In contrast to the last section, energy can now be exchanged between adjacent waveguides. First, the consequences of this additional transverse degree of freedom will be analyzed in detail. The linear propagation of light with a single frequency in a homogeneous lossless WGA is, according to Section 2.2, described by

$$i \frac{\partial}{\partial z} u_n^\mu(z) + c^\mu [u_{n+1}^\mu(z) + u_{n-1}^\mu(z)] = 0, \quad (3.7)$$

where the initial condition $u_n^\mu(0)$ is determined by the overlap of the exciting beam with the waveguide modes according to Eq. (2.9).

For WGAs, where the number of waveguides N goes to infinity, Eq. (3.7) can be

solved analytically. To this end the equation has to be Fourier transformed according to

$$\tilde{u}^\mu(\kappa, z) = \frac{1}{2\pi} \sum_n u_n^\mu(z) \exp(-i\kappa n), \quad u_n^\mu(z) = \int_{-\pi}^{\pi} \tilde{u}^\mu(\kappa, z) \exp(i\kappa n) d\kappa. \quad (3.8)$$

The $\tilde{u}^\mu(\kappa, z)$ are the amplitudes of the eigenmodes of the infinite WGA. In the coupled mode approximation these so-called supermodes $e_{\text{array}}^\mu(x, y, \kappa)$ are linear combinations of the mode profiles $e^\mu(x, y)$, where κ is the phase difference between adjacent waveguides, $e_{\text{array}}^\mu(x, y, \kappa) = \sum_n e^\mu(x, y - nd) \exp(i\kappa n)$ with the period d of the WGA. These supermodes are very good approximations of the Floquet-Bloch modes of the periodic system [23, 24], which can be found by solving Eq. (2.4) for the dielectric profile of the periodic array. However, in general not all Floquet-Bloch modes can be approximated by supermodes and hence, the discrete model cannot always be used. A particular example are modes where the linear inter-mode mixing cannot be neglected as discussed in Section 2.2.2. Here the Floquet-Bloch modes consist of contributions from several waveguide modes.

Applying the discrete spatial Fourier transform Eq. (3.8) to Eq. (3.7) yields the propagation equation for the supermodes

$$\left[i \frac{\partial}{\partial z} + 2c^\mu \cos(\kappa) \right] \tilde{u}^\mu(\kappa, z) = 0. \quad (3.9)$$

The solution of this equation is a mode amplitude with constant magnitude along z but an evolving phase, which is $2c^\mu \cos(\kappa) z$. With this we can define the longitudinal wavenumber of the supermode in the slowly varying envelope approximation, which depends on the transverse wavenumber

$$k^\mu(\kappa, \lambda, T) = 2c^\mu(\lambda, T) \cos(\kappa). \quad (3.10)$$

Eq. (3.10) is known as the diffraction relation of the weakly coupled WGA and determines the linear propagation in the array [37]. The complete longitudinal wavenumber of a supermode in the WGA, describing the physical phase velocity, is

$$k_0^\mu(\kappa, \lambda, T) = 2c^\mu(\lambda, T) \cos(\kappa) + \beta_0^\mu(\lambda, T) = k^\mu(\kappa, \lambda, T) + \beta_0^\mu(\lambda, T). \quad (3.11)$$

Eq. (3.11) determines a continuous band of longitudinal wavenumbers for the supermodes of the waveguide mode μ , depending on the transverse wavenumber and is hence often termed the band of the supermode. In the WGA the wavenumber spectrum of each single waveguide eigenmode is broadened to form a band, just depending on the coupling constant. Fig. 3.6 shows the Floquet-Bloch bands of an array with

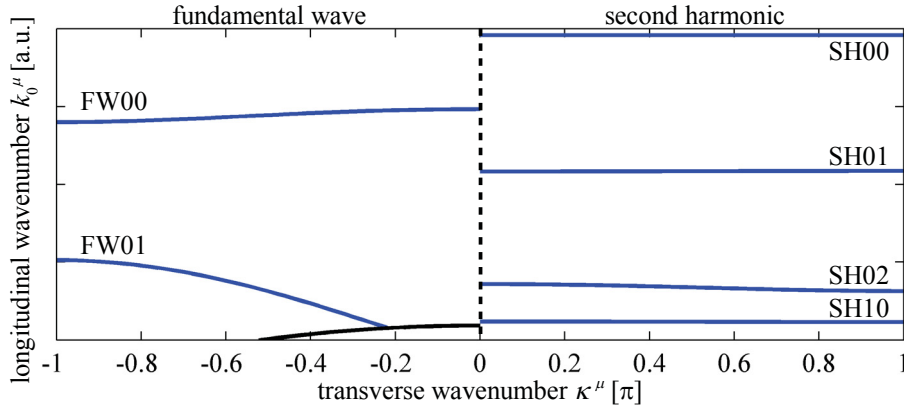


Figure 3.6: Bands of the FW (left panel) at 1500 nm and the SH at 750 nm. The black line in the left panel shows the wavenumber for propagation in bulk lithium niobate and the labels denote the mode indices.

$D_x = 3.8 \mu\text{m}$, $D_y = 4.45 \mu\text{m}$ and a period of $d = 12.5 \mu\text{m}$, which are calculated for the complete periodic system [132]. The bands are periodic with a period of 2π and symmetric with respect to $\kappa^\mu = 0$. Hence, it is sufficient to plot only the bands for one half of the first period of the bandstructure. Commonly, each period of the complete bandstructure is called a Brillouin zone. The first FW band and the first four SH bands indeed can be approximated with the cos-function Eq. (3.11). However, the FW01 band is clipped by the cut-off of waveguiding in the array, marked by the black line. Hence, it cannot be described with the coupled mode approximation and thus not with Eq. (3.11). In the following we always assume, that only one complete FW band exists in the investigated arrays. Hence, only one equation is necessary to describe this FW mode, which is denoted by the index FW.

If only one supermode with the transverse wavenumber κ_0 is excited, back transformation of the solution of Eq. (3.9) according to Eq. (3.8) leads to the solution in the spatial domain

$$u_n^\mu(z) = u_0^\mu(\kappa_0) \exp(i[2c^\mu \cos(\kappa_0)z + \kappa_0 n]), \quad (3.12)$$

which describes a discrete plane wave with the fixed amplitude $u_0^\mu(\kappa)$ in all waveguides propagating with the longitudinal phase velocity $k^\mu(\kappa_0)$ and a fixed phase difference of κ_0 between the waveguides.

In the following sections we will explore how SHG of plane waves in WGAs depends on the transverse wavenumber κ and the longitudinal wavenumber $k^\mu(\kappa)$.

3.2.1 Transverse phasematching

In Section 3.1 we investigated SHG in a single waveguide without transverse dynamics. In this system the SH output depends mostly on the phase mismatch $\Delta\beta^{\nu\xi\xi'}$ due to

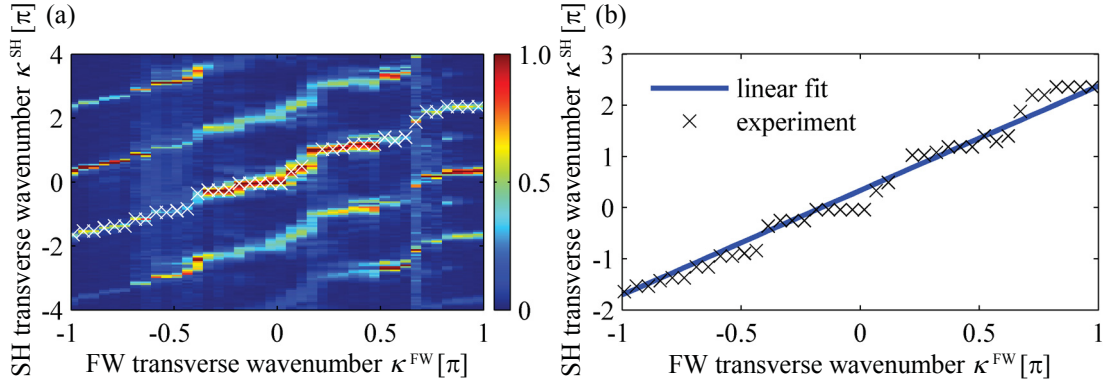


Figure 3.7: (a) Spatial spectrum of the SH output of a WGA in dependence on the FW transverse wavenumber. The crosses mark the maxima of one Fourier order. (b) Linear fit of the SH transverse wavenumbers to the experimentally obtained maxima.

the necessary momentum conservation. The phase mismatch is defined solely by the longitudinal propagation constants of the modes in the waveguides. As we have seen above, a coupled WGA assembled from multiple waveguides is a two-dimensional (2D) system, whose eigenmodes are also characterized by a transverse wavenumber. This transverse momentum has to be conserved in SHG in WGAs. Hence, for the transverse wavenumbers the relation

$$\kappa^{\text{SH}} = 2\kappa^{\text{FW}} + 2m\pi, m \in \mathbb{N} \quad (3.13)$$

holds [119], where the second term on the right side accounts for the wavevector induced by the periodic WGA.

This relation can be verified experimentally. To this end a WGA with $d = 13.5 \mu\text{m}$ is utilized and a wide FW beam with an FWHM width of $110 \mu\text{m}$ or ≈ 7 waveguides is coupled to the WGA. This beam excites several FW supermodes centered around the transverse wavenumber of the exciting beam, which is conserved upon excitation. For the used wide input beam the resulting spatial spectrum is narrow enough to enable the description of the beam dynamics by the properties of only the supermode in the center of the spectrum [37] (see also Section 4.1). We measure the energy distribution of the SH in the spatial spectrum in dependence on the angle of the FW beam and hence, in dependence on the FW wave vector with the setup explained in Section 2.4.2. The FW wavelength for each angle is set to achieve maximum SHG for a certain interaction (the connection between the transverse wavenumber and the phasematching wavelength will be studied in the next section). Fig. 3.7 shows a result which is obtained for the interaction of the FW00 with the SH10 mode. The transverse wavenumber of the FW is determined by monitoring the FW output in the spatial domain according to Ref. [37].

For each transverse FW wavenumber a periodic pattern in the SH spatial spectrum

is visible, where each maximum corresponds to one value of m in Eq. (3.13). The differences between these maxima are 2π . The crosses in Fig. 3.7(a) mark transverse SH wavenumbers which correspond to the same m . In Fig. 3.7(b) the points marked in Fig. 3.7(a) are plotted again with a linear fit. We find, as expected, that the ratio between κ^{SH} and κ^{FW} is 2.04 ± 0.05 , which confirms the relation Eq. (3.13).

3.2.2 Second harmonic generation

In the previous section the relation of the transverse wavenumbers of a generated SH wave and the generating FW field in a WGA was discussed. Now the efficiency of the SHG process of the FW and SH supermodes defined by the transverse wavenumbers κ_0 and $2\kappa_0$ is investigated.

Nonlinear propagation of cw light in a WGA is described in the spatial domain by

$$\begin{aligned} i \frac{\partial}{\partial z} u_n^{\text{FW}} + c^{\text{FW}} [u_{n+1}^{\text{FW}} + u_{n-1}^{\text{FW}}] &= -\omega^{\text{FW}} \sum_{\nu'} \chi_{\text{eff}}^{\nu'} u_n^{\text{FW}*} u_n^{\nu'} \exp[-i\Delta\beta^{\nu'} z], \\ i \frac{\partial}{\partial z} u_n^{\nu} + c^{\nu} [u_{n+1}^{\nu} + u_{n-1}^{\nu}] &= -\omega^{\text{FW}} \chi_{\text{eff}}^{\nu} [u_n^{\text{FW}}]^2 \exp[i\Delta\beta^{\nu} z]. \end{aligned} \quad (3.14)$$

Similar to the derivation of Eq. (3.4) in 3.1.2, we assume that the conversion efficiency is rather low. Hence, the FW solution in the spatial domain is the linear solution Eq. (3.12). This linear solution is inserted as a driving wave in the right hand side of the SH equation of Eqs. (3.14) and the resulting equation is Fourier transformed according to Eq. (3.8) to give

$$\left[i \frac{\partial}{\partial z} + 2c^{\nu} \cos(2\kappa_0) \right] \tilde{u}^{\nu}(z) = -\omega^{\text{FW}} \chi_{\text{eff}}^{\nu} [\tilde{u}^{\text{FW}}]^2 \exp[i(2k^{\text{FW}}(\kappa_0) + \Delta\beta^{\nu})z]. \quad (3.15)$$

We solve Eq. (3.15) in the Fourier domain using the ansatz

$$\tilde{u}^{\nu}(z) = \tilde{A}^{\nu}(z) \exp[ik^{\nu}(2\kappa_0)z], \quad (3.16)$$

where we set the longitudinal wavenumber of the considered SH supermode to $k^{\nu}(2\kappa_0) = 2c^{\nu} \cos(2\kappa_0)$. The resulting SH amplitude after a fixed length L , obtained by direct integration analog to Eq. (3.4) under the assumption that $\tilde{A}^{\nu}(0) = 0$, is

$$\tilde{A}^{\nu}(L) = \tilde{A}_0^{\nu} \{ \exp[iL(2k^{\text{FW}}(\kappa_0) - k^{\nu}(2\kappa_0) + \Delta\beta^{\nu})] - 1 \} \quad (3.17)$$

with

$$\tilde{A}_0^{\nu} = \frac{\omega^{\text{FW}} \chi_{\text{eff}}^{\nu} [\tilde{u}^{\text{FW}}]^2}{[2k^{\text{FW}}(\kappa_0) - k^{\nu}(2\kappa_0) + \Delta\beta^{\nu}]}. \quad (3.18)$$

This solution has a similar structure as Eq. (3.4) in the spatial domain. Hence, the

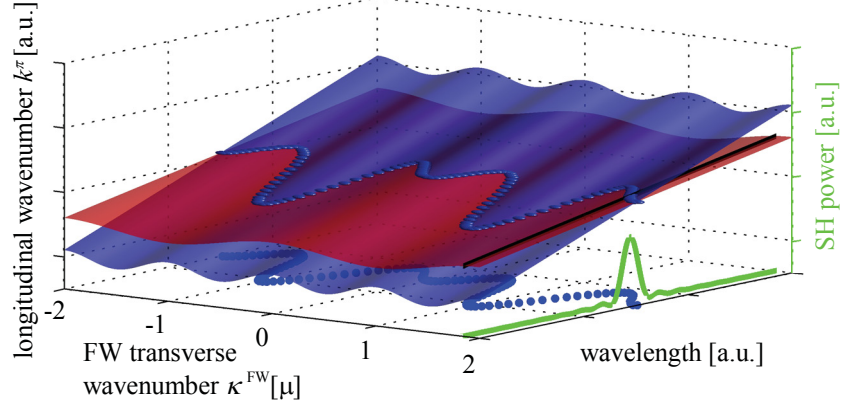


Figure 3.8: Scheme of the SH and FW bands in dependence on the wavelength, which are represented by the blue and red planes, respectively. The line of phasematching is marked by the blue spheres. The measurement procedure to determine the SH band is sketched by the black line and the green measured SH power.

generated SH power is

$$P^\nu(L) = \frac{1}{2} (\omega^{\text{FW}} \chi_{\text{eff}}^\nu)^2 P^{\text{FW}}(0)^2 \text{sinc}^2 \left(\frac{[2k^{\text{FW}}(\kappa_0) - k^\nu(2\kappa_0) + \Delta\beta^\nu] L}{2\pi} \right). \quad (3.19)$$

The maximum SH power is now achieved for [119]

$$2k^{\text{FW}}(\kappa_0) - k^\nu(2\kappa_0) + \Delta\beta^\nu = 4c^{\text{FW}} \cos(\kappa_0) - 2c^\nu \cos(2\kappa_0) + \Delta\beta^\nu = 0. \quad (3.20)$$

The SHG output power again shows the resonant sinc-dependence, however, the position of the maximum now depends also on the diffraction relations of the used bands. Thus the maximum SHG is achieved for different wavelengths depending on the transverse FW wavenumber.

3.2.3 Band characterization

The condition Eq. (3.20) for efficient SHG allows for the measurement of the bands if the properties of one waveguide mode and its supermodes are known. For example, from $\beta_0^{\text{FW00}}(\lambda^{\text{FW}})$ and the corresponding coupling constant $c^{\text{FW00}}(\lambda^{\text{FW}})$ all SH bands which interact with the FW00 band can be measured. A scheme of the FW and SH bands and the suggested measurement procedure is shown in Fig. 3.8. A very narrow spatial spectrum of FW00 supermodes (ideally only single κ^{FW}) is excited by a cw-laser. The laser wavelength is swepted and hence states with different longitudinal wavenumbers k_0 (visualized by the black line in Fig. 3.8) are excited. If the excited FW supermode has a vanishing phase mismatch to an SH band, efficient SHG takes place. SH power is generated according to Eq. (3.19) (green line) and recorded with a suitable detector. This procedure is repeated for many transverse wavenumbers. The

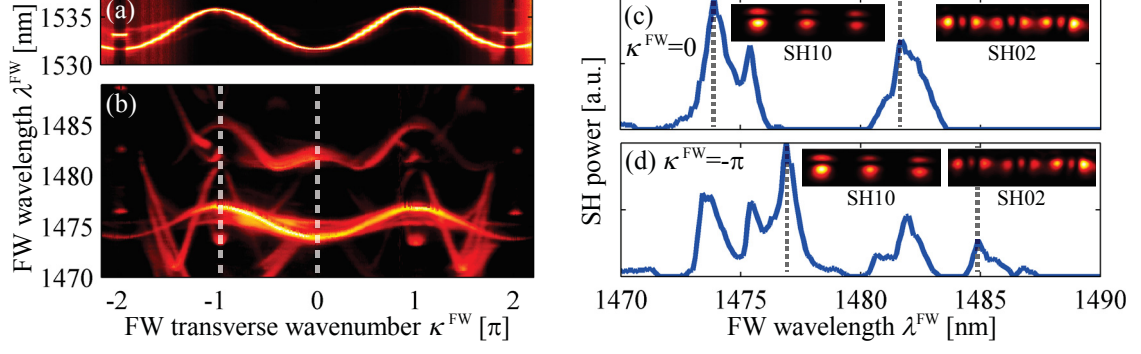


Figure 3.9: Normalized measured SH power in dependence on the FW wavelength and transverse wavenumber for the interactions of the FW00 band with (a) the SH00 band and (b) different higher SH bands. (c) SH power at $\kappa^{\text{FW}} = 0$ as indicated by the dashed line in (b). The insets show SH mode profiles measured at the wavelengths which are indicated by the dotted lines. (d) Same as (c) for $\kappa^{\text{FW}} = -\pi$.

minimal range of FW transverse wavenumbers which allows for the determination of the complete SH band is $0 \leq \kappa^{\text{FW}} \leq \pi$. Eq. (3.20) is fulfilled at the wavelengths of maximum SH power for each κ^{FW} , and the longitudinal wavenumbers of the SH band at the corresponding wavelengths can be determined according to

$$k_0^\nu(2\kappa, \lambda_{\text{PM}}^{\text{SH}}) = 2k_0^{\text{FW}}(\kappa_0, \lambda_{\text{PM}}^{\text{FW}}) + \frac{2\pi}{\Lambda_{\text{QPM}}}. \quad (3.21)$$

This scheme is realized with the setup for automatic beam angle tuning described in Section 2.4.2. The vertical width of the elliptical beam is $110 \mu\text{m}$, which ensures a narrow spatial spectrum of the FW after excitation. The experiments are carried out at room temperature, avoiding additional inhomogeneities introduced by the oven's temperature profile. Compared to other results presented in this thesis, this results in smaller phasematching wavelengths.

In Figs. 3.9(a,b) the SH power measured in dependence on the FW wavelength and the transverse wavenumber is shown for SHG with different SH bands for an array with $d = 12.5 \mu\text{m}$. The measured data shows clear continuous traces which, however, cannot readily be assigned to interactions with a certain SH band. To relate the measured signal to specific SH bands we measure the mode profile $|e_{\text{array}}^\nu(x, y, \kappa^{\text{FW}})|^2$ of the generated SH supermodes for a few values of κ^{FW} . In Figs. 3.9(c,d) we show the measured SH powers for $\kappa^{\text{FW}} = 0$ and $-\pi$ corresponding to the marked cuts across the data of Fig. 3.9(b). The insets show mode profiles of the supermodes measured at the marked wavelengths, which in each waveguide match to the mode profiles $|e^\nu(x, y)|^2$ of single waveguides found in Section 3.1.1. Hence, we conclude that traces visible for all $\kappa^{\text{FW}} \in \{-\pi, \pi\}$ in Fig. 3.9(b) stem from nonlinear interaction of the FW00 band with the SH10 and SH02 bands, whereas the SH in Fig. 3.9(a) is generated in the SH00

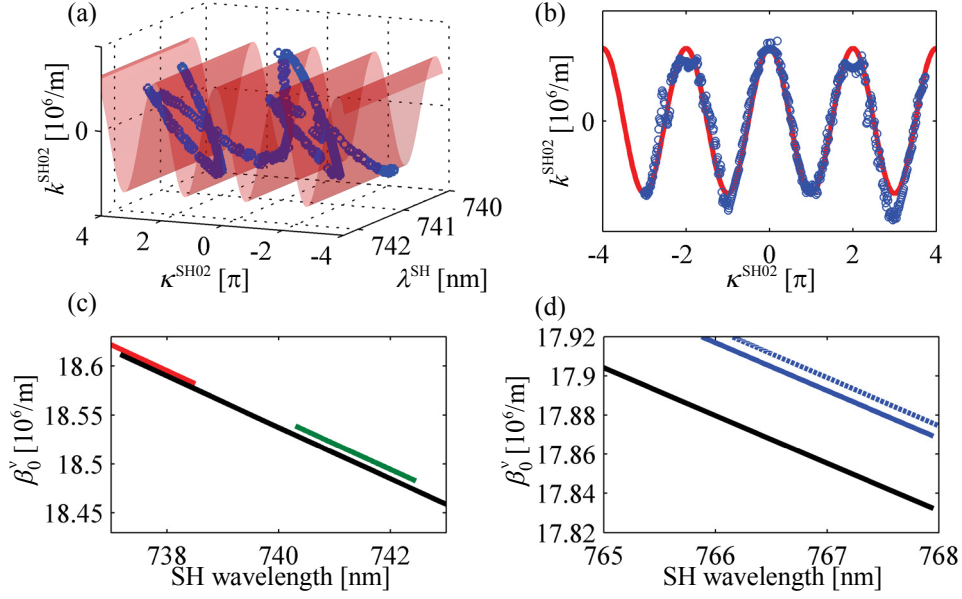


Figure 3.10: (a) Measured (blue dots) and fitted (red plane) longitudinal wavenumbers k^{SH02} in dependence on wavelength and transverse wavenumber for the SH02 band. (b) 2D view of the data from (a). (c,d) Retrieved wavenumber $\beta_0^\nu(\lambda)$ for the SH10 (red), SH02 (green), and SH00 (solid blue) bands compared to the bulk propagation constant (black) derived from [172]. The dotted blue line in (d) shows numerically calculated propagation constants for the SH00 mode.

mode. The additional signals in Fig. 3.9(b) are due to excitation of the FW01 mode, which is guided only for higher transverse wavenumbers. These higher order FW mode enables additional degenerate or non-degenerate interactions together with the FW00 mode. Hence, various SH modes similar to the observations in Section 3.1.2 are excited. For transverse wavenumbers κ^{FW} close to zero, the FW01 mode is not excited and not guided and hence does not take part in efficient nonlinear interactions.

To quantitatively characterize the measured SH bands, the known FW00 band is used. Section 3.1.1 showed, that the dispersion of the eigenmodes is mostly determined by the host material lithium niobate. The refractive index dispersion due to the titanium indiffusion and the mode dispersion can be neglected. Hence, the longitudinal FW00 wavenumbers from Eq. (3.11) are approximated using the propagation constant in bulk lithium niobate, which is known from measurements [172], instead of the propagation constant of the FW00 mode in a single waveguide. The FW coupling constants of $c^{\text{FW00}} = 237/\text{m}$ for $\lambda^{\text{FW}} = 1475 \text{ nm}$ and $c^{\text{FW00}} = 280/\text{m}$ for $\lambda^{\text{FW}} = 1534 \text{ nm}$ are determined by measuring the Green's function of the WGA [20, 49, 174] in dependence on the wavelength. This allows for the calculation of the longitudinal wavenumbers of the SH modes at the phasematching wavelengths according to Eq. (3.21). This set of points is fitted with the analytical model Eq. (3.11) for the SH wavenumbers, assuming that $c^\nu(\lambda) = \text{const.}$ and $\beta_0^\mu(\lambda) = F^\mu\lambda + F_0^\mu$ in the measured wavelength range. In Fig. 3.10(a) the measured and fitted slowly varying longitudinal wavenum-

period d	SH00	SH02	SH10	SH00	SH02	SH10
	experiment			simulation		
12.5 μm	34	329	19	0.5	225	17
13.0 μm	5	172	16	0.2	120	12
13.5 μm	3	81	1	0.1	63	8

Table 3.1: Measured and simulated coupling constants c^ν in $1/m$ of the SH00, SH02 and SH10 modes for three different WGAs.

ber $k^\nu = k_0^\nu - \beta_0$ for the SH02 mode is plotted in dependence on the wavelength and transverse wavenumber. In Fig. 3.10(b) only the dependence of the same quantities on the transverse wavenumber is plotted. The cos-shape of the measured values is obvious and underlined by the good correspondence to the fitted function. From the fit we determine the coupling constant of the SH02 mode in this array to $c^{\text{SH02}} = (329 \pm 10)/m$. The error in the coupling constant results from imperfections in the QPM structure of the used sample, which leads to broader tuning curves without a well defined maximum [see Figs. 3.10 (c,d)].

The derived propagation constants β_0^ν for the three SH bands detected in Fig. 3.9 are shown in Figs. 3.10(c,d) in comparison to the propagation constant in bulk lithium niobate [172]. Since the SH00 mode (solid blue line) has the highest effective index, its propagation constant has the largest difference to the bulk value, which is the cut-off for waveguiding in a single waveguide. The dotted blue line in Fig. 3.10(d) indicates values for β_0^{SH00} which are calculated with the finite element method according to Section 3.1.1. The used diffusion parameters are $D_x = 3.8 \mu\text{m}$ and $D_y = 4.45 \mu\text{m}$. The difference between measured and simulated propagation constants is approximately $10^4/m$ for the whole covered wavelength range and is mainly due to the use of the bulk propagation constant for the FW modes in the analysis.

The bands in WGAs with different periods d are measured. The results for the coupling constant of various SH bands are summarized in Tab. 3.1 and compared with simulation results. The simulations are conducted for the whole periodic system, where the coupling constants are determined by fitting a cos function to the calculated bands. We find that the simulated values for the coupling constant are in general smaller than the measured ones, even when the accuracy of the measurement procedure of $\approx \pm 10/m$ is considered. The reason for this may be threefold. First, to determine the diffusion constants (as described in Section 3.1.1) we have to measure the mode profile with a CCD camera which is limited in both sensitivity and dynamic range. This leads to an underestimation of the mode widths and hence the diffusion constants, which finally yields smaller calculated modes and coupling constants. Second, the cos-shape of the bands itself is an approximation, as seen in Section 2.2. Derivations of the FW bands from the cos-shape will lead to errors and hence to a systematic deviation

from the simulation result. Third, inhomogeneities in the diffusion profiles may lead to additional scattering in neighboring waveguide, thus increasing the coupling in the experiment especially for the modes with small coupling constants.

The presented method for band characterization can be used for bands of any shape as long as one reference band is known. The only condition for the reference band is that it is truly three-dimensional in the space of $\{\lambda, \kappa^\mu, k_0^\mu\}$. For example, in the system with essentially linear dispersion treated experimentally above, a reference band with $c^{\text{FW}} = 0$ is not sufficient, since information obtained in the 2D subspace defined by this band is not enough to reconstruct fully three-dimensional bands.

In the experimental demonstration above we extract only data at the phasematching wavelengths $\lambda_{\text{PM}}^{\text{FW}}$. This limits the applicability of the method to wavelengths very close to the phasematching wavelengths. However, since the tuning curve Eq. (3.5) has well defined minima for fixed phase differences of $\Delta\beta^\nu L = 2m\pi, m \in \mathbb{N}$, the unknown band could in principle be measured at each of these minima. Hence, the spectral bandwidth of the measurements can be enhanced for sufficiently sensitive detection schemes. This makes the presented method interesting for systems other than WGAs which have a quadratic nonlinearity, e.g. photonic crystals [175–177]. Methods to measure the bands in photonic crystals exist, but usually require complicated techniques [39, 178] to precisely excite the guided mode under test. The excitation of guided modes is achieved by disturbing the evanescent tails of the modes and therefore introduce coupling to external radiation. In turn, also the dispersion relation of the measured system will be perturbed. Alternative measurement methods use specialized samples [179] or are restricted to radiating modes [180]. Additionally, all of these methods can only retrieve bands for the excitation wavelength and are therefore not ideally suited for parametric systems. The method described here is relatively easy to implement, does almost not disturb the bands due to the weak nonlinear excitation mechanism and can characterize all guided modes.

We note, that in order to determine only the coupling constants of bands in weakly coupled WGAs, a far easier measurement is sufficient. We just need to compare the phasematching wavelengths to a certain SH mode ν in a single waveguide $\lambda_{\text{PM}}^{\text{FW}}$ with that in a WGA $\lambda_{\text{PM}}^{\text{FW}} + \Delta\lambda$, which has to be measured with $\kappa^{\text{FW}} = 0$. In the former case $\Delta\beta^\nu(\lambda_{\text{PM}}^{\text{FW}}) = 0$ is fulfilled, whereas in the latter situation

$$4c^{\text{FW}} - 2c^\nu + \Delta\beta^\nu(\lambda_{\text{PM}}^{\text{FW}} + \Delta\lambda) = 0 \quad (3.22)$$

holds [see Eq. (3.20) and Eq. (3.10)]. For small $\Delta\lambda$ we assume

$$\begin{aligned} \Delta\beta^\nu (\lambda_{\text{PM}}^{\text{FW}} + \Delta\lambda) &\approx \left. \frac{d(\Delta\beta^\nu)}{d\lambda} \right|_{\lambda_{\text{PM}}^{\text{FW}}} \Delta\lambda \\ &\approx -\frac{\pi\Delta\lambda}{(\lambda_{\text{PM}}^{\text{FW}})^2} \left. \frac{d}{d\lambda} \left[2n(\lambda^{\text{FW}}) - n\left(\frac{\lambda^{\text{FW}}}{2}\right) \right] \right|_{\lambda_{\text{PM}}^{\text{FW}}}, \end{aligned} \quad (3.23)$$

where we again neglect the modal dispersion. As shown in Fig. 3.10 this is well justified and the quantity Eq. (3.23) can be calculated from measured values of the refractive indices for bulk lithium niobate [172]. Hence the coupling constant c' can be calculated according to Eq. (3.22). An additional measurement of the same tuningcurve for $\kappa^{\text{FW}} = \pi$ allows for the calculation of both c^{FW} and c' from the two obtained shifts of the phasematching wavelengths.

Chapter summary

In this chapter first the properties of single waveguides, which are the building blocks of the later used WGAs, were reviewed. The different guided FW and SH modes and their dispersion relations were calculated numerically. The numerical results were confirmed by SHG measurements in single waveguides, revealing that SH is generated in higher order modes if phasematching occurs. The maximum efficiency of these interactions was shown to depend on the mode symmetry and the mode overlap.

For SHG in WGAs it was shown, both theoretically and experimentally, that the transverse SH wavenumber is twice the transverse FW wavenumber. Similar to the single waveguide, in WGAs efficient SHG in forward direction is only possible if the longitudinal wavenumbers of FW and SH coincide. However, in WGAs the wavelengths where this condition is fulfilled depend on the FW transverse wavenumber. This was used to map SH bands in WGAs by measuring the SH output intensity in dependence on the FW wavelength and transverse wavenumbers. The result is used to characterize the SH bands [FS26]. The presented method can be expanded to determine the linear bands in other periodic systems with parametric interactions. Finally, an easy to use method to determine only the coupling constants of the SH bands in weakly coupled WGAs was devised. This method is utilized throughout the present thesis.

Chapter 4

Multiple mode interactions

In the last chapter very weak nonlinear interactions taking place for small phase mismatches were studied. In this case only energy exchange from one frequency component to another is induced. The feedback of the SH to the FW was neglected and the different FW-SH interactions were treated independently from each other. Additionally, the investigations were restricted to the propagation and nonlinear interaction of plane waves in WGAs. In this chapter we will treat the more general case of spatially finite beams propagating with strong nonlinear interactions in waveguide arrays with several SH modes. The WGAs used in the experiments support only one FW mode across the whole range of transverse wavenumbers (see Section 3.2) and hence, the investigations are restricted to one FW band. In contrast, the number of guided SH modes is much larger, as was shown in Chapter 3. However, to obtain a general insight into the properties of nonlinear propagation for several SH modes, it is not useful to start from the complete SH bandstructure as shown in Fig. 3.6, which will be different for each waveguide array. Rather we will concentrate on two closely spaced SH bands with somewhat generalized properties as sketched in Fig. 4.1, which are likely to exist for different sample geometries. The difference of the propagation constants of the two modes taken into account is assumed to be much smaller than the mismatch to other SH modes. This allows for the neglect of other SH modes. Nonlinear effects in systems with more SH bands can be extrapolated if the propagation in the two-band WGA is understood.

The model is realized experimentally for the SH₁₀ and SH₀₂ modes in the used samples. Fig. 4.1 introduces the system investigated in this chapter, together with all relevant (normalized) parameters. In Fig. 4.1(a) we plot a sketch of the array together with the mode profiles of the considered modes. The numerically calculated phase mismatches are shown in Fig. 4.1(b). Depending on the wavelength, the mismatches either have the same or different signs. Finally, Fig. 4.1(c) shows sketches of the bands of the participating modes to clarify their relative position to each other. The modes again obey the limitations of the coupled mode equations, where especially direct linear

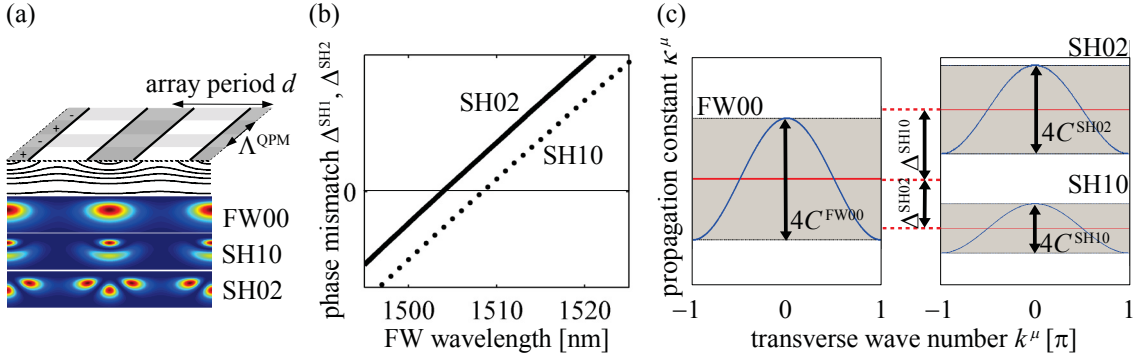


Figure 4.1: (a) Sketch of the experimental system with the refractive index profile of the periodically poled waveguide structure and the array modes. (b) Simulated phase mismatch between FW00 and SH02 (solid) or SH10 (dotted) mode versus the FW wavelength. (c) Bands of FW (left) and SH (right) modes.

interactions between the SH modes are neglected. The difference between the phase mismatches of the two modes is approximately constant, since the mode dispersion is mainly induced by the dispersion of the host material, which is the same for all SH modes. However, the phase mismatches can be adjusted by changing the wavelengths or sample temperatures.

To understand the nonlinear effects described later, in Section 4.1 the properties of linear propagation of beams with finite width in WGAs are reviewed. In Section 4.2 solitons are described, the stationary localized solutions of the propagation equations, which can be seen as fixed points of the nonlinear beam evolution. From these results, predictions for more general cases of dynamic beam evolution are deduced and tested experimentally in Section 4.3.

4.1 Linear propagation of finite beams

In Section 3.2 we found, that the wavenumbers of discrete plane waves in WGAs obey the diffraction relation Eq. (3.10), which describes a cosine dependence of the longitudinal on the transverse wavenumber. The discrete plane waves, which are also eigenmodes of the linear WGA, are spatially infinite. In the experiments described in Chapter 3 a very narrow spatial spectrum was excited by using broad beams, which was treated as a single plane wave. However, the experimentally more common and scientifically also very interesting schemes feature the excitation of only one or a few waveguides. In this case several discrete plane waves are excited and have to be taken into account.

The amplitudes in the real space and the spatial spectrum are connected by the Fourier transform Eq. (3.8). Hence, for narrower excitation the spatial spectrum is getting wider. For the excitation of only a single waveguide, the spatial spectrum

$\tilde{u}^\mu(\kappa, 0)$ is constant for all transverse wavenumbers κ . In this case, the solution of the propagation equation Eq. (3.9) is [20, 174]

$$u_{n,n'}^\mu(z) = i^{n-n'} J_{n-n'}(2c^\mu z), \quad (4.1)$$

where the n and n' denote the excited and observed waveguide, respectively and $J_{n-n'}$ is the Bessel function of the first kind of $(n - n')$ th order. This result describes the well known phenomenon of discrete diffraction and represents the Green's function of the waveguide array. Hence, it can in principle be used to calculate the amplitudes in the waveguide array for arbitrary input conditions with the Green's function approach [20]. However, except for very narrow excitations, a different approach, which also yields precise results, is more intuitively understandable.

Following Ref. [37], spatial linear beam propagation in waveguide arrays is approximated analog to the description of pulse dispersion in Section 2.1. For beams with a narrow spatial spectrum the diffraction relation Eq. (3.10) is expressed as a Taylor-expansion to the 2nd order around the central transverse wavenumber κ_0 ,

$$k^\mu(\kappa) = k^\mu(\kappa_0) + \left. \frac{dk^\mu}{d\kappa} \right|_{\kappa_0} (\kappa - \kappa_0) + \frac{1}{2} \left. \frac{d^2k^\mu}{d\kappa^2} \right|_{\kappa_0} (\kappa - \kappa_0)^2. \quad (4.2)$$

Inserting this approximation in Eq. (3.9) and transforming back to the real domain with Eq. (3.8) we obtain an equation which formally describes linear beam dynamics in the spatial domain

$$\left[i \frac{\partial}{\partial z} + k^\mu(\kappa_0) - i \left. \frac{dk^\mu}{d\kappa} \right|_{\kappa_0} \frac{\partial}{\partial n} - \frac{1}{2} \left. \frac{d^2k^\mu}{d\kappa^2} \right|_{\kappa_0} \frac{\partial^2}{\partial n^2} \right] u^\mu(z, n) = 0, \quad (4.3)$$

where n now appears as a continuous variable and $u^\mu(z, n) = u_n^\mu \exp(-i\kappa_0 n)$. Similar to Eq. (2.31) we conclude that the first derivative

$$\left. \frac{dk^\mu}{d\kappa} \right|_{\kappa_0} = -2c^\mu \sin(\kappa_0) \quad (4.4)$$

describes the transverse velocity of the beam and the second derivative

$$\left. \frac{d^2k^\mu}{2d\kappa^2} \right|_{\kappa_0} = -2c^\mu \cos(\kappa_0) \quad (4.5)$$

determines the beam broadening or diffraction and is hence termed the diffraction coefficient. The linear beam dynamics under this kind of diffraction relation has been discussed in great detail in Refs. [36, 37]. A few characteristic features are important for the nonlinear effects which we will study later. For a transverse wavenumber $\kappa_0 = 0$ the transverse velocity is zero and the diffraction has its minimum value of $-2c^\mu$. The

sign of the diffraction is the same as in natural materials which consequently is termed normal diffraction. Anomalous diffraction, which is not possible in natural materials, occurs in waveguide arrays for transverse wavenumbers of $\kappa_0 = \pi/d$, where the value of the diffraction coefficient is $2c^{\mu}$. As we will see later, the sign of the diffraction will critically influence the structure and excitation of nonlinear wave patterns. In the next sections solitons will be studied, which emerge when the diffraction induced by the band structure is balanced by nonlinear effects.

4.2 Stationary solutions

Bright spatial solitons are localized stationary solutions of the nonlinear propagation equations for cw-light, in contrast to nonlinear plane waves, which are spatially extended. Solitons are important for the analysis of nonlinear beam propagation since they represent fixed points in the phase space of dynamic solutions. They exist for parameters where the diffraction of finite beams is canceled by a nonlinearity induced phase shift.

In quadratic nonlinear interactions, phase shifts in the different frequency components can be achieved by utilizing subsequent frequency mixing processes, so-called cascaded interactions [113]. In this thesis, the involved processes are SHG and difference frequency generation (DFG) of SH and FW photons. Specifically, SH photons are generated and converted back to the FW by DFG after a certain propagation distance. In the case of phase mismatched propagation these processes lead to nonlinear phase shifts in both components due to the different phase velocities [64]. If only FW is present at the input, the SH wave is periodically generated and converted back to FW (as in Fig. 3.3). For very large mismatches, the effective cascading nonlinearity for the FW beam is similar to a Kerr nonlinearity [68, 69] with tunable sign and strength depending on the phase mismatch. However, for smaller mismatches qualitative differences to Kerr systems appear, since a larger amount of FW is converted to SH and back and the phase of the FW does not change continuously but stepwise [64].

To propagate as spatial solitons, the phase velocities of all frequency components in all spatial parts of the beam have to be equal. This is achieved if the phase distortions introduced to the localized beam by diffraction are balanced by the phase shifts due to cascading [181]. The influence of the linear and nonlinear phase shifts on the propagation of cw light in a homogeneous lossless WGA with two SH modes is described

by the normalized coupled mode equations

$$\begin{aligned}
i\frac{\partial A_n^{\text{FW}}}{\partial z} + C^{\text{FW}}(A_{n+1}^{\text{FW}} + A_{n-1}^{\text{FW}}) + (\gamma^{\text{SH1}} A_n^{\text{SH1}} + \gamma^{\text{SH2}} A_n^{\text{SH2}}) (A_n^{\text{FW}})^* &= 0, \\
i\frac{\partial A_n^{\text{SH1}}}{\partial z} + C^{\text{SH1}}(A_{n+1}^{\text{SH1}} + A_{n-1}^{\text{SH1}}) - \Delta^{\text{SH1}} A_n^{\text{SH1}} + \gamma^{\text{SH1}} (A_n^{\text{FW}})^2 &= 0, \\
i\frac{\partial A_n^{\text{SH2}}}{\partial z} + C^{\text{SH2}}(A_{n+1}^{\text{SH2}} + A_{n-1}^{\text{SH2}}) - \Delta^{\text{SH2}} A_n^{\text{SH2}} + \gamma^{\text{SH2}} (A_n^{\text{FW}})^2 &= 0.
\end{aligned} \tag{4.6}$$

To get insight into the mechanism of the two SH processes acting on the same FW it is instructive to analyze Eqs. (4.6) in the limit of large mismatches. We assume, that the SH coupling is vanishing ($C^{\text{SH1}} = C^{\text{SH2}} = 0$), such that the effective nonlocality of the cascaded nonlinear processes [182] can be neglected. Then, following a standard procedure developed for cascaded quadratic nonlinear interactions [113], we derive a discrete nonlinear Schrödinger equation [47] with effective Kerr-type nonlinearity for the FW amplitudes

$$i\frac{\partial A_n^{\text{FW}}}{\partial z} + C^{\text{FW}}(A_{n+1}^{\text{FW}} + A_{n-1}^{\text{FW}}) + \Gamma |A_n^{\text{FW}}|^2 A_n^{\text{FW}} = 0. \tag{4.7}$$

The strength of the effective nonlinearity is

$$\Gamma = \frac{(\gamma^{\text{SH1}})^2 \Delta^{\text{SH2}} + (\gamma^{\text{SH2}})^2 \Delta^{\text{SH1}}}{\Delta^{\text{SH1}} \Delta^{\text{SH2}}}. \tag{4.8}$$

The resulting effective nonlinearity is focusing ($\Gamma > 0$) or defocussing ($\Gamma < 0$) when both mismatches are positive ($\Delta^{\text{SH1}}, \Delta^{\text{SH2}} > 0$) or negative ($\Delta^{\text{SH1}}, \Delta^{\text{SH2}} < 0$), respectively. For focusing [47, 49] and defocusing [149, 183, 184] third-order nonlinearities the existence of spatial discrete solitons was shown in WGs with Kerr- and photorefractive nonlinearity, respectively. Hence, we also expect the existence of solitons in these parameter ranges. However, for mismatches of different signs [$\text{sgn}(\Delta^{\text{SH1}}) \neq \text{sgn}(\Delta^{\text{SH2}})$] the coefficient Γ may have either sign and crosses zero for

$$\left(\frac{\gamma^{\text{SH1}}}{\gamma^{\text{SH2}}}\right)^2 = -\frac{\Delta^{\text{SH1}}}{\Delta^{\text{SH2}}}. \tag{4.9}$$

The vanishing of the nonlinear coefficient is a feature which is not possible in a system with Kerr nonlinearity or cascaded nonlinearity involving only one SH mode. Hence, in this parameter region, where the signs of the two mismatches are different, the nonlinear propagation will be defined through the competition between the two SH interactions, and the beam's self-interaction and soliton formation are expected to demonstrate novel features.

In the following the stationary solutions of Eqs. (4.6) are analyzed first for a simplified case without linear coupling and later for the complete system. Although all equa-

tions are derived for general values of the linear and nonlinear coupling strengths, in the calculated examples $C^{\text{FW}} = C^{\text{SH1}} = C^{\text{SH2}}$ and equal normalized nonlinear strengths of $\gamma^{\text{SH1}} = \gamma^{\text{SH2}} = 1$ are assumed. This is justified also experimentally, since these parameters are, even if they are not exactly equal, of the same order. The difference of the phase mismatches is fixed to $\Delta^{\text{SH1}} - \Delta^{\text{SH2}} = 9$. This value is of the same magnitude than realized in the experiment, yet is somewhat smaller to allow for more detailed numerical calculations.

4.2.1 Stationary solutions for single waveguides

To get physical insight into the properties of the stationary solutions of Eqs. (4.6), we first consider the case of $C^{\text{FW}} = C^{\text{SH1}} = C^{\text{SH2}} = 0$. This describes the situation of a single waveguide, but may also serve as an approximation for the case of strong nonlinear interactions, when the solitons are effectively localized in a single waveguide (see e.g. [102, 106]). Then,

$$\begin{aligned} i \frac{\partial A^{\text{FW}}}{\partial z} + (\gamma^{\text{SH1}} A^{\text{SH1}} + \gamma^{\text{SH2}} A^{\text{SH2}}) (A^{\text{FW}})^* &= 0, \\ i \frac{\partial A^{\text{SH1}}}{\partial z} - \Delta^{\text{SH1}} A^{\text{SH1}} + \gamma^{\text{SH1}} (A^{\text{FW}})^2 &= 0, \\ i \frac{\partial A^{\text{SH2}}}{\partial z} - \Delta^{\text{SH2}} A^{\text{SH2}} + \gamma^{\text{SH2}} (A^{\text{FW}})^2 &= 0. \end{aligned} \quad (4.10)$$

Since the neighboring waveguides are decoupled, the waveguide number n is dropped. The stationary solutions have the following form

$$\begin{aligned} A^{\text{FW}}(z) &= A_0^{\text{FW}} \exp(ibz), \\ A^{\text{SH1}}(z) &= A_0^{\text{SH1}} \exp(2ibz), \\ A^{\text{SH2}}(z) &= A_0^{\text{SH2}} \exp(2ibz). \end{aligned} \quad (4.11)$$

The real parameter b defines the propagation constant of all three components due to nonlinear synchronization and A_0^{FW} , A_0^{SH1} , and A_0^{SH2} are the real valued stationary amplitudes. After inserting this ansatz into Eqs. (4.10), we derive the following solutions for the amplitudes

$$\begin{aligned} (A_0^{\text{FW}})^2 &= \frac{2b(b - \Delta^{\text{SH1}}/2)(b - \Delta^{\text{SH2}}/2)}{[(\gamma^{\text{SH1}})^2 + (\gamma^{\text{SH2}})^2](b - B_0)}, \\ A_0^{\text{SH1}} &= \frac{b(b - \Delta^{\text{SH2}}/2)\gamma^{\text{SH1}}}{[(\gamma^{\text{SH1}})^2 + (\gamma^{\text{SH2}})^2](b - B_0)}, \\ A_0^{\text{SH2}} &= \frac{b(b - \Delta^{\text{SH1}}/2)\gamma^{\text{SH2}}}{[(\gamma^{\text{SH1}})^2 + (\gamma^{\text{SH2}})^2](b - B_0)}, \end{aligned} \quad (4.12)$$

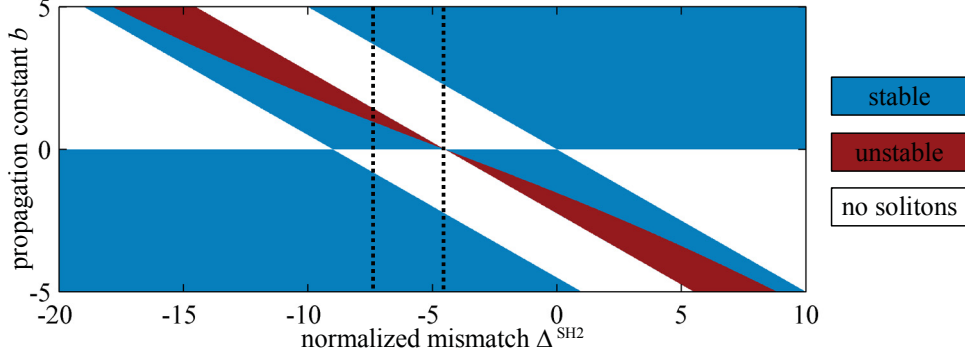


Figure 4.2: Existence and stability domains of stationary solutions for a single uncoupled waveguide with $C^{\text{FW}} = C^{\text{SH1}} = C^{\text{SH2}} = 0$. Stable solutions are indicated by blue and unstable by red shading. In the white domains no stationary solutions exist. The dashed lines indicate the soliton families shown in Fig. 4.3.

with

$$B_0 = \frac{(\Delta^{\text{SH1}}\Psi + \Delta^{\text{SH2}}(1 - \Psi))}{2} \quad \text{and} \quad \Psi = \frac{(\gamma^{\text{SH2}})^2}{[(\gamma^{\text{SH1}})^2 + (\gamma^{\text{SH2}})^2]}. \quad (4.13)$$

As will become evident later, B_0 is the propagation constant where the contributions of the two SH processes cancel each other. Real valued stationary solutions, which we are interested in, exist only when $(A_0^{\text{FW}})^2 \geq 0$. Regions of existence of real valued stationary solutions are plotted in Fig. 4.2 in dependence on the propagation constant b and the mismatch Δ^{SH2} . For all Δ^{SH2} , real solutions can be found in three domains of the parameter b . For the two semi-infinite domains $b < \min(0, -\Delta^{\text{SH1}}/2)$ and $b > \max(0, -\Delta^{\text{SH2}}/2)$, the solutions resemble those of a system with only one SH resonance [101]. Both nonlinear processes act in the same way, mimicking a single nonlinear resonance and we call the ensuing localized states cumulative solitons. A new solution domain is introduced due to competition between the two nonlinear processes for $-\Delta^{\text{SH1}}/2 < b < -\Delta^{\text{SH2}}/2$ and $|b| \leq |B_0|$ and consequently solutions in this domain are called competitive solitons. For $\Delta^{\text{SH2}} = -\Delta^{\text{SH1}}$ ($\Delta^{\text{SH2}} = -4.5$ in the depicted examples) this solution domain becomes a δ -distribution since $B_0 = 0$. The δ -peak coincides with the linear propagation constant of the FW mode, and hence competitive solitons do not exist for this mismatch.

In Fig. 4.3 we plot properties of the calculated families of stationary solutions for (a,b,c) $\Delta^{\text{SH2}} = -7.5$ and (d,e,f) $\Delta^{\text{SH2}} = -4.5$. The powers of the individual components μ , $P^\mu = |A^\mu|^2$ and of the complete solution $P = P^{\text{FW}} + P^{\text{SH1}} + P^{\text{SH2}}$ are plotted in Fig. 4.3(a,d). For $\Delta^{\text{SH2}} = -7.5$ three branches of the solutions exist for distinct ranges of the propagation constant. The powers of all components asymptotically go to infinity for $b \rightarrow B_0$ due to the competition between the two SH processes. For propagation constants close to B_0 the remaining effective nonlinear strength is very weak and large

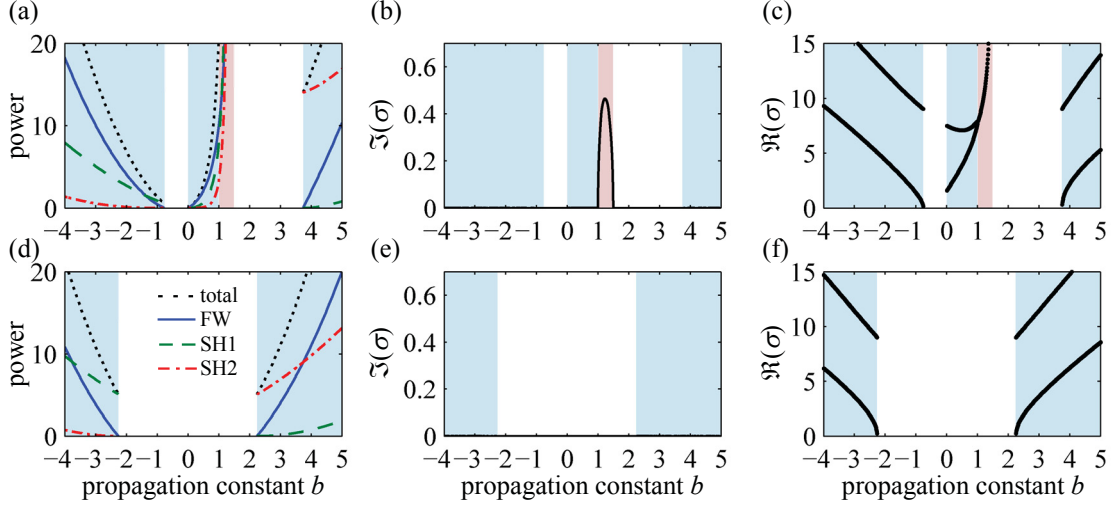


Figure 4.3: Families of stationary solutions for the single uncoupled waveguide with $C^{\text{FW}} = C^{\text{SH1}} = C^{\text{SH2}} = 0$ for (a,b,c) $\Delta^{\text{SH2}} = -7.5$, and (d,e,f) $\Delta^{\text{SH2}} = -4.5$. (a,d) Total power (black dotted line) and power of the FW (blue solid), SH1 (green dashed), and SH2 (red dash-dotted) components. (b,e) Imaginary part and (c,f) real part of the instability parameter σ . Stable solutions are indicated by blue and unstable solutions by red shading.

powers are necessary to maintain the soliton. This is in sharp contrast to normal SHG (only one SH component, $\gamma^{\text{SH2}} = 0$), where all powers are finite for finite propagation constants. A boundary of the existence domain and a singularity in the power are features also found for solitons in WGAs with saturable nonlinearity [185]. Hence, in the vicinity of a propagation constant where the nonlinearities compensate each other, they mimic a saturable system. Here an increase of the power does not lead to an increase in the soliton propagation constant.

The cumulative solution branches for the mismatches shown in Fig. 4.3 both bifurcate from the SH modes and hence exhibit a nonzero power threshold [22, 101]. The solution branch introduced through competition extends to zero power, where it bifurcates from the FW band. For all families with $-(\Delta^{\text{SH1}} - \Delta^{\text{SH2}}) < \Delta^{\text{SH2}} < 0$ the only branch of solutions with zero power threshold is generated through competition of the two phase-mismatched SHG processes. However, for $\Delta^{\text{SH2}} = -(\Delta^{\text{SH1}} - \Delta^{\text{SH2}})/2$ only the solutions on the cumulative branches exist, and no thresholdless solution can be obtained [see Fig. 4.3(d)]. This corresponds to the condition in Eq. (4.9), obtained in the cascading approximation, for $\gamma^{\text{SH1}} = \gamma^{\text{SH2}} = 1$.

We investigate the stability of the calculated solutions by linear stability analysis

using the ansatz

$$\begin{aligned} A^{\text{FW}}(z) &= \exp(ibz) (A_+^{\text{FW}} e^{i\sigma^* z} + A_-^{\text{FW}} e^{-i\sigma z} + A_0^{\text{FW}}), \\ A^{\text{SH1}}(z) &= \exp(2ibz) (A_+^{\text{SH1}} e^{i\sigma^* z} + A_-^{\text{SH1}} e^{-i\sigma z} + A_0^{\text{SH1}}), \\ A^{\text{SH2}}(z) &= \exp(2ibz) (A_+^{\text{SH2}} e^{i\sigma^* z} + A_-^{\text{SH2}} e^{-i\sigma z} + A_0^{\text{SH2}}), \end{aligned} \quad (4.14)$$

where the $(A_0^{\text{FW}}, A_0^{\text{SH1}}, A_0^{\text{SH2}})$ are the stationary solutions, variables with superscripts ‘ \pm ’ denote small perturbations, and the instability parameter σ characterizes the perturbation dynamics. Inserting this ansatz in Eqs. (4.10) and taking into account only the first order terms of the small perturbations leads to an eigenvalue problem for the value of σ which we solve numerically. In our case we obtain six generally complex eigenvalues for each propagation constant, which are distributed symmetrically with respect to the real axis. Depending on the value of the eigenvalues, the obtained solutions fall into different categories [186]. If the eigenvalue is real, the perturbation in ansatz Eqs. (4.14) is not growing and the corresponding eigenmode is called stable. Purely imaginary eigenvalues σ correspond to unstable and complex σ to oscillatory unstable eigenmodes. The initial soliton is called unstable for a certain propagation constant b if one of the eigenvalues for this b has a positive imaginary part, $\Im(\sigma) > 0$. Regions of instability exist for the solution branch with competition and are plotted with red shading in Figs. 4.2 and Fig. 4.3. The imaginary part of the instability parameter $\Im(\sigma)$ is shown in Fig. 4.3(b). The instability appears due to the collision of two eigenvalues σ at $b \simeq 1$, as seen in the real part $\Re(\sigma)$, which is presented in Fig. 4.3(c). The point of collision marks an upper boundary for the propagation constant of stable competitive solitons. The corresponding upper boundary for their power, as seen in Fig. 4.3(a), depends on the mismatch. Physically, this instability is rooted in the competitive balance of the two SH processes. For the high powers close to B_0 , even a small change in the powers leads to excess phase shifts induced by one of the nonlinear processes. This disturbs the balance and leads to soliton decay.

4.2.2 Discrete spatial solitons

In the last section we deduced the basic properties of the stationary solutions of Eqs. (4.6) for the analytically solvable case of decoupled equations. Now the full coupled system is analyzed. The ansatz for localized stationary solutions reads

$$\begin{aligned} A_n^{\text{FW}}(z) &= A_{0n}^{\text{FW}} \exp(ibz), \\ A_n^{\text{SH1}}(z) &= A_{0n}^{\text{SH1}} \exp(2ibz), \\ A_n^{\text{SH2}}(z) &= A_{0n}^{\text{SH2}} \exp(2ibz). \end{aligned} \quad (4.15)$$

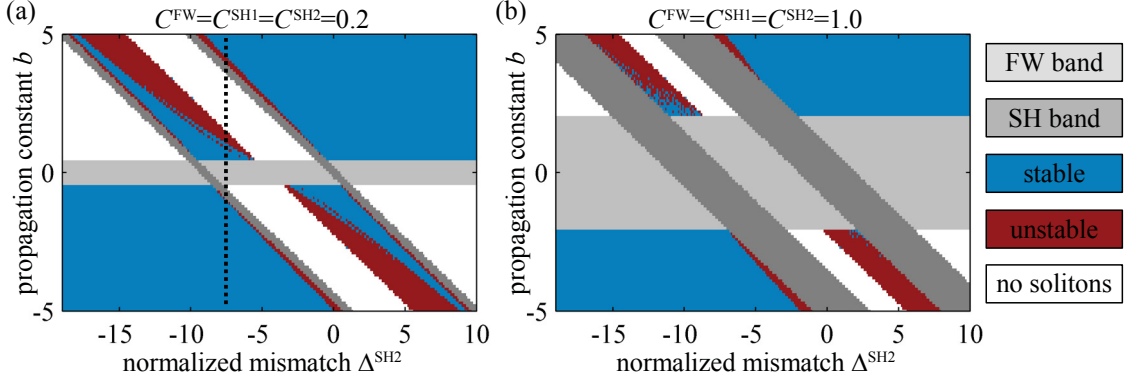


Figure 4.4: Soliton existence domains for (a) $C^{\text{FW}} = C^{\text{SH}1} = C^{\text{SH}2} = 0.2$ and (b) $C^{\text{FW}} = C^{\text{SH}1} = C^{\text{SH}2} = 1.0$. Stable solutions are indicated by blue and unstable solutions by red shading. In the white domains no stationary solutions exist. Light and dark gray shading indicates the FW and SH bands, respectively. The dashed line indicates the soliton family shown in Fig. 4.5.

Insertion of this ansatz into Eqs. (4.6) leads to a nonlinear system of equations which is solved numerically for A_{0n}^{FW} , $A_{0n}^{\text{SH}1}$, and $A_{0n}^{\text{SH}2}$. Here only odd solitons are treated. Even solitons for quadratic nonlinear interactions with only one SH component have been shown to exist in the same parameter regions as their odd counterparts, however they are always unstable [101, 105]. Even discrete solitons always decay in odd solitons and hence, beam dynamics is in general determined by the odd solutions. It is noted though, that the decay length may be long enough to detect characteristic features of even solitons in experiments.

The linear stability of the obtained odd stationary solutions is investigated similar to the single waveguide by inserting the perturbed solution

$$\begin{aligned}
 A_n^{\text{FW}}(z) &= \exp(ibz) \left(A_{+n}^{\text{FW}} e^{i\sigma^* z} + A_{-n}^{\text{FW}} e^{-i\sigma z} + A_{0n}^{\text{FW}} \right), \\
 A_n^{\text{SH}1}(z) &= \exp(2ibz) \left(A_{+n}^{\text{SH}1} e^{i\sigma^* z} + A_{-n}^{\text{SH}1} e^{-i\sigma z} + A_{0n}^{\text{SH}1} \right), \\
 A_n^{\text{SH}2}(z) &= \exp(2ibz) \left(A_{+n}^{\text{SH}2} e^{i\sigma^* z} + A_{-n}^{\text{SH}2} e^{-i\sigma z} + A_{0n}^{\text{SH}2} \right),
 \end{aligned} \tag{4.16}$$

into Eqs. (4.6) and solving the eigenvalue problem for the instability parameter σ , taking into account only the first order terms in the small perturbations.

Fig. 4.4 shows the domains of soliton existence and stability for two different coupling strengths, where domains of stable (unstable) solutions are blue (red) and the linear bands are gray. Similar to the case of the isolated waveguide analyzed in Section 4.2.1 above, we find three different solution branches for a wide domain of the mismatches. Cumulative solutions, which resemble the staggered or unstaggered solitons of a WGA with only one SHG resonance [101], are found for $b < \min(-2C^{\text{FW}}, -\Delta^{\text{SH}1}/2 - 2C^{\text{SH}1})$ or $b > \max(2C^{\text{FW}}, -\Delta^{\text{SH}2}/2 + C^{\text{SH}2})$, respectively. The third branch is formed due to nonlinear competition for $-\Delta^{\text{SH}1}/2 + C^{\text{SH}1} <$

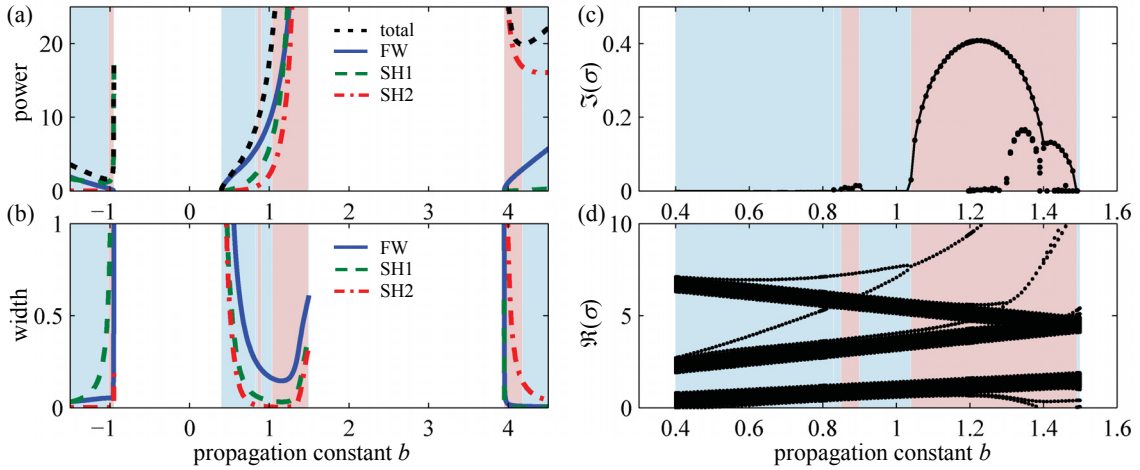


Figure 4.5: Soliton families for $C^{\text{FW}} = C^{\text{SH1}} = C^{\text{SH2}} = 0.2$ and $\Delta^{\text{SH2}} = -7.5$ (dashed line in Fig. 4.4). (a) Power and (b) width of the calculated solutions. Plotted are the overall power (black dotted line) and the respective quantities for the individual components, FW (blue solid), SH1 (green dashed), and SH2 (red dash-dotted). Stable solutions are indicated by blue and unstable solutions by red background. (c) Imaginary and (d) real part of the instability parameter for the competitive solutions.

$b < -\Delta^{\text{SH2}}/2 - C^{\text{SH2}}$ and $|b| \leq |B_0|$. However, solutions in this domain can now only exist for $|b| > 2|C^{\text{FW}}|$ due to the extended linear bands, which prevent the formation of nonlinear localized states. This leads to a gap in the existence of solutions for the competitive branch and hence to a range of mismatches where no solutions with zero power threshold exist.

In Fig. 4.5 we show numerically calculated properties of the soliton family at $\Delta^{\text{SH2}} = -7.5$ for a coupling strength of $C^{\text{FW}} = C^{\text{SH1}} = C^{\text{SH2}} = 0.2$. In Fig. 4.5(a) we plot the power of the solutions and the powers of its constituents vs. the propagation constant b . The solution power is determined by summing up the powers in the individual waveguides. Again we find a power threshold for the cumulative branches of the solutions, which bifurcate from the SH bands. Close to the bands the power of these solutions grows with decreasing propagation constants. According to the Vakhitov-Kolokolov criterion [187], we expect that such solutions with $\frac{dP}{d|b|} \leq 0$ are unstable, which is confirmed by the linear stability analysis. The existence of the only branch of solutions with zero power threshold, bifurcating from the FW band, is again induced by the competition between the two phase-mismatched nonlinear processes. For increasing propagation constant, the power of the competitive solitons increases monotonically and diverges for $b \rightarrow B_0$. Here, the increasing propagation constant moves towards the center between the two SH bands where the effects of the two competing nonlinear processes are almost compensated by each other and higher powers are necessary to maintain a soliton.

In Fig. 4.5(b) we plot the width of the components of the solutions, which we

calculate as the second moment of the power distribution in the waveguides. Close to the linear bands, the solitons resemble linear waves, hence their width is diverging when b approaches these boundary of the existence domains. In the competitive solitons, the width of all components is large close to the linear bands and first decreases with increasing propagation constant b . It increases to a finite value when b approaches the upper existence boundary. This is explained by a cascaded saturation of the effective nonlinearity in the different waveguides. Close to B_0 , the large central amplitude of the odd soliton can not grow any larger due to the competition induced saturation of the nonlinearity. Consequently the power in neighboring waveguide grows and the solitons are getting wider. The same effect was reported for spatial solitons in WGAs with saturable nonlinearities [185].

The imaginary and real parts of the perturbation eigenvalue, $\Im(\sigma)$ and $\Re(\sigma)$, are plotted in detail for the competitive branch in Figs. 4.5(c) and (d), respectively. Similar to the case of the single uncoupled waveguide analyzed in Section 4.2.1 above, we find a range of propagation constants between $b = 1$ and $b = 1.5$ where collisions between the eigenvalues lead to instability. This is again due to disturbances of the balance between the competing SHG processes. Additionally, for a small band of propagation constants around $b = 0.85$ we reveal soliton instability due to coupling to a linear band [188, 189]. Here the propagation constant $2b - \Re(\sigma)$ of the instability mode is phase-matched to the SH band defined by C^{SH2} , hence energy exchange between the soliton and the linear band can take place. We note, that due to the spatially extended nature of the linear states, the numerical calculation for the instability growth rate $\Im(\sigma)$ is sensitive to the finite number of waveguides of the simulated WGA, which is 128 here. For larger coupling constants, many small domains of instability appear, as seen in Fig. 4.4(b). These are induced by the three mechanisms described above, where the Vakhitov-Kolokolov type instabilities are only found close to the bifurcation points of the solutions from the SH bands (dark gray).

The different instabilities have physically different origins, resulting in different typical soliton decay scenarios. This is shown by numerically solving Eqs. (4.6) with slightly perturbed stationary solutions as starting conditions: $(A_n^{\text{FW}}, A_n^{\text{SH1}}, A_n^{\text{SH2}}) = (A_{0n}^{\text{FW}}, A_{0n}^{\text{SH1}}, A_{0n}^{\text{SH2}}) \pm 0.01 (A_{0n}^{\text{FW}}, A_{0n}^{\text{SH1}}, A_{0n}^{\text{SH2}})$, where either plus or minus is applied to all components of the excitation. The intensity distributions of all three components are plotted in Fig. 4.6 vs. the propagation distance for typical instability regimes of the soliton family at $C^{\text{FW}} = C^{\text{SH1}} = C^{\text{SH2}} = 0.2$ and $\Delta^{\text{SH2}} = -7.5$ (as in Fig. 4.5). Fig. 4.6(a) shows results for the Vakhitov-Kolokolov type instability at $b = -0.95$ and an input with decreased power. The perturbed soliton input is quickly decaying into linear waves. A completely different dynamics is observed for the same stationary solution with slightly raised input power, plotted in Fig. 4.6(b). Here the intensity oscillates during propagation. These two types of instability dynamics have been described

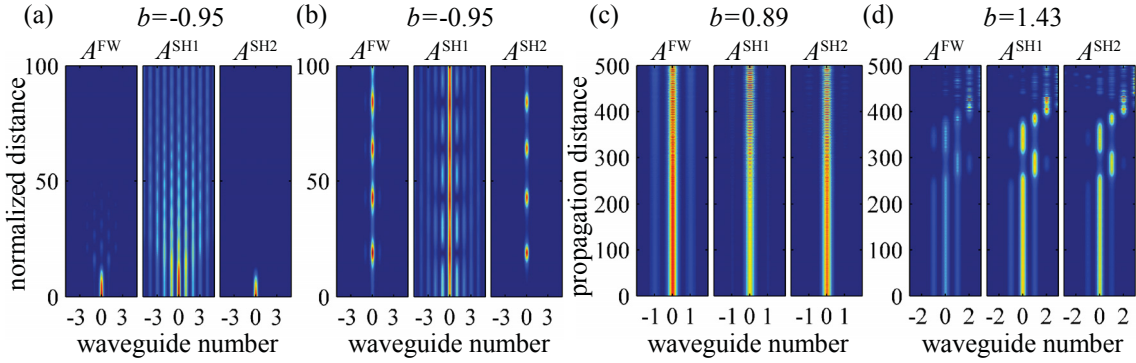


Figure 4.6: Evolution of $|A_n^{\text{FW}}|^2$ (left panels), $|A_n^{\text{SH1}}|^2$ (center panels), and $|A_n^{\text{SH2}}|^2$ (right panels) of perturbed solutions for $C^{\text{FW}} = C^{\text{SH1}} = C^{\text{SH2}} = 0.2$ and $\Delta^{\text{SH2}} = -7.5$. Shown are the dynamics for the Vakhitov-Kolokolov type instability at $b = -0.95$ for input powers (a) smaller and (b) larger than the powers of the solutions. (c) Dynamics for the band instability at $b = 0.89$ and (d) for the collision induced instability at $b = 1.43$.

earlier for the Vakhitov-Kolokolov type instability of quadratic solitons with one SH component in bulk lithium niobate [190]. The oscillation for raised input power can be explained as pulsation around a new stable solution, which can be excited due to the higher power. The other types of instabilities show qualitatively the same behavior for increased and decreased input power, hence we plot only results for decreased power. At $b = 0.89$ [Fig. 4.6(c)] the solution interacts with an SH band. The energy oscillates rapidly between the different components of the soliton without evident changes in the shape of the excitation. Only after long propagation one can recognize that energy is slowly radiating away from the soliton via linear waves in the A_n^{SH2} component. This is consistent with the very small calculated values of $\Im(\sigma)$ for this case [see Fig. 4.5(c)]. For the collision caused instability at $b = 1.43$ we plot the propagating intensities in Fig. 4.6(d). Here the soliton decays abruptly through all three components after initial propagation without apparent changes.

The dynamics of perturbed stable spatial solitons is also investigated. They always show small oscillations in the initial stages of the propagation, resulting in radiation losses of light. However, these losses always result in the propagation of a stationary localized wavepacket. A complete decay or long-lasting oscillations are not observed.

4.3 Spatial dynamics

The analysis of the preceding section revealed, that stable solitons with two SH components exist for large domains of the mismatch. The aim of this section is the experimental verification of this finding. The main experimental problem is the excitation of the stationary states, which consist of phase locked FW and SH components. Like in the setup used here, most experiments excite only with the FW wave (with Ref. [106]

being the exception). The reason for this is the necessity of a fixed phase difference between FW and SH that is hard to stabilize experimentally. An FW only beam initially excites states on the linear FW bands, which can dynamically shape into solitons during the nonlinear propagation. Since the solitons bifurcate from the upper or lower edges of the linear bands, the most common excitation schemes feature excitation at $\kappa^{\text{FW}} = 0$ and $\kappa^{\text{FW}} = \pi$. To shape the Gaussian excitation towards a soliton, the necessary SH components have to be generated and the diffraction has to be arrested [105]. The latter is accomplished, if the phase shifts induced by cascaded nonlinear processes balance the diffraction Eq. (4.5). For $\kappa^{\text{FW}} = 0$, where the diffraction is normal, the effective nonlinearity acting on the FW needs to be focusing. The sign of the combined effective nonlinearity is estimated in the large mismatch limit Eq. (4.7). It is focusing for $\Gamma > 0$, which is fulfilled if both mismatches are positive for wavelengths above the phasematching resonances or between the two resonances close to the low wavelength phasematching resonance. The focusing nonlinearity increases the propagation constant of the FW beam. Thus, nonlinear states with propagation constants above the linear FW band (see Fig. 4.4) are accessible for excitation with $\kappa^{\text{FW}} = 0$. Along the same line of arguments we conclude that solitons below the linear FW band can only be generated when we excite states with $\kappa^{\text{FW}} = \pi$ and use defocusing nonlinearity. It is noted, that the specific way of excitation may be different for solutions not discussed here, e.g. flat-top or truncated nonlinear Bloch-waves [111, 191, 192].

From the discussion above we conclude, that in typical experiments solitons are generated in a dynamical process. This favors the excitation of solitons which are close to the exiting FW beam. Hence, broad solitons with a small SH component and a propagation constant close to the linear FW band are most likely excited. However, other localized states can be generated, depending on the input power, beam shape, and mismatch, though the excitation efficiency might be very small [193]. Also dynamic nonlinear propagation effects appear, which do not result in soliton excitation.

4.3.1 Simulations with fundamental wave excitation

The experimental excitation is modeled by numerically integrating Eqs. (4.6) with an input FW distribution of Gaussian shape. The aim of the simulations is to allow for the comparison of the dynamical beam self-action with the results of the stationary analysis. Hence, all parameters are similar to the last section and only cw light is considered. The FWHM of the intensity profile is 4 array periods and the phase difference between adjacent waveguides is set to either 0 or π . As in the dynamical simulations of Section 4.2.2 we consider the case of $C^{\text{FW}} = C^{\text{SH1}} = C^{\text{SH2}} = 1$. The propagation is simulated over 10 coupling lengths.

The results of the numerical experiments for the excitation with $\kappa^{\text{FW}} = 0$ are sum-

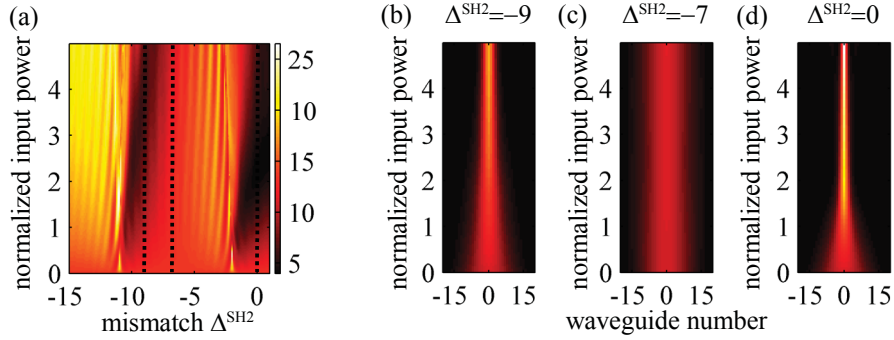


Figure 4.7: (a) Width of the FW output signal in dependence on the mismatch and input peak power for excitation with $\kappa^{\text{FW}} = 0$. (b,c,d) Output intensity distributions in dependence on the input peak power for $\Delta^{\text{SH2}} = -9$, $\Delta^{\text{SH2}} = -7$, and $\Delta^{\text{SH2}} = 0$, denoted by the dotted lines in (a).

marized in Fig. 4.7. To comprehensively describe the nonlinear effects in dependence on input peak power and input mismatch, the output width as the second moment of the output intensity distribution is calculated and plotted in Fig. 4.7(a). Focusing of the beam during propagation is a sign for soliton excitation and is observed for two ranges of mismatches, $\Delta^{\text{SH2}} \approx -9$ and $\Delta^{\text{SH2}} \geq -1$. This corresponds to the regions of mismatches where we showed the existence of stationary solutions bifurcating from the upper edge of the FW band in Section 4.2.2 [see Fig. 4.4(b)]. The output intensity distributions in dependence on the input peak power for several mismatches are shown in Figs. 4.7(b-d). For the mismatches $\Delta^{\text{SH2}} = -9$ and $\Delta^{\text{SH2}} = 0$ the diffraction induced broadening is clearly counteracted by the nonlinearity, and the output beam width is becoming smaller with increasing peak power. Here spatial solitary waves are excited. The case depicted in Fig. 4.7(b) corresponds to the competitive soliton described in the preceding section, whereas in Fig. 4.7(d) the excitation of a cumulative soliton is shown. The cumulative solitons are narrower than their competitive counterpart for similar powers. This results from the different widths of the stationary solutions and from the different effective nonlinear strengths. In the cumulative case, larger nonlinear phase shifts can be achieved and hence solitons with larger propagation constants and smaller width are accessible for the investigated excitation powers.

For a fixed power and mismatches between -9 and -2 an increase of the output width with increasing Δ^{SH2} is observed. At $\Delta^{\text{SH2}} \approx -2$ the excited linear FW states are phasematched to the SH2 mode, which marks the boundary of the competitive regime. The oscillations in the width stem from interferences between the original propagating FW and parts of the FW backconverted from SH components which are not locked to the FW radiation [194–196]. This effect is avoided with pulsed light, due to the group velocity mismatch between SH and FW. For one particular mismatch, $\Delta^{\text{SH2}} = -7$ in our case, the output FW width stays the same regardless of the input power due to the

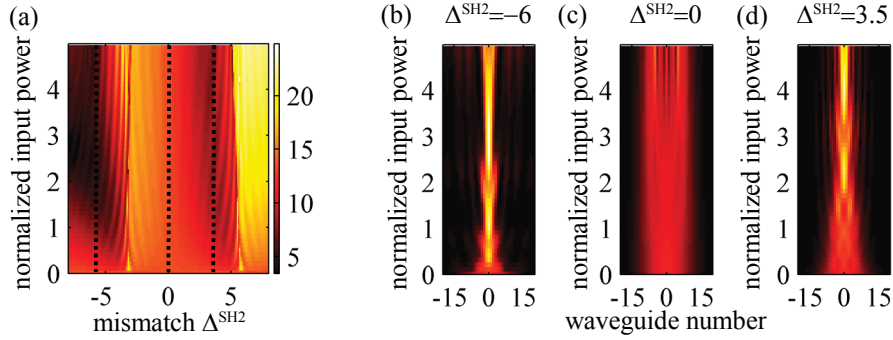


Figure 4.8: (a) Width of the FW output signal in dependence on the mismatch and input peak power for excitation with $\kappa^{\text{FW}} = \pi$. (b,c,d) Output intensity distributions in dependence on the input peak power for $\Delta^{\text{SH2}} = -6$, $\Delta^{\text{SH2}} = 0$, and $\Delta^{\text{SH2}} = 3.5$, denoted by the dotted lines in (a).

competition of the two nonlinear processes. The corresponding output intensity distributions are shown in Fig. 4.7(c). This behavior can be understood easily in the large mismatch approximation. If condition Eq. (4.9) is fulfilled, the propagation equation Eq. (4.7) becomes linear and diffraction is the only effect remaining. Consequently, the beam behaves like a linear beam and diffracts for all powers. If the strong assumption of large phase mismatch is lifted, step-like phase shifts of the FW are induced by both SH components [64]. In general they do not compensate completely, however, the beam periodically undergoes small positive and negative phase shifts and no noticeable spatial effects remain.

Similar results for the excitation with $\kappa^{\text{FW}} = \pi$ are plotted in Fig. 4.8, where the width of the output FW distribution is shown in Fig. 4.8(a). For $\kappa^{\text{FW}} = \pi$ the diffraction of the linear beam is anomalous, in contrast to the case discussed above. Hence, to achieve similar nonlinear effects, a different sign of the effective nonlinearity is necessary. In accordance with our theoretical findings this leads to the result in Fig. 4.8(a), which qualitatively is flipped with respect to Fig. 4.7(a). Again two mismatch regions with focusing nonlinear effects can be observed. The corresponding power dependences of the output distributions are shown in Fig. 4.8(b) for the cumulative and in Fig. 4.8(d) for the competitive case, respectively. Compensation and the inhibition of spatial reshaping is found for $\Delta^{\text{SH2}} = 0$ between the phasematching resonances. The power dependence for this mismatch is depicted in Fig. 4.8(c).

In this section the possibility of exciting the solitons found in Section 4.2.2 with FW only input was investigated. Characteristic features in the width of the propagating wave packets were described and attributed to the solutions found before. Both cumulative and competitive solitons were excited. Additionally, a dynamic regime showing the complete suppression of spatial nonlinear effects was described. In the next section these phenomena will be studied experimentally.

4.3.2 Experimental realization

For the experimental verification of the phenomena discussed in the preceding sections we use a 71 mm long waveguide array with a period of $d = 15 \mu\text{m}$. In the necessary wavelength range around 1500 nm, this translates into a coupling constant for the FW00 mode of $c^{\text{FW}} = 80 \text{ m}^{-1}$. With a normalization length of $L_0 = 1/c^{\text{FW}} = 12.5 \text{ mm}$ the corresponding normalized coupling constant is $C^{\text{FW}} = 1$. The utilized SH modes are the SH02 and SH10 modes, which in a single waveguide are phasematched to the FW00 mode at wavelengths of 1500.77 nm and 1503.28 nm, respectively. This corresponds to a normalized difference in the mismatches of the two modes of $\Delta^{\text{SH02}} - \Delta^{\text{SH10}} = 20$. According to the measured phasematching wavelengths, the SH10 mode in the sample under investigation corresponds to the SH2 mode of the theoretical section. In contrast to the examples discussed above the coupling strengths of the SH modes differ from the one of the FW mode and from each other. With the techniques described in Chapter 3, the coupling constants are determined to be $c^{\text{SH02}} = 63 \text{ m}^{-1}$ and $c^{\text{SH10}} = 16 \text{ m}^{-1}$, which in normalized units is $C^{\text{SH02}} = 0.79$ and $C^{\text{SH10}} = 0.2$. According to our previous findings, this will slightly shift the lower boundaries of the regions of soliton existence, as was discussed in Section 4.2.2.

A more pronounced effect is expected from the difference of the nonlinear overlap integrals K^ν and hence the nonlinear coefficients γ^ν of the two interactions in the experiment. With the measurement method described in detail in Appendix B, we find for the SH10 mode that $K^{\text{SH10}} \approx 2.9 \cdot 10^8 \text{ V}^3/\text{m}$ and for the SH02 mode that $K^{\text{SH02}} \approx 1.9 \cdot 10^8 \text{ V}^3/\text{m}$. This translates to normalized quantities of $\gamma^{\text{SH10}} = 1$ and $\gamma^{\text{SH02}} = 0.66$, respectively. The imbalance in the nonlinear strengths will shift the existence boundary for the competitive solitons closer to the linear band of the weaker SH02 mode, according to both the cascading approximation Eq. (4.9) and the analytic condition for the existence boundary B_0 , Eq. (4.13). Thus, the existence domain for competing solitons with $b \geq 0$ shrinks, whereas it is larger for $b \leq 0$.

To experimentally characterize the beam dynamics we use pulses of 5.3 ps length. It has been shown, that for moderate powers the spatial dynamics of the beam is only weakly influenced by the temporal structure [196–198]. Specifically, the SH necessary for the nonlinear phase shifts is trapped under the FW pulse. Hence, although there always exists a small amount of SH generated at the sample input and propagating freely [196], spatial effects induced by GVM and GVD can be neglected. Thus, the sample output is interpreted as if it is generated by a cw beam. The same approach was used in Ref. [105].

The input beam is shaped into an elliptical input spot of 60 (3) μm horizontal (vertical) FWHM width. This corresponds to an FWHM of the excitation of 4 array periods. The captured output profiles of FW and SH in dependence on the FW input wave-

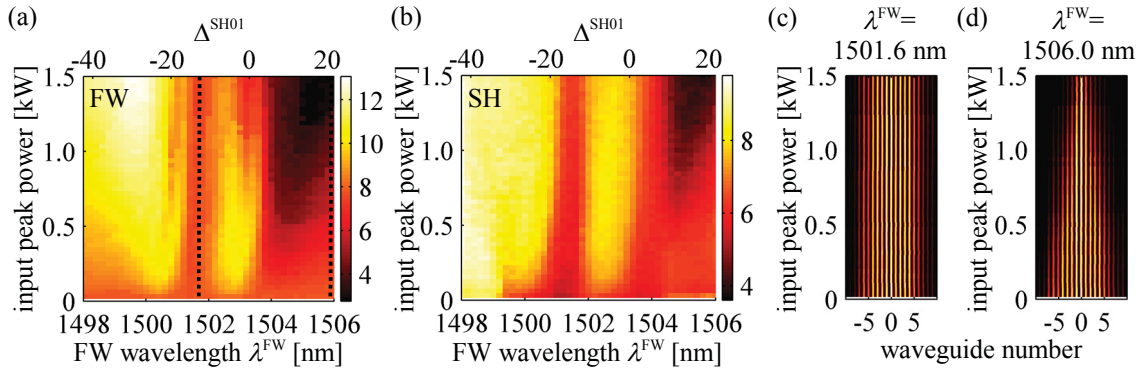


Figure 4.9: Measurement result for normal incidence ($\kappa^{\text{FW}} = 0$). Output width of the (a) FW and (b) SH beams measured in array periods in dependence on the input FW peak power and the FW wavelength. The upper abscissa gives the normalized mismatch of the SH10 mode for better comparison to the theoretical results of Section 4.2.2. (c) Power dependence of the FW output profile for the wavelength of nonlinearity inhibition, 1501.6 nm. (d) Power dependence of the FW output profile showing focusing for a wavelength of 1506 nm. The dotted lines in (a) mark the wavelengths of (c) and (d).

length and peak power are used to derive the width of the beam, again by calculating the second moment. Additionally, FW and SH mode profiles are evaluated to better understand the beam dynamics.

Fig. 4.9 shows experimental results for an excitation under normal incidence, corresponding to a transverse wavenumber of $\kappa^{\text{FW}} = 0$, where Fig. 4.9(a) shows the second moment width of the FW output intensity distribution. These results are qualitatively comparable to the result of the simulations in Section 4.3.1 for the same case, depicted in Fig. 4.7(a). Two wavelengths with increasing width already for small peak powers are identified at 1500.3 nm and 1502.8 nm. These are the phasematching wavelengths for this excitation. They are shifted to smaller wavelengths with respect to the single waveguide, as has been discussed in Section 3.2.3. The increase in width at the phasematching is due to the generation of SH, and hence energy extraction from the FW beam, predominantly in the center of the FW beam where the peak intensity is initially higher. Since the used sample is not exactly homogeneous, the phasematching regions are broader than expected from the cw simulations.

Focusing is found only for wavelengths above both phasematching resonances, which corresponds to the excitation of cumulative solitons with both SH modes. The corresponding dependence of the FW output intensity on the input power is shown in Fig. 4.9(d). Notably, the experimental results do not indicate the excitation of competing solitons. No decreasing width is measured between the phasematching resonances. This results from the inhomogeneity of the sample, which completely closes this existence window. Nevertheless, between the phasematching resonances, a wavelength where the width of the output beam is almost independent from the input power is

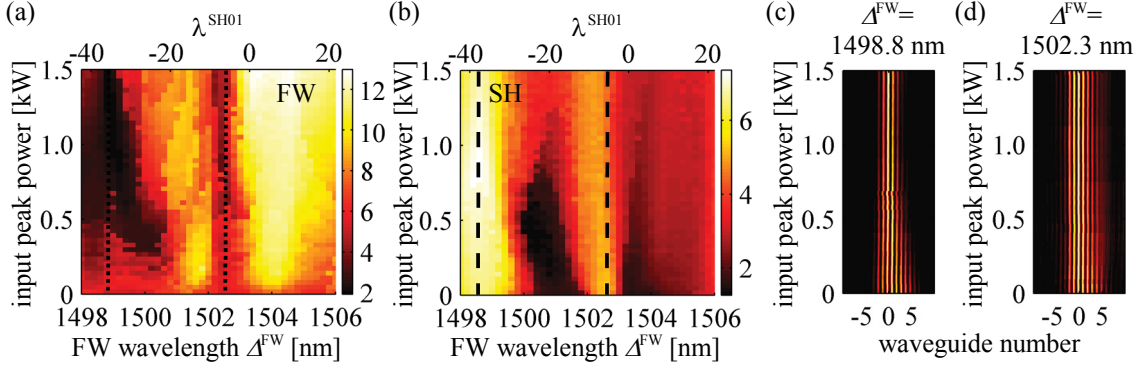


Figure 4.10: Measurement result for tilted incidence ($\kappa^{FW} = \pi$). Output width of the (a) FW and (b) SH beams measured in array periods in dependence on the input FW peak power and the FW wavelength. The upper abscissa gives the normalized mismatch to the SH10 mode for better comparison to the theoretical results of Section 4.2.2. (c) Power dependence of the FW output profile showing focusing for a wavelength of 1498.8 nm. (d) Power dependence of the FW output profile for the wavelength of nonlinearity inhibition, 1502.3 nm. The dotted lines in (a) indicate the wavelengths of (c) and (d) whereas the dashed lines in (b) mark phasematching to the SH11 and SH03 modes.

clearly visible and marked by the dashed line in Fig. 4.9(a). The measured intensity distributions for this wavelength are shown in Fig. 4.9(c), indeed confirming that no reshaping takes place and the beam propagates as if no nonlinearities were present in the system.

The width of the generated SH signal is depicted in Fig. 4.9(b). The dependence of the SH width on power and wavelength is in general similar to the FW results. However, due to quadratic dependence of the SH power on the FW power, the SH width is smaller than the FW width. The only discrepancy between FW and SH width occurs at the lowest measured wavelengths, where the FW width is increasing constantly with increasing powers whereas the SH width is staying constant but higher than for other wavelengths. The SH responsible for this large width is generated in the SH11 mode, which is found by separate measurements of the SH mode profiles. Almost no SH from the targeted modes SH02 and SH10 is found. The SH11 mode is strongly coupled and therefore spreads quickly across the array. However, the odd SH11 can not be generated by the even FW00 mode. Since no other guided FW supermodes exist in the array for $\kappa^{FW} = 0$, this can only be explained by non-degenerated interactions of the FW00 and odd radiating FW supermodes to the SH11 mode.

A measurement of the beam output width for different mismatches and input powers is also conducted for tilted excitation with $\kappa^{FW} = \pi$ and the main results are summarized in Fig. 4.10. As expected in Fig. 4.10(a) we again find a wavelength region of nonlinear focusing, now below both phasematching wavelengths, and a wavelength where the width stays almost constant for all powers. The corresponding FW

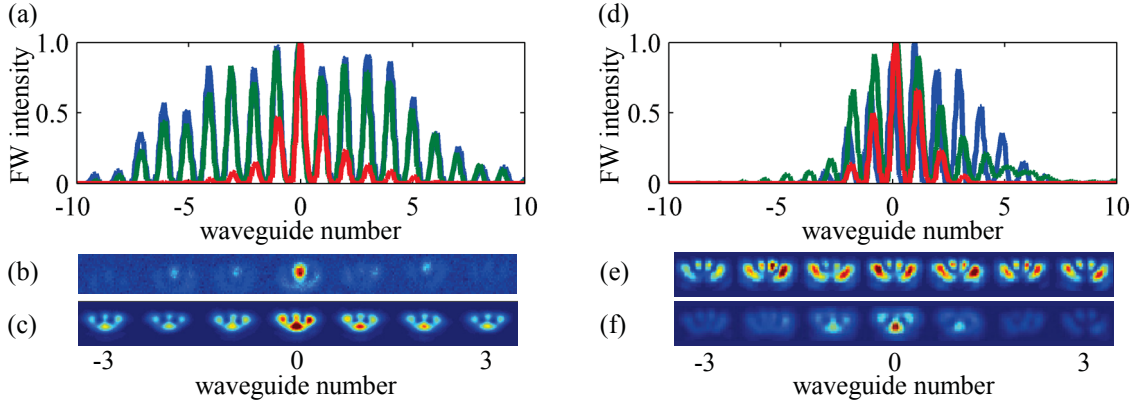


Figure 4.11: FW output profiles for linear propagation (blue), the inhibition of spatial nonlinear effects (green), and a cumulative soliton (red) for (a) $\kappa^{\text{FW}} = 0$ and (d) $\kappa^{\text{FW}} = \pi$. SH profiles at (b) 0.05 kW and (c) 1.3 kW for the wavelength of 1506 nm. SH profiles at (e) 0.05 kW and (f) 1.3 kW for the wavelength of 1498.8 nm.

intensities are shown in Fig. 4.10(c) and (d), respectively. We do not excite competing solitons. Although these measurements mostly confirm the predictions of the cw simulations from Section 4.3.1, the results are not as clear as in the case of incidence with $\kappa^{\text{FW}} = 0$. This is due to the fact that at the edge of the Brillouin zone the array supports two modes for the FW, which enables the generation of odd SH modes with high efficiency. The respective phasematching wavelengths are indicated by the dashed lines in Fig. 4.10(b). The large constant SH width in these regions is due to the large coupling constants of the generated SH modes SH11 and SH03.

In Figs. 4.11(a) and (d) we show FW output profiles of the described characteristic types of nonlinear beam propagation under the influence of two SH modes. For the case of $\kappa^{\text{FW}} = 0$ in Fig. 4.11(a) we find perfect agreement between the low power case (blue) and the case of nonlinearity inhibition (green) at 1.3 kW. Corresponding to the soliton (red) at 1506 nm, we also measured the mode profile of the generated SH beam at low and high peak powers, shown in Figs. 4.11(b) and (c), respectively. Although for the smaller power only very little SH is generated and the SH mode can not be clearly identified, the image shows that the generated SH modes are all even. For high power we clearly see, that the SH profiles are an interference of SH02 and SH10 modes, as expected. This serves as a proof that both SH modes are part of the cumulative soliton excited for $\kappa^{\text{FW}} = 0$ and that no other SH modes have a significant influence on the beam dynamics.

For the output profiles with $\kappa^{\text{FW}} = \pi$ in Fig. 4.11(d) we see, that the profiles for the linear case (blue) and the case of nonlinearity inhibition (green) are different. However, the spatial reshaping with competing nonlinearities is considerably smaller than for the cumulative case, where we again excite a soliton (red). The low power SH mode profiles for the soliton wavelength 1498.8 nm in Fig. 4.11(e) show, that the

generated SH mode is different from the ones taken into consideration up to now. Instead, the measured profiles correspond to the odd SH11 mode. This mode can only be generated if both FW00 and FW01 are present in the system, which is very likely with our type of excitation. The measured phasematching wavelength for this non-degenerated interaction is 1498.2 nm, very close to the soliton wavelength. Another non-degenerated SH resonance (SH mode profile not shown) is found at 1502.8 nm, which is very close to the inhibition wavelength. The differences between the results from Fig. 4.10 and the theoretical predictions and simulations can be explained by additional phaseshifts created by the two described non-degenerate interactions, which are not included in our theoretical model. However, the cumulative solitons can still be excited as predicted. In Fig. 4.11(f) we show the corresponding SH mode profiles, which in the center of the beam are an interference of SH02 and SH10 modes. The additional even SH11 mode can only be recognized in the wings of the SH beam. Differences in the mode profiles in the beam centers of Figs. 4.11(d) and (f) stem from unequal phase differences of the two SH modes which form the interference pattern.

Chapter summary

This chapter was devoted to the study of nonlinear beam propagation in WGAs with several SH modes. The analysis was simplified by taking into account only two modes, a scenario which is common in the experimentally investigated LiNbO₃ samples. First, the stationary solutions as fixed points of nonlinear dynamics were analyzed. They could be calculated analytically for single waveguides and numerically for WGAs. In both cases we found novel properties which do not appear for just one SH mode [FS9,FS25,FS29]. Two types of solitons were identified, cumulative solitons with larger magnitude of the propagation constants than both SH modes and competitive solitons where the propagation constants are between both SH modes. Cumulative solitons are qualitatively similar to solitons with just one SH mode, although both SH modes are part of the stationary solution. For competitive solitons we identified an upper boundary of the propagation constant for their existence. Close to this boundary the solitons are qualitatively similar to solitons in WGAs with saturable nonlinearity. Additionally, the existence region of competitive solitons shows a gap, resulting in soliton families with an energy threshold for soliton existence, which is not known in systems with just one SH mode. The stability of all identified solutions was studied as well. We found, that close to the existence boundary competitive solitons are unstable.

Experimentally, cumulative solitons could be excited and the participation of both SH modes in the soliton was confirmed [FS7,FS16]. For specific mismatches, spatial nonlinear beam-reshaping could be arrested completely due to the nonlinear competition [FS3,FS17]. This results in quasi-linear beam propagation even for high input power, and may be of significance also for applications trying to avoid nonlinear effects.

Chapter 5

Linearly coupled second harmonic modes

In the preceding chapter the influence of several SH modes on the nonlinear propagation of finite beams in WGAs was investigated. However, these investigations were limited to the existence, stability, and excitation of spatial solitons and related dynamic processes. The properties of these solitons and beams have been described only with rather general parameters such as power and width. The influence of specific parameters of the utilized SH modes was also only discussed in terms of how they influence soliton existence.

The topic of this chapter is the investigation of the impact of the specific properties of higher order SH modes on nonlinear beams, where the structure of solitons will be discussed in particular. A special emphasis is put on the topology of the SH parts of the beams, which are shown to possess novel features. Since the behavior of each SH component depends only on the properties of the guided mode it is propagating in, the analysis can be sufficiently carried out for only one SH mode. This allows for the precise determination of the effects induced by a particular higher order SH mode, without the added complexity of effects induced by mutual interactions of the FW with several SH modes. Experimentally, interaction with mainly one mode can be achieved, if the corresponding phase mismatch is much smaller than mismatches to other modes.

To focus the investigation on spatial effects, we restrict the theoretical description to the cw case. The dispersion coefficients not taken into account are similar for all modes, hence higher modes are not expected to result in different temporal effects. In this case, light propagation in a homogeneous lossless WGA is described by

$$\begin{aligned} i \frac{\partial}{\partial \bar{z}} A_n^{\text{FW}} + C^{\text{FW}} [A_{n+1}^{\text{FW}} + A_{n-1}^{\text{FW}}] &= -\gamma A_n^{\text{FW}*} A_n^{\text{SH}}, \\ i \frac{\partial}{\partial \bar{z}} A_n^{\text{SH}} + C^{\text{SH}} [A_{n+1}^{\text{SH}} + A_{n-1}^{\text{SH}}] - \Delta A_n^{\text{SH}} &= -\gamma [A_n^{\text{FW}}]^2. \end{aligned} \tag{5.1}$$

In this equation two parameters appear, which strongly depend on the SH mode prop-

erties, namely the nonlinear coefficient γ and the linear coupling strength C^{SH} . Differences in these coefficients for the various SH modes and their influence on the propagation will be the major subjects of our investigations. The mismatch Δ can be controlled by the experimental conditions, e.g. by the input wavelength.

The nonlinear coefficient γ can be changed significantly due to vastly different SH mode profiles and overlap integrals with the FW mode. However, the extreme case $\gamma = 0$, which can be achieved with modes of different symmetry (see Section 3.1.2), instantly leads to decoupling of the two equations of Eqs. (5.1) and hence to the well known linear propagation. On the other hand, a mere change of the magnitude of γ can be compensated by a change in the used power levels without the appearance of new effects. We will appreciate this fact by setting $\gamma = 1$ in the following. Thus, the only property of the SH modes with a nontrivial influence on the beam propagation is, as we will show, the linear coupling constant C^{SH} .

For a vanishing SH coupling ($C^{\text{SH}} = 0$) the spatial dynamics of the SH part of an evolving nonlinear beam is completely determined by the FW wave. SH photons can be generated from and converted to the FW wave and thus create the phase shifts necessary for spatial nonlinear effects. However, they cannot travel across the WGA. In this scenario the beam dynamics is very similar to that in a Kerr nonlinear medium, an analogy which finds its formal expression in the cascading approximation for large mismatches as derived in Section 4.2. Differences to Kerr media lie mainly in the changeable strength and sign of the nonlinearity due to the adjustable mismatch and the more involved form of the phaseshifts for smaller mismatches [64]. All experiments undertaken before this thesis were conducted in this limited case, since the linear coupling constant of the used SH00 can be considered zero for experimentally available sample lengths due to the strong mode confinement [105, 106]. However, as we showed experimentally in Section 3.2, the coupling constants for accessible higher order SH modes can be one or two orders of magnitude larger than for the SH00 mode. This results in the introduction of a kind of nonlocality in the nonlinear processes, since now SH photons generated in one waveguide can create nonlinear phaseshifts in different waveguides due to linear coupling independent from the FW. This system is now fundamentally different from the case with $C^{\text{SH}} = 0$ discussed above and it cannot be ascribed to a simple Kerr medium for any mismatch. For bulk media, where the SH wave diffracts, this nonlocality of the nonlinearity has been pointed out in various works [182, 199–201].

The aim of this chapter is to establish a basic understanding of the effects arising in nonlinear beam dynamics from the coupling of the SH modes. To this end in Section 5.1 the stationary solutions are derived and analyzed, first for the simplified system of Eqs. (5.1). After the explanation of the structure of the spatial solitons in this special case, we will show that the new characteristic effects remain also in

systems with more SH modes. The experimental proof for the predicted new effects of SH coupling is given in Section 5.2. To understand deviations between the predicted stationary solutions and the experimentally measured transient behavior, a thorough study of spatio-temporal pulse propagation in the WGA is carried out in Section 5.3.

5.1 Stationary solutions

Analog to the approach in Chapter 4, first discrete solitons are analyzed as fixed points of the system of Eqs. (5.1). The investigation will be restricted to solitons with real amplitudes, thus including only solutions with either 0 or π phase difference between fields in adjacent waveguides, which are called unstaggered or staggered. It is well established, that in a system with only one phasematching resonance solitons with unstaggered FW exist for propagation constants above the linear bands whereas solitons with staggered FW have propagation constants below the linear bands [22, 101, 105]. This was shown theoretically also for solutions with linearly coupled SH components. Nevertheless, the structure of the SH has never been studied comprehensively, although Refs. [22, 101, 202] found solutions with staggered FW and both unstaggered and staggered SH components. In the following the conditions for staggered or unstaggered soliton components are derived for the low power tails of the solitons, which can be treated analytically.

5.1.1 The structure of the soliton tails

To derive the condition for staggered or unstaggered soliton components first the solutions for linear waves propagating outside the linear bands are analyzed. The results can be applied to the low power soliton tails, which are only weakly nonlinear. A discrete linear plane wave of the WGA with constant amplitudes A_0^μ is propagating according to

$$\begin{aligned} A_n^{\text{FW}} &= A_0^{\text{FW}} \exp(i\kappa^{\text{FW}}n + ik^{\text{FW}}z), \\ A_n^{\text{SH}} &= A_0^{\text{SH}} \exp(i\kappa^{\text{SH}}n + ik^{\text{SH}}z). \end{aligned} \quad (5.2)$$

The transverse wavenumbers κ^μ and longitudinal wavenumbers k^μ are connected by the diffraction relations for FW and SH (see Eq. (3.10) in Section 3.2), which in the current case are

$$k^{\text{FW}} = 2C^{\text{FW}} \cos(\kappa^{\text{FW}}), \quad k^{\text{SH}} = 2C^{\text{SH}} \cos(\kappa^{\text{SH}}) - \Delta. \quad (5.3)$$

With Eq. (5.3) we can eliminate the transverse wavenumbers in Eq. (5.2). For propagation constants outside the bands, i.e. $|k^{\text{FW}}| \geq 2C^{\text{FW}}$ and $|k^{\text{SH}}| \geq 2C^{\text{SH}} - \Delta$ we find

an exponential decay for waves in the transversal direction. This reads as

$$A_n^{\text{FW}} = (\eta^{\text{FW}})^{-|n|} \text{ and } A_n^{\text{SH}} = (\eta^{\text{SH}})^{-|n|}, \quad (5.4)$$

with

$$\begin{aligned} \eta^{\text{FW}} &= \frac{k^{\text{FW}}}{2C^{\text{FW}}} \left(1 + \sqrt{1 - \left(\frac{2C^{\text{FW}}}{k^{\text{FW}}} \right)^2} \right), \\ \eta^{\text{SH}} &= \frac{k^{\text{SH}} + \Delta}{2C^{\text{SH}}} \left(1 + \sqrt{1 - \left(\frac{2C^{\text{SH}}}{k^{\text{SH}} + \Delta} \right)^2} \right). \end{aligned} \quad (5.5)$$

The amplitudes η^μ are positive for propagation constants above the linear bands and negative for propagation constants below the linear bands. Thus, for $k^{\text{FW}} \leq -2C^{\text{FW}}$ or $k^{\text{SH}} \leq -2C^{\text{SH}} - \Delta$ the respective wave amplitude switches its sign between adjacent waveguides, i.e. it is staggered.

To solve for stationary localized solutions of Eqs. (5.1) we use the exponential ansatz

$$\begin{aligned} A_n^{\text{FW}}(z) &= A_{0n}^{\text{FW}} \exp(ibz), \\ A_n^{\text{SH}}(z) &= A_{0n}^{\text{SH}} \exp(2ibz), \end{aligned} \quad (5.6)$$

with the propagation constant of the soliton b . Plugging this ansatz into Eqs. (5.1) results in the following system of equations

$$\begin{aligned} -bA_{0n}^{\text{FW}} + C^{\text{FW}} (A_{0n-1}^{\text{FW}} + A_{0n+1}^{\text{FW}}) + A_{0n}^{\text{FW}*} A_{0n}^{\text{SH}} &= 0, \\ -2bA_{0n}^{\text{SH}} + C^{\text{SH}} (A_{0n-1}^{\text{SH}} + A_{0n+1}^{\text{SH}}) + \Delta A_{0n}^{\text{SH}} + [A_{0n}^{\text{FW}}]^2 &= 0. \end{aligned} \quad (5.7)$$

In general, these equations have to be solved numerically, which we will do in the next section. However, the tails of the localized solutions can still be analyzed analytically. Here, for $|n| \gg 1$, $|A_{0n}^{\text{FW}}| \rightarrow 0$ and $|A_{0n}^{\text{SH}}| \rightarrow 0$ for localized states. Then the solution for the FW is approximately the same as for linear waves outside the linear bands,

$$A_{0n}^{\text{FW}} \approx (\eta^{\text{FW}})^{-|n|}. \quad (5.8)$$

However, for the SH equation of Eqs. (5.1) we cannot neglect the nonlinear term even in the small amplitude limit, since it represents an effective FW driving force. Hence, we have to perform an asymptotic analysis, thus determining the dominating contribution

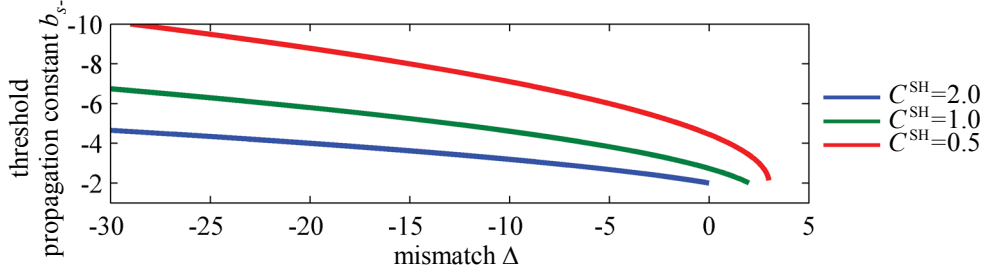


Figure 5.1: Threshold propagation constant b_{s-} in dependence on the mismatch Δ for $C^{\text{FW}} = 1$ and different C^{SH} .

to the SH amplitudes for large $|n|$. For the SH beam tails this is

$$\begin{aligned} A_{0n}^{\text{SH}} &\approx (\eta^{\text{SH}})^{-|n|} \quad \text{if } |\eta^{\text{SH}}| \leq (\eta^{\text{FW}})^2, \\ A_{0n}^{\text{SH}} &\approx (\eta^{\text{FW}})^{-2|n|} \quad \text{if } |\eta^{\text{SH}}| \geq (\eta^{\text{FW}})^2. \end{aligned} \quad (5.9)$$

In the first case the profile of the SH tails corresponds to the linear wave solution, whereas in the second case the SH is completely determined by the FW wave. We immediately see, that in this second situation the sign of the SH amplitudes is always positive, hence it cannot be staggered.

The transition between the two cases takes place when $|\eta^{\text{SH}}| = (\eta^{\text{FW}})^2$, which leads to a threshold propagation constant expressed as

$$b_{s\pm} = -\frac{C^{\text{FW}2}}{C^{\text{SH}}} \pm \sqrt{\frac{C^{\text{FW}4}}{C^{\text{SH}2}} + 2C^{\text{FW}2} - \Delta \frac{C^{\text{FW}2}}{C^{\text{SH}}}}. \quad (5.10)$$

For solitons with larger propagation constants than all linear states, the transition is rather trivial, since FW and SH are always unstaggered. However, $\eta^\mu < 0$ if the propagation constant is below the bands, $b < \min(-2C^{\text{FW}}, -C^{\text{SH}} - \Delta^{\text{SH}}/2)$. Hence, the FW tails are always staggered whereas the SH component can switch from unstaggered to staggered tails. For $b < b_{s-}$ and $b > b_{s+}$ the SH tails are staggered and unstaggered for $b_{s-} < b < b_{s+}$.

In Fig. 5.1 the threshold propagation constant b_{s-} for $C^{\text{FW}} = 1$ is plotted for various values of the SH coupling constant. The minimum threshold is determined by the FW band, since the solitons propagation constant has to be outside of the linear bands. In the shown examples $C^{\text{FW}} = 1$ leads to a minimum threshold of $b_{s-} = -2$. The magnitude of b_{s-} constantly grows with increasing magnitude of the mismatch. Also, a decrease of the SH coupling constant leads to an increase of the threshold propagation constant. Moreover we can deduce from Eq. (5.10) that $b_{s\pm}$ diverges for $C^{\text{SH}} \rightarrow 0$. Hence, the described effect was previously not experimentally observable due to the negligible coupling constant of the utilized SH00 mode.

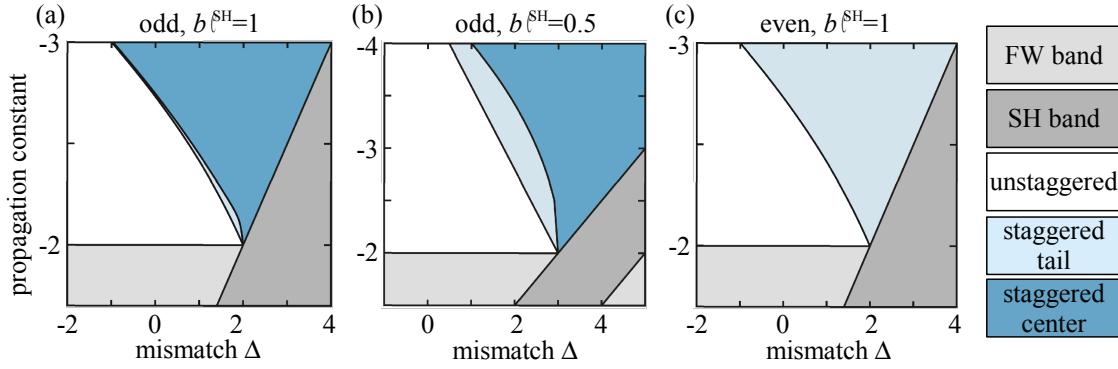


Figure 5.2: Parameter regions for different soliton topologies. In the linear FW (light gray) and SH (dark gray) bands, no solitons exist. We find solitons with unstaggered SH (white), staggered SH tails and unstaggered beam centers (light blue) and completely staggered SH (dark blue). Shown are odd solutions for (a) $C^{\text{SH}} = 1$ and (b) $C^{\text{SH}} = 0.5$ as well as (c) even solutions with $C^{\text{SH}} = 1$.

5.1.2 Parameter regions for soliton existence

In the last section we deduced an analytic expression for a transition of the soliton topology of spatial solitons with propagation constants below the linear bands of FW and SH. In this case the FW component is always staggered [101]. However, the analytic derivation of Eq. (5.10) was restricted to the tails of the localized solutions. Now the existence of the transition is shown also for the complete soliton by solving Eqs. (5.7) numerically [203]. Odd as well as even modes are calculated, which can be determined by choosing the appropriate initial conditions in the numerical iteration algorithm and an even or odd number of waveguides, respectively. For all numerical calculations $C^{\text{FW}} = 1$, which can always be achieved by normalization with the appropriate length L_0 . Additionally $\gamma = 1$ is assumed, which in the system of Eqs. (5.1) can be assured by an adequate transformation of the amplitudes, however, might be subject to changes in systems with more SH modes. To categorize the found solutions, the signs of the SH amplitudes in two neighboring waveguides are compared. Different signs imply that the SH part of the solution is staggered at the position of the two test waveguides. This topology test is applied at the edge of the calculation domain to monitor the soliton tails and at the maximum of the amplitude distribution.

The results of the numerical calculations and subsequent topology tests are summarized in Fig. 5.2. Here regions where no solitons exist due to the linear bands are marked in light (FW band) and dark (SH band) gray. All other colors are used to denote different soliton topologies. In white regions the SH is completely unstaggered, light blue marks staggered tails and dark blue a completely staggered SH wave. Fig. 5.2(a) shows odd solutions with $C^{\text{SH}} = 1$. Clearly solitons bifurcating from the FW bands undergo the transition with increasing magnitude of the propagation constant. The threshold for the soliton tails agrees with the analytical predictions of Eq. (5.10) and

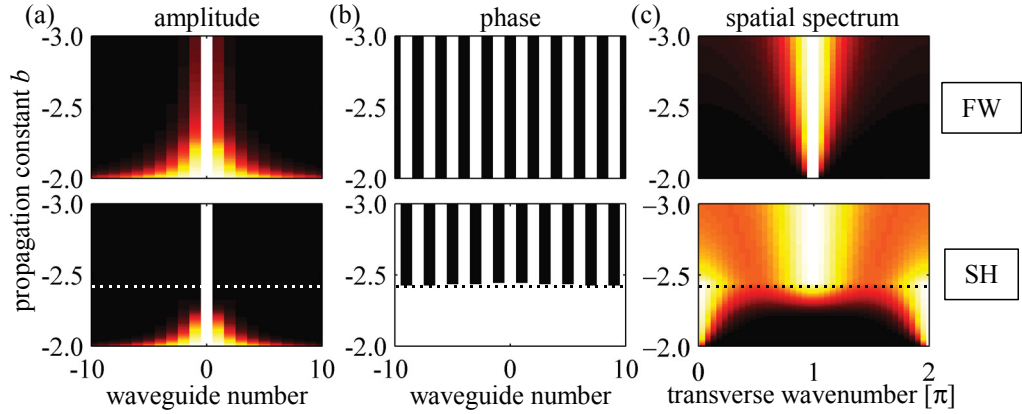


Figure 5.3: Odd soliton family for $\Delta = 1$. Quantities in the upper row belong to the FW and in the lower row to the SH component. (a) Absolute values of the mode amplitudes, (b) phases, where white corresponds to 0 and black to π , and (c) spatial spectral amplitudes. The dotted lines mark the analytical threshold propagation constant b_{s-} .

Fig. 5.1. The complete change of the SH topology happens for slightly larger propagation constants, which will be explained later when we analyze the intensity profiles of the soliton families. In Fig. 5.2(b) the odd solitons with $C^{\text{SH}} = 0.5$ are analyzed. As expected, for any mismatch the threshold propagation constant for the tails is larger than in the more strongly coupled case in Fig. 5.2(a). Additionally, the transition in the beam center takes place for larger propagation constant and hence the parameter domain of staggered tails and unstaggered beam center is much larger.

Remarkably, odd solutions bifurcating from the SH band always have a completely staggered SH component. This can be explained considering the power of the SH frequency component. For soliton families bifurcating from the SH band (in our examples for mismatches larger than the intersection point of FW and SH bands), the SH component always has a larger power than the FW. This is also known for quadratic spatial solitons in bulk media [204]. Hence, according to Eq. (5.9), the SH is always staggered.

Results for even solitons are plotted in Fig. 5.2(c). Here the transition in the tails exists as well and the transition propagation constant is the same as for the odd case. However, the transition in the center of the soliton is not taking place. This is a result of the symmetry constraints as will be shown later when we analyze the profiles of the solitons in more detail. We note that the even solutions are unstable [101] and decay into odd solitons when perturbed.

To better understand the mechanism of the topology transition, the intensity profiles of the solutions are evaluated. Fig. 5.3 shows the amplitudes of the odd soliton family with $\Delta = 1$. Other parameters are the same as in Fig. 5.2(a). In Fig. 5.3(a) the intensities of FW and SH components are shown. At low magnitudes of the propagation constants, close to the linear FW band, the stationary solutions are very wide and resemble linear waves. In this parameter regime also the power of the solution is small

and the fraction of SH energy in the soliton is very small. This is in accordance with earlier studies [101] and with the results for cumulative solitons from Section 4.2.2. For increasing propagation constants the solution is getting narrower and simultaneously total power, peak power, and SH power fraction are increasing. In Fig. 5.3(b) the phases of the two frequency components are shown. Since only real solutions are considered, the possible values of the phase are either 0 or π . The phase profile of the FW is staggered by default for all propagation constants below the linear bands. For the SH phase we confirm the results presented earlier. For smaller propagation constants the SH is unstaggered and abruptly switches to the staggered state at the transition threshold. The transition starts in the tails of the localized state and evolves towards the beam center.

The transformation of the SH is also manifested in the spatial spectra in Fig. 5.3(c). For wide solutions, the SH is generated according to the phasematching relation Eq. (3.13) for the transverse wavenumbers, which was proven experimentally in Section 3.2.1. This relation demands the transverse wavenumber of the SH to be twice the FW transverse wavenumber. We showed, that for wide staggered FW beams which have $\kappa^{\text{FW}} = \pi$ the corresponding SH has $\kappa^{\text{SH}} = 0$. This is fulfilled also for the wide stationary solutions. However, as the solitons become narrower the SH is driven at a decreasing number of waveguides. Hence, it becomes independent of the FW phase structure and propagates in its own preferred state. According to the linear solution Eq. (5.5), for propagation constants below the linear bands this is the staggered state. Thus, the onset of the SH phase transition can be explained by an increased localization of the stationary solution.

It has to be noted, that although other types of multicolor discrete spatial solitons with staggered phase profiles have been described [59,60,205], the existence of the phase transition is coupled to the parametric interaction between the different frequency components. Only this interaction enables one of the frequency components to be either determined by the other or to oscillate freely and hence allows switching between this two states. In the cited examples, the coupling between different frequencies was incoherent and consequently no transition was observed.

An even family of stationary solutions of Eq. (5.1) is plotted in Fig. 5.4. The dependence of the solution's width on the propagation constant is almost the same as for the odd solutions. The most prominent difference to odd solutions is the equality of the two central waveguides of each intensity distribution. As for the phases of the individual waveguides, we see that the FW is completely staggered as well. In the SH component the transition starts to emerge in the beam tails at the same threshold as in the odd case (not visible in the image due to the finite number of shown waveguides). However, the transition is not completed, even for large propagation constants. This results from the fact that due to the even symmetry of the solitons the localization is not

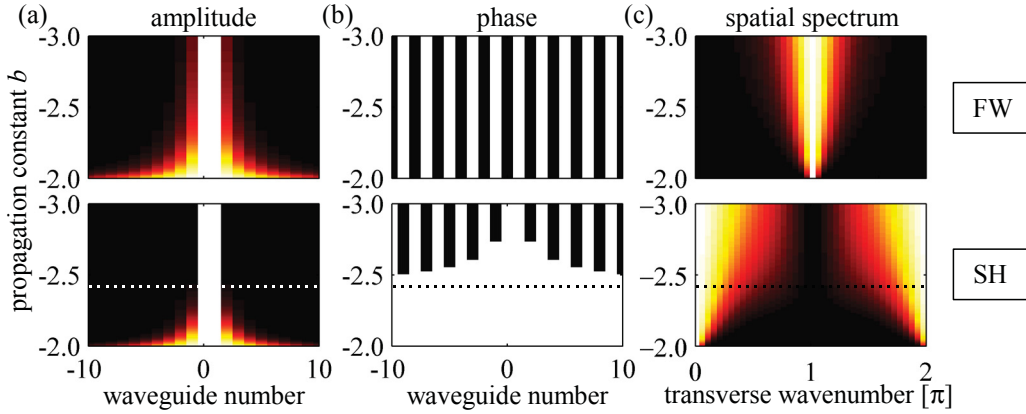


Figure 5.4: Even soliton family for $\Delta = 1$. Quantities in the upper row belong to the FW and in the lower row to the SH component. (a) Absolute values of the mode amplitudes, (b) phases, where white corresponds to 0 and black to π , and (c) spatial spectral amplitudes. The dotted lines mark the analytical threshold propagation constant.

as strong as for the odd solutions. Instead of being compressed to a width of almost only one waveguide, the minimum allowed width of the FW is two waveguides. Since the two central FW amplitudes have different phases, the corresponding SH amplitudes are forced to have the same phase. Hence they cannot be staggered. The incompleteness of the SH transition for even solitons can also be found in the spatial spectra. Here again the FW is centered at propagation constants of $\kappa^{\text{FW}} = \pi$. However, the maximum of the SH spatial spectrum is always at $\kappa^{\text{SH}} = 0$, even for a larger magnitude of the propagation constant where the SH tails are staggered. This results from the properties of the Fourier transformation.

In this section we confirmed the existence of a nontrivial topology transition of the SH component of discrete spatial solitons. By analyzing the soliton profiles the degree of localization of the soliton could be identified as a crucial property that determines in which state the soliton exists. In the next section the transition will be shown experimentally after we verified that it still exists in more realistic systems with several SH modes.

5.2 Soliton transition in multimode systems

One of the main results of the preceding section was, that the phase transition of the spatial solitons is directly linked to the linear coupling of the SH modes. It has already been pointed out, that for array periods which do not violate the approximation of weak coupling for the FW, the coupling coefficient of the SH00 mode is negligible. This entails, that the SH00 mode cannot be used experimentally to show the phase transition. Instead, higher order SH modes, having a larger mode area and hence an increased linear coupling coefficient, are utilized. As was described in Chapter 3, the

SH02 mode can have coupling constants which are in the same range or even larger than the ones for the FW00 mode for reasonably small array periods. Thus, among the easily accessible SH modes the SH02 mode is the best candidate to experimentally show the soliton phase transition. However, the SH02 and SH10 modes usually have similar wavenumbers, resulting in closely spaced phasematching wavelengths to the SH mode.

In Chapter 4 the existence of solitons in a system with two SH modes was extensively discussed. Especially the cumulative solitons, which exist for mismatches above or below both SH bands were found to be very similar to solitons in a system with only one SH mode. Hence, they are very likely to also undergo the topology transition if linearly coupled SH modes are involved. However, the SH02 and SH10 modes usually have different coupling constants, with the SH10 mode being coupled to a much lesser degree. In Section 5.1 it was concluded that the transition happens for smaller wavenumbers if the mismatch is small. Hence, it will be beneficial for its observation if the phasematching wavelength to the SH02 is closer to the excitation wavelength. For the necessary negative mismatches this requires the phasematching wavelength of the FW00 mode to the SH02 mode to be smaller than to the SH10 mode.

All formulated requirements for the experimental realization are fulfilled in the sample already used for the experiments in Chapter 4. Hence, we choose the same WGA with a period of $15\ \mu\text{m}$, resulting in coupling constants of $c^{\text{FW}} = 80\ \text{m}^{-1}$, $c^{\text{SH02}} = 63\ \text{m}^{-1}$, and $c^{\text{SH10}} = 16\ \text{m}^{-1}$, respectively. These are not ideal parameters, since the coupling of the SH02 mode is somewhat smaller than for the FW00. However, these numbers represent a reasonable trade-off. For arrays with larger coupling constants the SH bands will disturb each other, violating the condition of weak linear mode mixing, formulated in Section 2.2.2, and thus rendering the used coupled mode equations inappropriate to describe light propagation. Other available samples with different refractive index profiles and larger coupling constants show a reversed order of the two SH modes in demand, as in Section 3.2.3.

5.2.1 Stationary solutions

Before the measurement results concerning the soliton phase transition are described, we will again analyze the stationary solutions in a system which models the experimental conditions more precisely. As explained above, in the WGA we use in the measurements the SH10 mode is phasematched very close to the sought after SH02 mode. The phasematching wavelengths of all other SH modes with the SH02 are very far away, and hence other modes can be neglected. Thus, cw beam propagation is

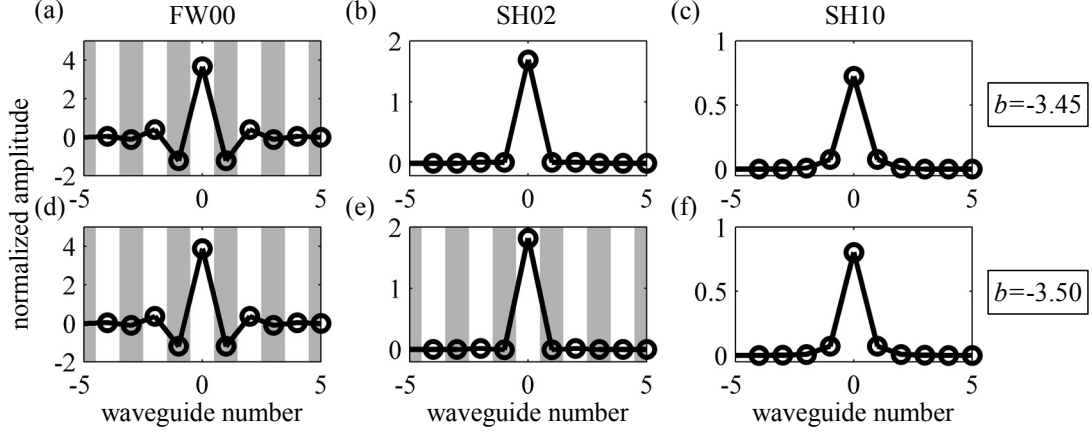


Figure 5.5: Soliton solutions with (a,d) FW, (b,e) SH02, and (c,f) SH10 components. For all plots, the mismatches are $\Delta^{\text{SH02}} = -1$ and $\Delta^{\text{SH10}} = -21$. The propagation constants are (a,b,c) $b = -3.45$ and (d,e,f) $b = -3.65$. The circles show the mode amplitudes and the shading denotes the phase where white corresponds to a phase of 0 and gray to a phase of π . The connecting lines are guides to the eye.

described by the system of equations already analyzed in Chapter 4, which reads

$$\begin{aligned}
 i \frac{\partial A_n^{\text{FW}}}{\partial z} + C^{\text{FW}}(A_{n+1}^{\text{FW}} + A_{n-1}^{\text{FW}}) + (\gamma^{\text{SH02}} A_n^{\text{SH02}} + \gamma^{\text{SH10}} A_n^{\text{SH10}}) (A_n^{\text{FW}})^* &= 0, \\
 i \frac{\partial A_n^{\text{SH02}}}{\partial z} + C^{\text{SH02}}(A_{n+1}^{\text{SH02}} + A_{n-1}^{\text{SH02}}) - \Delta^{\text{SH02}} A_n^{\text{SH02}} + \gamma^{\text{SH02}} (A_n^{\text{FW}})^2 &= 0, \\
 i \frac{\partial A_n^{\text{SH10}}}{\partial z} + C^{\text{SH10}}(A_{n+1}^{\text{SH10}} + A_{n-1}^{\text{SH10}}) - \Delta^{\text{SH10}} A_n^{\text{SH10}} + \gamma^{\text{SH10}} (A_n^{\text{FW}})^2 &= 0.
 \end{aligned} \tag{5.11}$$

Again, spatial solitons are stationary solutions of this system of equations which are found with the ansatz Eq. (4.15) with constant amplitude and a common propagation constant b for all frequency components. However, in contrast to the analysis in Chapter 4 now the normalized coefficients in Eqs. (5.11) are calculated from the coefficients of the experimental system. The normalized coupling coefficients are $C^{\text{FW}} = 1$, $C^{\text{SH02}} = 0.79$, and $C^{\text{SH10}} = 0.2$, respectively. In the same normalization the difference between the normalized mismatches is $\Delta^{\text{SH02}} - \Delta^{\text{SH10}} = 20$. The used normalized nonlinear coefficients are $\gamma^{\text{SH10}} = 1.51$ and $\gamma^{\text{SH02}} = 1$.

The stationary solutions of Eqs. (5.11) are again calculated numerically. Profiles of these spatial solitons with the aforementioned parameters for a mismatch of $\Delta^{\text{SH02}} = -1$ are plotted in Fig. 5.5. The threshold propagation constant for the SH02 mode with $C^{\text{SH02}} = 0.79$, calculated according to Eq. (5.10), is $b_{s-} = -3.47$. Since other potentially interacting SH modes do not change the asymptotic considerations leading to Eq. (5.10), the threshold should remain the same. This is confirmed by the numerical results. Figs. 5.5(a-c) show a soliton profile just below the threshold at $b = -3.45$. Here none of the SH components is staggered. In Figs. 5.5(d-f) the stationary solution at

$b = -3.65$ is depicted, where the SH02 mode is staggered. The threshold propagation constant is determined to $b_{s-} = -3.50 \pm 0.05$, thus corresponding to the analytic prediction. The SH10 amplitudes in Figs. 5.5(c,f) are unstaggered for both plotted propagation constants. With Eq. (5.10) the respective threshold propagation constant is calculated to be $b_{s-} = -16.5$.

In short, the phase transition of the SH components of spatial solitons also exists in systems with realistic parameters and two SH modes. However, the transition point strongly depends on the SH coupling constants and the mismatch, leading to different threshold propagation constants for the various SH components.

5.2.2 Experimental demonstration

For the experimental confirmation of the soliton phase transition its manifestation in the spatial spectrum is used. According to the results from Fig. 5.3 for odd solitons, upon the transition the intensity maximum moves from the center of the SH Brillouin zone to its edge. The spatial spectrum of the SH can be measured with the setup discussed in Section 2.4.2. To confirm the phase transition, solitons with different propagation constants and different widths have to be excited and a change in the spatial spectrum has to be recorded. This cannot be achieved directly, since the propagation constant of a soliton cannot be set externally. Additionally, the experiments are again carried out with FW only excitation and a fixed beam width. Although spatial solitary waves in lithium niobate WGAs have been successfully excited in spite of these experimental shortcomings [105], their width always was very close to the width of the wide incident beam. A number of studies investigating the excitation problem of quadratic spatial solitons in bulk crystals has already been undertaken [83, 193, 206–208]. They show that increasing the input power increases the parameter range of solitons accessible with a fixed input beam. Hence, also solitons with profiles very different from the input beam can be excited, although the fraction of energy transferred to that soliton may be very small. This effect is used here for the controlled excitation of states with staggered SH. The absolute power $P = \sum_n |A_n^{\text{FW}}|^2 + |A_n^{\text{SH02}}|^2 + |A_n^{\text{SH10}}|^2$ of the stationary solutions of Eqs. (5.11) for realistic parameters is plotted in Fig. 5.6 in dependence on the propagation constant for different mismatches. The threshold for the transition is marked by the crosses. For increasing magnitude of the propagation constant, the necessary power is always increasing. Hence, for small powers the solutions with staggered SH can never be excited, whereas for increasing power it should be possible to transfer energy from the exciting beam to the sought after solitary wave.

The necessary power levels, which are in the range of 10 kW, are generated by short optical pulses of 5.3 ps FWHM length. Due to the high peak powers and consequently large amounts of SH radiation, temporal effects have to be taken into account when

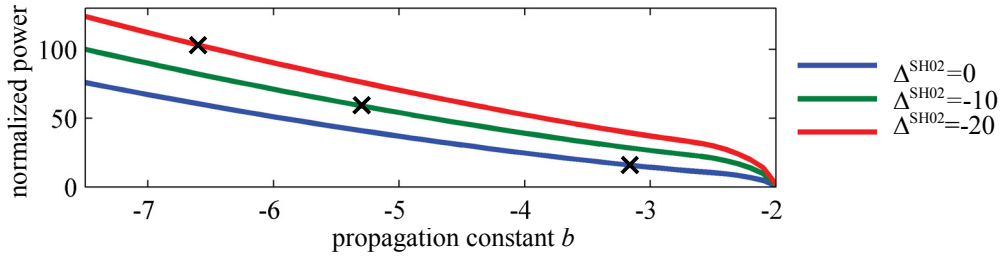


Figure 5.6: Absolute power of stationary solutions for real parameters in dependence on the propagation constant for different mismatches Δ^{SH02} . The crosses mark the analytically calculated threshold propagation constants.

the experimental results are analyzed. This is in contrast to Section 4.3.2, where the weaker SH was assumed to be trapped under the FW pulse. Complete temporal trapping of the SH cannot readily be postulated here. Furthermore, spatio-temporal solitons, which may show the same spatial SH topology transition as the spatial solitons, do not exist in the used samples [95]. This is due to the large difference in the GVD of FW and SH. Hence, a complicated temporal dynamics is expected to take place during propagation, which cannot be directly resolved with the existing measurement equipment. To interpret the measurement results and to additionally study the pulse dynamics inside the sample leading to the measured output, simulations which model the experiment as exactly as possible are carried out.

The experiments now aim to confirm the existence of the phase transition in a dynamic system, where stationary states are not necessarily excited. First, we will discuss the results of temporally integrated spatial measurements, double-checked by simulations. The spatio-temporal dynamics of the propagating pulses is revealed in the following section.

In all experiments described here, the FW input beam has an FWHM width of

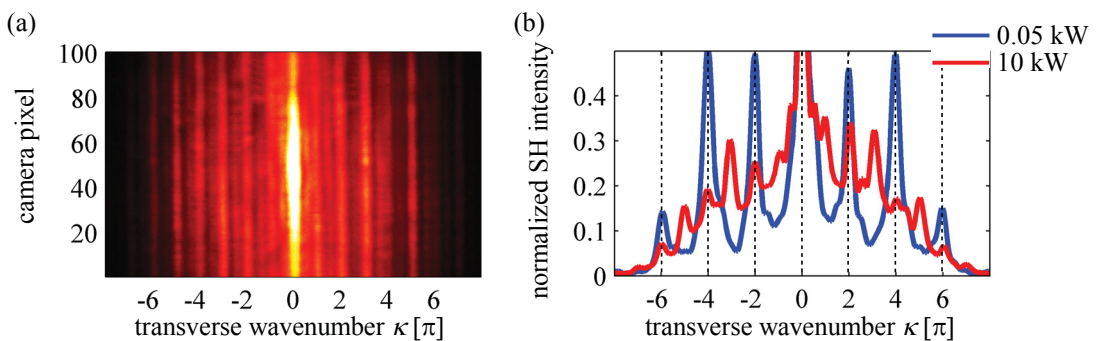


Figure 5.7: (a) Typical result of time integrated measurements in the spatial SH Fourier domain. The used input wavelength is $\lambda^{\text{FW}} = 1499 \text{ nm}$ with an input peak power of 10 kW. (b) Vertically integrated SH spatial spectra for the same wavelength as in (a) for different levels of FW peak power. The high power curve corresponds to the measurement in (a).

60 μm , corresponding to 4 array periods, and is tilted to achieve a phase difference $\kappa^{\text{FW}} = \pi$ between adjacent waveguides. The input beam is adjusted to have its maximum exactly at the location of a waveguide, thus exciting a wavepacket with odd symmetry. The SH output of the WGA is filtered spatially. To this end in the image plane of the coupling objective an aperture is included in the setup which blocks all but the 5 central waveguides. This is necessary to reduce the influence of SH modes from non-degenerate nonlinear interactions on the measurement results. A typical measurement result in the SH Fourier plane is depicted in Fig. 5.7(a). Since the measuring CCD camera uses exposure times in the range of milliseconds, the measurement is averaged over the temporal envelope of several pulses. The image in Fig. 5.7(a) is measured for an input FW peak power of 10 kW at a wavelength of 1499 nm. The periodic nature of the spatial spectrum is clearly visible in the horizontal direction. To accommodate for vertical inhomogeneities, the 2D data is integrated vertically. The resulting spatial spectra for 10 kW and 0.05 kW FW input peak power are shown in Fig. 5.7(b). For the lower FW power the SH is completely localized at wavenumbers of $\kappa^{\text{SH}} = 2m\pi, m \in \mathbb{N}$, corresponding to the centers of the different Brillouin zones and hence to unstaggered SH. Here the transverse wavenumber κ^{SH} is used to describe the spatial spectrum of both modes simultaneously, since we cannot distinguish between them. Measurements at low power are also used to calibrate the wavenumber axis in all experimental images. For the larger FW input power of 10 kW, additional SH maxima at $\kappa^{\text{SH}} = (2m + 1)\pi, m \in \mathbb{N}$ are visible. They clearly indicate, that staggered SH is indeed generated for these experimental conditions. A noticeable feature of all measured Fourier spectra is the very large maximum at $\kappa^{\text{SH}} = 0$. The intensity there is inflated, since all SH radiation which is produced in the sample but not in a guided mode of the array is generated at very small transverse wavenumbers. This may include SH spawned from non-guided FW waves, from the sample edges, and from interactions with very high order non-guided SH modes. To avoid this excessively large peak in the following only the SH spatial spectrum with $2\pi \leq \kappa^{\text{SH}} \leq 4\pi$ will be evaluated. However, the plot labels will still refer to the first Brillouin zone, which is justified because of the periodicity. Additionally we note, that the SH intensity is not dropping to zero between the peaks. This is due to the limited spectral resolution induced by the spatial filtering. In the following analysis the minimum low power SH intensity in the investigated part of the spatial spectrum is always subtracted.

The upper row of Fig. 5.8 shows experimental results for a number of mismatches. The stationary solutions corresponding to these mismatches show the phase transition in the SH02 wave. In each experiment the FW input peak power is increased from about 500 W to 8.5 kW. Due to the limited dynamic range of the automatic power control in our setup, the low power boundary cannot be set to smaller powers. In Fig. 5.8 each measurement of the SH intensity (corresponding to one FW peak power) has

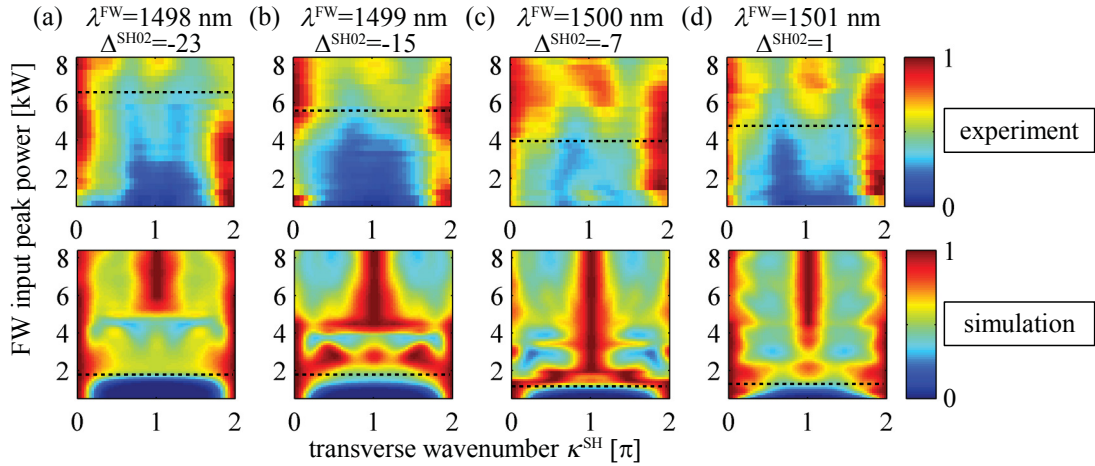


Figure 5.8: Spatial spectrum of the SH component in dependence on the FW input peak power for an input FW wavelength λ^{FW} (input mismatch Δ^{SH02}) of (a) 1498 nm (-23), (b) 1499 nm (-15), (c) 1500 nm (-7), and (d) 1501 nm (1). The upper row shows experimental results, which are compared to the corresponding simulations in the lower row. The dotted lines mark the approximate transition powers.

been normalized to the SH peak intensity for that input power in the shown interval of the spatial spectrum. In all measurements we find that at low powers the SH intensity is localized at $\kappa^{\text{SH}} = 0, 2\pi$. With increasing power, an additional maximum appears at $\kappa^{\text{SH}} = \pi$, corresponding to staggered SH. Hence, these experimental results confirm the existence of a partial transition of the SH from unstaggered to staggered for odd beams. The threshold power, for which the staggered SH intensity reaches approximately one half of the maximum SH intensity in this measurement, is marked by the dotted lines. The threshold power is decreasing for decreasing magnitude of the negative mismatch, which is due to the larger nonlinearity closer to phasematching. This is also in agreement with the stationary solutions, where we found a decrease in the threshold propagation constant (roughly proportional to the power, see Fig. 5.6) for decreasing magnitude of the mismatch. The threshold slightly increases for $\lambda^{\text{FW}} = 1501$ nm. An increase of the threshold power is expected for wavelengths above the phasematching wavelength 1501.5 nm. Here stationary states have a higher SH content. Hence, the excitation efficiency is lower with FW only excitation and higher powers are necessary to generate states with staggered SH. Due to inhomogeneities of the sample and the spectral width of the used pulses the excitation for $\lambda^{\text{FW}} = 1501$ nm is partially in this regime.

To further corroborate these observations, we conduct simulations of the experiments by integrating the complete set of equations Eqs. (2.58) with the parameters of Tab. 5.1 using the split-step algorithm [209]. In the simulations the sample inhomogeneities are taken into account as linear detuning $\Delta_{\text{lin}}^{\text{SH02}}(z)$ and $\Delta_{\text{lin}}^{\text{SH10}}(z)$. Simulation results are shown in the lower row of Fig. 5.8, where the sum of the intensities of both

description	real values			normalized values				
		FW00	SH10	SH02		FW00	SH10	SH02
GVD	D^μ [ps ² m ⁻¹]	0.14	0.53	0.68	\bar{D}^μ	0.0061	0.024	0.030
group velocity	$\frac{1}{v_g^\mu}$ [ns m ⁻¹]	7.34	7.70	7.70	δ^ν	-	0.85	0.85
nonlinearity	χ_{eff}^ν [as m ⁻¹]	-	8.3	5.5	γ^ν	-	1.50	1.0
damping	α^μ [m ⁻¹]	4.7	9.2	9.2	$\bar{\alpha}^\mu$	0.029	0.058	0.058
coupling	c^μ [m ⁻¹]	80	62	16	C^μ	1	0.79	0.2

Table 5.1: Parameters of the sample. The normalized values have been obtained with a normalization length of $L_0 = 1/c^{\text{FW}} = 1.25$ cm and a normalization time of $T_0 = 5.3$ ps, which is the input pulse duration.

SH components is plotted. The simulations qualitatively agree with the measurement results, also showing the transition for all mismatches. However, the threshold power, above which a significant fraction of the SH is staggered, differs considerably between measurements and simulations. In the experiments this threshold is much larger than in the simulations. The dependence of the transition power on the mismatch is similar to the measurements, a decrease with increasing mismatch and a slight increase for $\Delta^{\text{SH02}} = 1$. However, in the measurements we also find weak staggered SH for input peak powers much below the threshold power. This is visible in Figs. 5.8(a) and (c). Hence, in accordance with the simulations, staggered SH may be generated for much lower powers.

To investigate the trigger mechanism for the appearance of staggered SH in the dynamic experimental situation, we analyze the spatial output of experiment and simulation in Fig. 5.9(a) and (b). In the images the FW spatial output intensity is plotted in dependence on the input peak power for $\lambda^{\text{FW}} = 1500$ nm. We observe focusing of the beam at a power of around 1 kW in accordance with earlier measurements from Section 4.3.2. This focusing corresponds to the excitation of spatial solitons with un-staggered SH components, where the output beam width equals the input beam width. In the experiments, further increase of the power broadens the beam, whereas it is focused to almost only one waveguide in the simulation. In the simulation, this strong focusing triggers the excitation of states with staggered SH at powers between 1.5 and 2 kW, seen in Fig. 5.8(c). For higher powers (not shown in Fig. 5.9(a) and (b)), the output FW beam width nearly stays the same in experiment and simulation. Here the propagating pulse is focused inside the sample and broadens upon further propagation. It can be concluded from the simulations, that similar to the stationary solutions the focusing of the beam to a small number of waveguides is necessary to generate staggered SH. Hence, we assume that staggered SH is generated in the experiment as well for lower powers, but cannot be detected with the time integrated measurement method due to a low generation efficiency and a large background signal. By analyzing

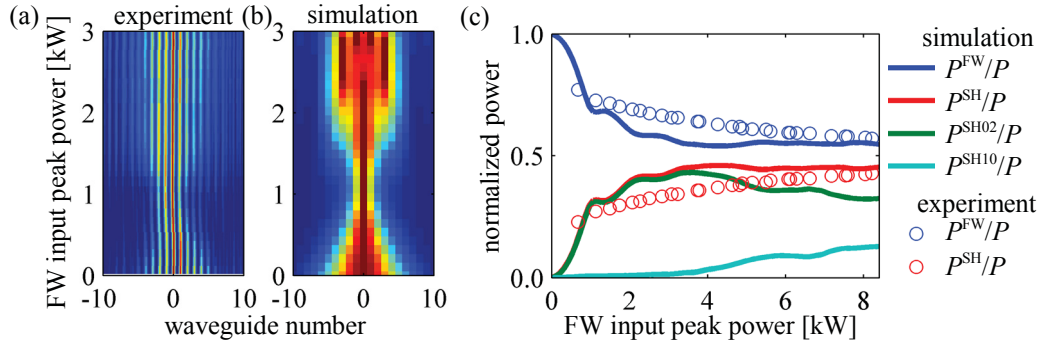


Figure 5.9: (a) Measurement of the spatial FW intensity distribution at the array output in dependence on the FW input peak power and (b) corresponding simulation. The input FW wavelength is $\lambda^{\text{FW}} = 1500$ nm, meaning the mismatch is $\Delta^{\text{SH02}} = 7$. (c) Comparison of the measured and calculated powers of the different components for the same parameters as in (a) and (b). The powers are normalized to the overall power for each input peak power.

the pulse dynamics in the next section, the generation of staggered SH will be further clarified. Spectrally resolved measurements will also clear the discrepancies between simulation and experiment.

An additional problem of the experiments results from not distinguishing between the intensities belonging to different participating SH modes. Although this would be possible with specially designed optical elements [210], this method is not suitable for implementation in the used setup. Fig. 5.9(c) shows the simulated and measured powers at the array output as fractions of the absolute power for $\lambda^{\text{FW}} = 1500$ nm. Here, the absolute power is $P = \sum_{\mu} \sum_n |A_n^{\mu}|^2$ with μ again running over all modes at all frequencies. The partial powers then are $P^{\text{FW}} = \sum_n |A_n^{\text{FW}}|^2$, $P^{\text{SH}} = \sum_n |A_n^{\text{SH02}}|^2 + |A_n^{\text{SH10}}|^2$, and $P^{\nu} = \sum_n |A_n^{\nu}|^2$ for the SH mode ν . In the experiments we can only determine P^{FW} and P^{SH} . A good agreement between simulated and measured powers is found, with almost half of the power transferred to the SH frequency at the highest input power. The normalized FW (SH) power in the experiment is always a bit larger (smaller) than in the simulation, which can be attributed to the excitation of the FW01 mode. The FW01 mode does not strongly participate in nonlinear interactions at this wavelength, but is measured as FW power. The good agreement leads to the conclusion, that in the experiments the maximum power in the SH10 mode is around 30% of the SH02 power. For SH generated at $\kappa^{\text{SH}} = \pi$ the simulated SH10 component is even weaker.

A striking feature of the soliton phase transition is the vanishing of staggered SH intensity in the spatial spectrum for even solutions. To also prove this feature experimentally, the SH spatial spectrum is recorded for odd and even FW excitation for an input peak power of 10 kW. The result for $\lambda^{\text{FW}} = 1500$ nm is compared to corresponding simulations in Fig. 5.10(a). Clearly, the SH spatial spectrum is affected by the change of the excitation. For odd excitation, staggered SH is generated, whereas the

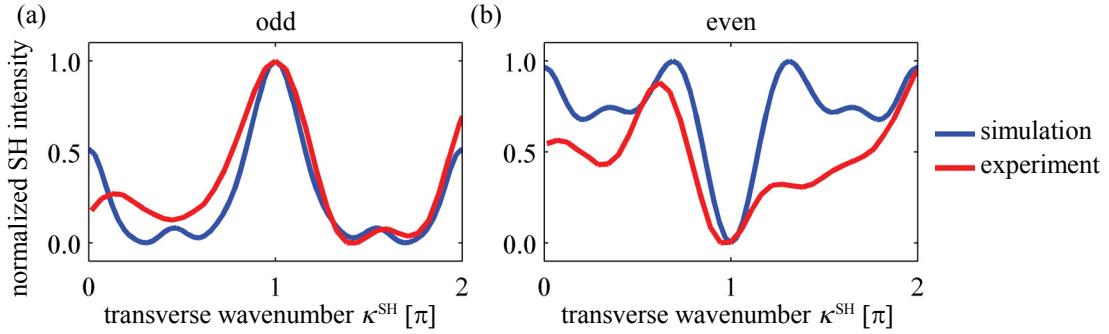


Figure 5.10: Spatial SH spectra for (a) odd and (b) even FW excitation. The input FW wavelength is $\lambda^{\text{FW}} = 1500$ nm, the mismatch $\Delta^{\text{SH02}} = -7$, and the FW input peak power is 10 kW.

intensity at $\kappa^{\text{SH}} = \pi$ is minimal in the even case. The experimental verification of the difference between even and odd beams is surprising, since even beams are known to be unstable and tend to decay into odd beams [101, 105]. Nevertheless, the instability develops slow enough that some characteristic features of even beam propagation survive and are measurable.

Summarizing the experimental results described until now, the power dependent topology transition of the SH wave in nonlinear parametric beam propagation was shown with time integrated measurements. A mismatch dependent power threshold for the generation of staggered SH was identified. However, in the experiments most staggered SH was generated for powers where the beam was shown to be relatively broad. Hence, stably propagating spatial solitons with staggered SH have not been shown, even not in the sense of Ref. [197], where the beam profile of pulsed beams is still determined by the underlying spatial solitary wave. We conclude, that the SH topology transition is not restricted to solitons, but a generic feature of parametric beam propagation in WGAs. Additionally, the dependence of the phase transition on the beam symmetry was experimentally verified.

5.3 Spatio-temporal dynamics

After investigating the temporally integrated output of the WGA for various mismatches and FW input peak powers we concluded, that the predicted transition of the SH wave from staggered to unstaggered is a generic property of parametric nonlinear beam propagation. However, although staggered SH was detected only for beams undergoing focusing, the generation mechanism could not be completely uncovered. To this end one needs to directly study the spatio-temporal dynamics of the propagating pulses. A number of standard techniques to experimentally characterize short optical pulses exist [211]. However, these methods are not very suitable to characterize the

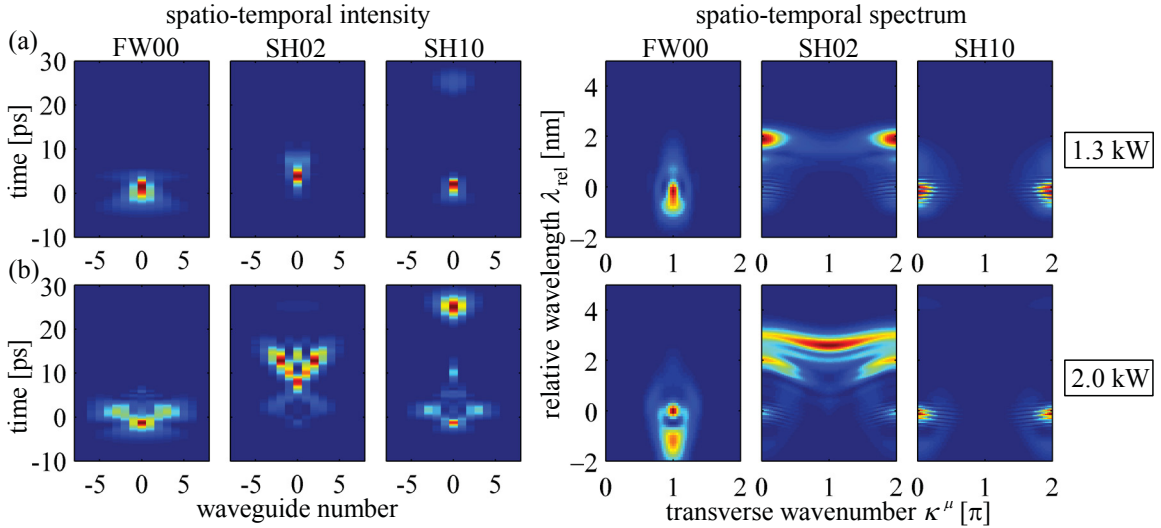


Figure 5.11: Spatio-temporal (left) and spectral (right) representations of simulated FW, SH02, and SH10 output intensities for (a) 1.3 kW and (b) 2.0 kW FW input peak power. The wavelengths are given as the corresponding FW wavelengths relative to the central input wavelength of 1499 nm.

output pulses of the experimentally investigated WGAs, since every waveguide has to be measured separately for each investigated power level. A spatially resolved cross-correlation technique [212] would be feasible, however, it relies on a pump pulse much shorter than is available with the laser system used here. Consequently we will follow a different approach. First, the pulse propagation in the array will be analyzed using simulation results which show the pulses in the spatio-temporal as well as in the spectral domains. This analysis is used to identify distinct features indicating the generation of staggered SH, which we measure in the spectrally resolved spatial spectrum. In turn, these measurements are utilized to verify the simulations.

5.3.1 Simulation of pulse dynamics

In the last section results of time integrated measurements have been presented for a number of different phase mismatches. Since these results did not show qualitative differences, it is sufficient to carry out the detailed analysis of the spatio-temporal dynamics only for one wavelength or mismatch. The wavelength of interest is determined by experimental constraints. The results at wavelengths close to the phasematching wavelength between FW00 and SH02, $\lambda^{FW} = 1501.5$ nm, are strongly influenced by sample inhomogeneities. Hence, they may not be very representative. At $\lambda^{FW} = 1498$ nm the experiments are complicated by non-degenerated phasematching to the SH11 mode, which is not simulated. A suitable wavelength is $\lambda^{FW} = 1499$ nm, corresponding to a normalized mismatch of $\Delta^{SH02} = -15$, which is further used.

First, we simulate and analyze the power dependence of the output of the WGA af-

ter 71 mm of propagation. The same simulation results presented already in Fig. 5.8(b) are used, albeit not integrated over time. Results for input peak powers of 1.3 kW and 2 kW are shown in Fig. 5.11, below and just above the threshold power defined in Fig. 5.8(b). 1.3 kW also corresponds to the power where the time integrated beam is focused to its smallest width. For each power (one row of Fig. 5.11), the spatio-temporal intensities as well as the intensity in dependence on wavelength and transverse wavenumber for all three frequency components are plotted. The wavelengths in this and the following figures are labeled with the wavelength relative to the FW input wavelength, which is $\lambda_{\text{rel}} = \lambda^{\text{FW}} - \lambda_{\text{in}}^{\text{FW}}$ for the FW and $\lambda_{\text{rel}} = 2\lambda^{\text{SH}} - \lambda_{\text{in}}^{\text{FW}}$ for the SH. Hence, equal relative wavelengths of FW and SH figures correspond to each other. The phasematching wavelengths are 1501.5 nm to the unstaggered SH02 and 1503.8 nm to the unstaggered SH10 wave, corresponding to relative wavelengths λ_{rel} of 2.5 nm and 4.8 nm, respectively.

For 1.3 kW in Fig. 5.11(a), the pulses are compressed spatially to almost one waveguide. Front and tail of the FW pulse are still broader, since the lower power in this regions is not enough to generate the necessary phase shifts for spatial focusing [213]. We note, that this effect is used in WGAs with Kerr-nonlinearity to excite X-shaped waves [214–216]. Both SH components show the same features. They consist of a trailing pulse, which was already generated at the input, and SH trapped by the FW pulse [194–196, 217, 218], although the free radiation is very weak for the SH02. The trapped SH photons are constantly generated by SHG and subsequently reabsorbed via DFG and by this cascading are responsible for the nonlinear phase shifts. The FW spectrum is broadened due to effective self-phase modulation. Since the cascading phase shifts depend on the wavelength, the spectral broadening is not symmetric as in a process driven by Kerr-nonlinearity [219]. The FW shifted to longer wavelengths comes very close to the phasematching wavelength with the SH02 wave and hence is efficiently transferred to the SH frequency. As a consequence, for powers above the power of strongest focusing SHG strongly increases, as is also documented in Fig. 5.9(b) for a slightly smaller mismatch than considered here. The SH is not generated exactly at $\lambda_{\text{rel}} = 2.5$ nm, which would correspond to the phasematching wavelength, but a bit below. This originates from the sample inhomogeneity, since at the end of the sample the local phasematching wavelength is lower. Although the beams in the spatial domain are strongly localized and thus in the spatial-spectral domain are rather broad, the maximum of the SH02 component is still unstaggered. The SH10 spectrum is concentrated around the excitation wavelength, here a beating between the components traveling with the FW pulse and the ones propagating freely behind is observed.

For an input peak power of 2 kW in Fig. 5.11(b) the spatial representations are already broadened with respect to Fig. 5.11(a). The FW pulse maintains its X-shape, but with more pronounced wings. The SH10 wave mainly travels with the FW pulse. In

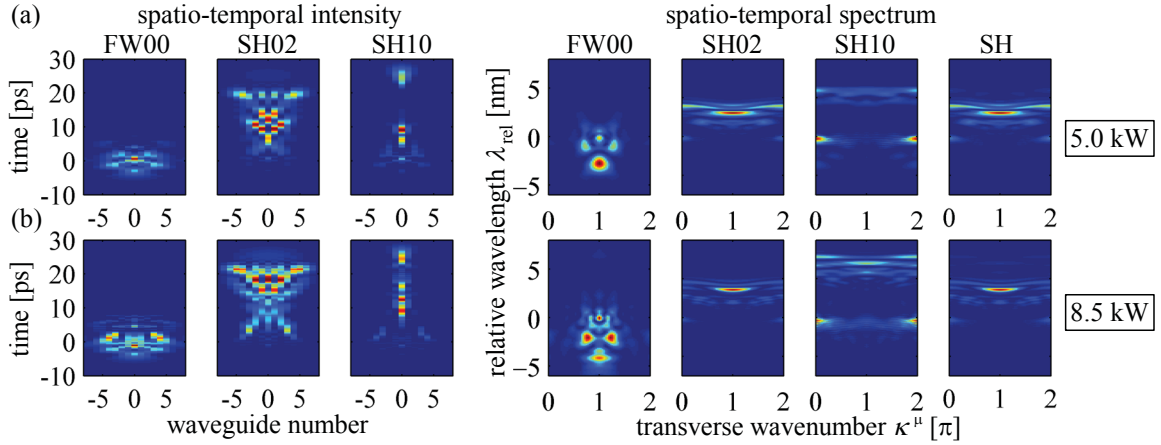


Figure 5.12: Spatio-temporal (left) and spectral (right) representations of simulated FW, SH02, and SH10 output intensities for (a) 5.0 kW and (b) 8.5 kW FW input peak power. The wavelengths are given as the corresponding FW wavelengths relative to the central input wavelength of 1499 nm. The right column shows the sum of the spectral SH02 and SH10 intensities.

contrast, the SH02 component radiates away from the FW pulse and diffracts. This is a consequence of the efficient SHG at the phasematching wavelength. The large amount of generated SH cannot be retained under the FW pulse since it travels with the same phase velocity and thus is not subject to cascading. Hence, it is radiating away and consequently diffracts due to linear coupling. Now staggered SH02 at $\kappa^{\text{SH02}} = \pi$ is generated, even though this takes place in the SH radiation cone and is not part of a stationary state. This generation is restricted to approximately the phasematching wavelength to the SH02 wave, which however is now shifted to higher wavelengths with respect to Fig. 5.11(a). This has two reasons. First, the SH presumably is now generated at a different place in the sample, where the local phasematching wavelength is higher than at the end. Secondly, due to phaseshifts generated by the FW00-SH10 phasematching resonance, the FW00 travels effectively with a different phase velocity. Thus, the phasematching wavelength to the SH02 is nonlinearly detuned to larger values [77]. The SH10 wave does not show staggered waves due to its smaller coupling constant, larger mismatch and hence larger threshold power.

For higher input peak powers the output pulses, shown in Fig. 5.12, are more complex. However, we see that for both powers, 5 kW in Fig. 5.12(a) and 8.5 kW in Fig. 5.12(b), the SH waves do not propagate locked to the FW. Instead, both SH components radiate away, forming cones of different width correlating to the coupling strengths. Consequently, now also the SH10 has significant components generated close to the relative low power phasematching wavelength of $\lambda_{rel} = 4.8$ nm. The SH02 wave is mostly generated in the staggered state, whereas the SH10 component shows staggered portions only for 8.5 kW. However, as evident in the images combining both SH components, the SH02 is still dominant. This is a consequence of the generation

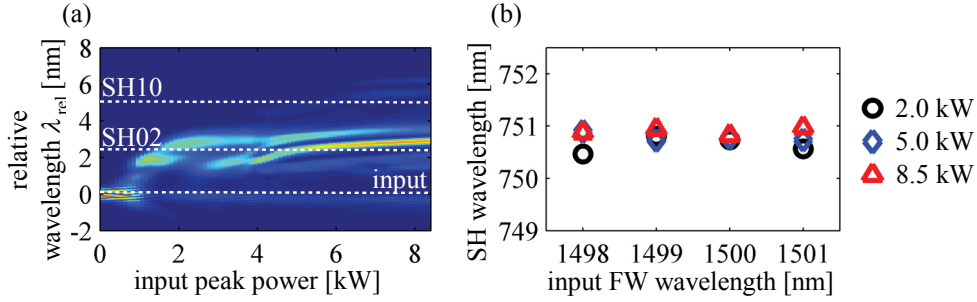


Figure 5.13: (a) Simulated SH output spectrum in dependence on the input power for $\lambda^{\text{FW}} = 1499$ nm. The dotted lines mark the input and phasematching wavelengths relative to the FW input wavelength as indicated by the labels. (b) Wavelength of the maximum SH02 intensity for $\kappa^{\text{SH02}} = \pi$ in dependence on input FW wavelength and power.

mechanism, since only FW which is shifted across the SH02 phasematching resonance without being transformed can contribute to the phasematched SH10. Hence, for all simulated powers the main contribution to the staggered SH comes from the SH02 wave.

The largest amount of SH and especially the staggered SH components are generated at the phasematching wavelengths. To further underline this, the SH output spectrum corresponding to the simulated pulse outputs explained above is depicted in Fig. 5.13(a). Above a power of ≈ 1.0 kW, shortly before the strongest focusing appears, the SH indeed is generated near the phasematching wavelengths. Differences are due to sample inhomogeneities and power dependent detuning [77]. The same effects as described for 1499 nm are found for other FW input wavelengths. In Fig. 5.13(b), the wavelengths of the maximum SH02 intensity at a transverse wavenumber of $\kappa^{\text{SH02}} = \pi$ are compared for different input wavelengths and powers. The differences in the generation wavelengths are very small and again originate mostly from inhomogeneities and nonlinear detuning.

To further strengthen the given interpretations, the pulse dynamics along the propagation inside the sample is investigated. To be consistent with the case discussed above, the FW input wavelength is again 1499 nm with all other parameters staying the same as well. The input power simulated here is 2 kW. For this power Fig. 5.11(b) already shows the generation of staggered SH, yet the pulse shapes are still easy to interpret. The intensities in different stages of the propagation are shown in Fig. 5.14. Here the SH10 component is omitted, since it does not contribute to the generation of staggered SH waves. Initially, the FW and SH pulse are spatially narrowing. After 20 mm of propagation, the SH pulse not retained under the FW pulse is visible, trailing the FW radiation by ≈ 7 ps. After 38 mm, the pulses are strongly focused, especially the SH wave is localized in only 1 waveguide. This leads to broad spatial spectra of all components. Also, the effective self-phase modulation of the FW already

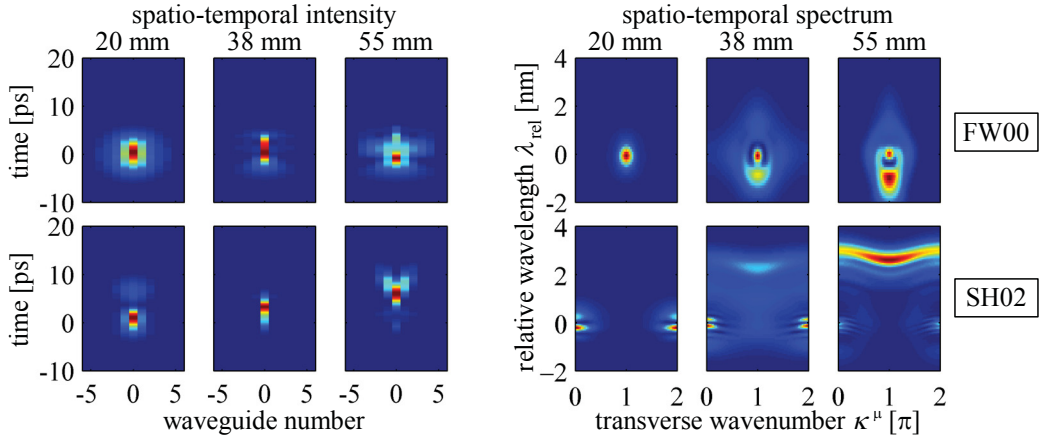


Figure 5.14: Spatio-temporal (left) and spectral (right) representations of simulated FW (upper row) and SH02 (lower row) intensities for different propagation lengths. The wavelengths are given relative to the central input wavelength of 1499 nm for the FW and 749.5 nm for the SH, respectively. The FW input peak power is 2 kW.

broadened the spectra, leading to efficient SHG at the phasematching wavelength of $\lambda_{\text{rel}} = 2.5$ nm. Notably, for the SHG generated at the phasematching wavelength a maximum at $\kappa^{\text{SH02}} = \pi$ can be recognized, signaling SHG primarily of staggered waves. Indeed, locally the pulses are similar to the stationary solutions calculated in Section 5.2.1 in terms of the necessary localization and power levels. Finally, after 55 mm of propagation the FW is broadened again in the front and tail, whereas the generated SH is radiating away from the FW pulse. The SH spatial spectrum clearly shows a maximum for staggered SH. This maximum is rather broad, since due to the strong spatial localization of the FW wave SH can be generated for a large range of transverse wavenumbers. However, we note that the SH is not generated at the same wavelength across the whole Brillouin zone. This can be explained with results from Chapter 3, where we found that in order to fulfill the phasematching condition for various FW transverse wavenumbers, the SH is generated at different points of its dispersion relation and hence at different wavelengths. In the case discussed here, the FW spectrum is broad enough to enable simultaneous phasematching for different transverse wavenumbers. The SH is generated at an isoline of the SH dispersion relation. In a weakly coupled WGA, these isolines of constant longitudinal wavenumber follow a cosine-shape like the diffraction relation. States which have their energy distributed along the isolines of the dispersion relation have been described as SH X-waves [220–222]. In Ref. [220] also the SH radiation cone, which is supported by the FW pulse at one end, is predicted, exactly as we find it in our simulations.

To conclude this section, we have shown that in our system staggered SH is not generated in spatial solitons. Instead, a highly dynamical process takes place which includes spatial and spectral reshaping of the input beam. The staggered SH is only generated at wavelengths close to the phasematching wavelength. This peculiar feature

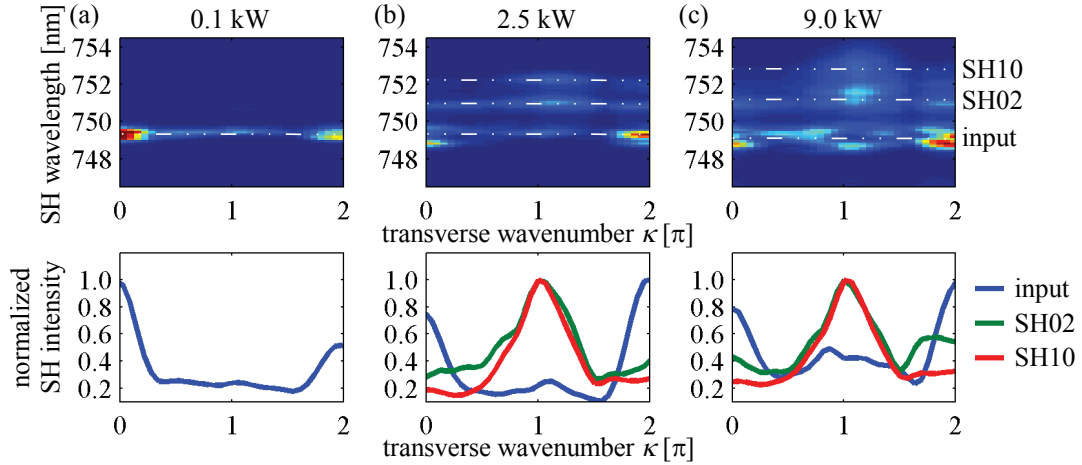


Figure 5.15: Measured spectrally resolved SH spatial spectra for an FW input wavelength of 1499 nm and (a) 0.1 kW, (b) 2.5 kW, and (c) 9 kW FW input peak power. The upper row shows the measured 2D spectra whereas the lower row shows cuts at different wavelengths corresponding to the input wavelength and the phasematching wavelengths to SH02 and SH10. The dash-dotted lines in the upper row mark the wavelengths where the cuts are taken.

will be demonstrated experimentally in the next section to corroborate the simulations.

5.3.2 Experimental demonstration

To realize the spectral measurement capabilities necessary to prove the simulation results described in the preceding section, the same measurement setup as for the integrated measurements in Section 5.2.2 (described in detail in Section 2.4.2) is used. However, instead of a CCD camera we use an imaging spectrograph as the detection instrument in the SH Fourier plane. This allows for the measurement of the SH intensity distribution in dependence on wavelength and transverse wavenumber. With the used instrument a spectral resolution of 0.5 nm is achieved.

Here results obtained for an FW input wavelength of 1499 nm are presented, consistent with the simulated case discussed above. Measurements for different input powers are presented in Fig. 5.15. In Fig. 5.15(a) the input peak power is 0.1 kW, where no nonlinear effects besides mismatched SHG are expected. The measurements show generated SH only at the wavelength of 749.5 nm, corresponding to SH of the FW input wavelength. The lower image of Fig. 5.15(a) shows the SH intensity at this wavelength only, which however is integrated over a spectral domain corresponding to the spectral resolution of 0.5 nm. Clearly the SH is not staggered, as is expected from the simulations and the spectrally integrated experiments. Results for an input power of 2.5 kW are shown in Fig. 5.15(b). This power is above the power necessary to obtain the largest localization of the beam at the array output. Here SH is detected at three distinct wavelengths, where the lowest again corresponds to the exciting FW. The other

distinct wavelengths of 751 nm and 752.3 nm correspond roughly to the phasematching wavelengths of 1501.5 nm and 1503.8 nm to the SH02 and SH10 modes, respectively. Small deviation from the low power phasematching wavelengths are again due to non-linear detuning [77]. The intensity cuts at these wavelengths show, that the SH at the input wavelength is again unstaggered, whereas the SH at the phasematching wavelengths has its maximum at $\kappa' = \pi$. Qualitatively the same result is obtained at an input power of 9 kW in Fig. 5.15(c). Again, SH at both phasematching wavelengths (further shifted) is present and staggered, whereas the maximum intensity at the input wavelength corresponds to unstaggered SH.

The presented experimental result confirm the main result of the analysis of the simulations in Section 5.3.1. Staggered SH is indeed only generated at the phasematching wavelengths, if the input power is larger than necessary for spatial focusing at the array output. Besides the general agreement between simulations and experiments, some discrepancies between the spectral measurements on one hand and the spatio-temporal simulation and the integrated measurements on the other hand exist. First, the SH10 mode, which was almost not recognizable in the simulations, generates also staggered SH with an intensity comparable to the SH02 mode. Also, the SH which is generated at the input wavelength has a much larger intensity than in the simulations. This is visualized in Fig. 5.16(a), where the spectrum integrated over all transverse wavenumbers is presented in dependence on the input power. The measured result is comparable to the simulated data in Fig. 5.13(a), however, with the described deviations. These are linked to the longitudinal inhomogeneity of the sample. This is in principle included in the simulations, but the resolution with which the inhomogeneity is known is in the range of several mm, as is described in detail in Appendix B. Smaller scale inhomogeneities also play an important role in parametric processes, which depend sensitively on the phases of the participating frequency components. Unfortunately, they cannot be experimentally determined for a particular sample. The consequence of the inhomogeneity induced dephasing may be, that a larger amount of the self-phase modulated FW is not transferred to the SH02 but shifted further to the SH10.

To further strengthen this notion a spectrum of the SH at a power of 2.5 kW for a larger spectral range is presented in Fig. 5.16(b). We notice, that SH is not only generated at the SH10 phasematching wavelength, but also at the wavelength corresponding to the SH00 mode. Hence, the frequency conversion of wavelength shifted FW is not as efficient as in the simulation. The self-phase modulation itself is further reinforced by the effective cubic nonlinearity induced by higher order QPM terms mentioned in Section 2.1 [141, 142]. Additionally, the simulations also lack to describe the effects of cascaded interactions with the SH11 and SH00 modes, which are weak, but may produce noticeable effects due to additional phase shifts of the FW00 wave.

The described decreased efficiency of the generation of staggered SH also explains

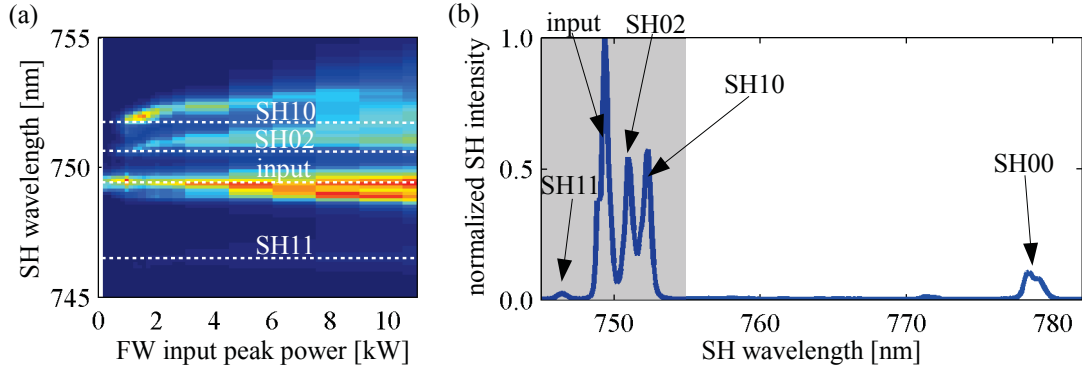


Figure 5.16: (a) Spatially integrated SH output spectra for $\lambda^{\text{FW}} = 1499$ nm in dependence on the FW input peak power. The dotted lines mark the low power phasematching and input wavelengths. (b) Extended SH output spectrum for an input power of 2.5 kW. The gray shading denotes the spectral region already plotted in (a). The labels name the SH modes corresponding to the spectral maxima.

the discrepancies between the integrated and spectrally resolved measurements. For lower input peak power the generated staggered SH is hidden in a background of the broad unstaggered SH maxima generated at the input wavelength and additionally at the phasematching wavelengths to SH00 and SH11 modes.

Chapter summary

The influence of specific properties of higher order SH modes on the nonlinear beam propagation was investigated in this chapter. Thereby the focus was on the linear coupling strength, which was zero in all experiments reported previous to the work conducted in this thesis.

First, discrete solitons were analyzed. Analytically it was shown, that the SH component of a soliton undergoes a power dependent topology transition from unstaggered to staggered if the SH is linearly coupled. This was proved by numerically calculating the corresponding stationary solutions, where the spatial localization was identified as the trigger mechanism for the transition. The SH topology transition was confirmed experimentally by showing a power dependent amount of staggered SH [FS5,FS7,FS11,FS19-22]. The experiments could not excite solitons with staggered SH but revealed, that the transition is a generic property of nonlinear propagation.

The generation of staggered SH in the dynamic experimental situation was studied by conducting detailed simulations of the pulse propagation. It could be shown, that the generation of staggered SH is indeed triggered by a localization of the beams. However, also a spectral reshaping takes place, which results in the output of staggered SH always at the phasematching wavelength of the corresponding SH mode [FS27]. This peculiar feature could be confirmed experimentally by spectrally resolving the spatial SH spectrum [FS8,FS29,FS30].

Chapter 6

Conclusions and Outlook

The aim of this thesis was to establish an understanding of the effects induced by higher order modes on nonlinear beam propagation in WGAs. To achieve this, light propagation in multimode WGAs manufactured by titanium indiffusion in periodically poled lithium niobate was investigated both experimentally and theoretically. These WGAs provide a second-order nonlinearity, which couples light of different frequencies. For the theoretical studies the coupled mode equations were used. They are suitable to describe light dynamics in WGAs under almost all circumstances, given that the linear modes of the waveguides are independent of the effects taken into account to describe the dynamics. It was additionally assumed, that the eigenmodes of the WGA are supermodes, linear superpositions of only one guided mode of the individual waveguides, which requires the bands of the modes to be well separated. Under these assumptions the resulting set of equations could be easily adapted for a simplified analytical treatment or the description of complex experimental circumstances.

For the experimental verification of the theoretically described effects, a flexible experimental apparatus was used. It allowed for the automated control of a larger number of input parameters and for a computer aided collection of all necessary measurements. Pulsed light generated by a unique cw-seeded NOPA system was utilized. The computer controlled beam manipulation system enabled parameter scans of wavelength, input power, and input beam tilt of the beam coupled to the WGA. At the output of the WGA, the powers and spatial profiles of both FW and SH components as well as the spectrally resolved spatial spectrum of the SH were detected.

Weak nonlinear processes in the form of SHG were studied for low input powers. Here the focus was solely on the generation of specific SH modes and its dependence on the input conditions. The SHG process in general was very well understood before the work on this thesis started and the experimental results were mainly used to characterize the higher order SH modes in single waveguides and WGAs. In single waveguides, an exciting FW wave can, in dependence on the input wavelength, be converted to different SH modes. This was shown by means of tuning curve measurements.

The conversion efficiency for each mode follows the well known sinc-dependence on the phase mismatch, leading to a resonance-like generation of SH. The measurement of the mode profiles in the maximum of the SH resonances enabled the adaptation of an analytic model of the waveguide refractive index profile to a particular sample. Thus, the phasematching wavelengths and mode shapes could be obtained by simulations.

SHG in WGAs was described with the same formalism as in the single waveguide. Again, a sinc-dependence of the generation efficiencies was obtained. However, the wavelength of the efficiency maximum in WGAs is not only dependent on the phase-matching wavelength in the single waveguides, but also on the dispersion relations of the interacting waves. These dispersive bands lead to different longitudinal wavenumbers for waves with differing transverse wavenumbers. It was shown experimentally, that the transverse wavenumber of the SH is twice the transverse wavenumber of the FW. The dependence of the phasematching wavelength on the dispersion relations enables the measurement of the SH bands. For this, the FW band has to be known. The measurement procedure was demonstrated experimentally for waveguide arrays with different linear coupling constants. It should be emphasized, that the developed measurement scheme is not restricted to WGAs and can be used in other periodic systems with parametric nonlinearities. Especially photonic crystals with quadratic nonlinearity, which were developed recently [176, 177], could be characterized with the presented approach. For weakly coupled WGAs the linear coupling constant is sufficient to completely determine a band at a fixed wavelength. To measure only these coupling constants of the SH modes, a simplified characterization technique was devised, which relies on only two measurements of the phasematching wavelengths.

For higher input powers, an FW wave can interact with several SH components, even if the phasematching conditions are not fulfilled [77]. In this thesis a simple system of one FW and two SH modes was studied with emphasis on spatial beam reshaping. First, spatial solitons were analyzed analytically in a single waveguide and numerically in WGAs. For each set of phase mismatches between the FW and the SH waves, solitons exist in three parameter ranges of the propagation constant. This is in contrast to solitons with only one SH, where a maximum of two different solution domains can exist. These two existence regions are reproduced for two SH modes, where they are characterized by cumulative action of both parametric interactions. The additional soliton existence region forms due to competition between the two SH components. It is bounded by the linear bands of FW or SH and the propagation constant in the center between the two SH bands. For soliton propagation constants approaching the latter existence boundary, the soliton power goes asymptotically to infinity. This is not possible for solitons with only one SH mode, where the power is always finite for finite propagation constants. However, a similar behavior was shown for discrete solitons with saturable nonlinearities. Hence, the nonlinear competition in a

WGA with two SH modes mimics a saturable system for certain mismatches. In WGAs, regions of mismatches have been identified where competition solitons do not exist and the cumulative solitons bifurcate from the SH bands. Here the power threshold for soliton existence is non-zero, which is not known from systems with only one SH mode. Furthermore, the calculated solitons were probed for instability and several instability mechanisms were identified. Especially solutions close to the competition cut-off are unstable.

Beam propagation with two SH modes was studied experimentally for the interaction of the FW00 mode with the SH02 and SH11 modes. A peculiarity of the experiments was, that only the FW was coupled to the sample. Solitons could only be excited dynamically during the propagation. Nevertheless, the excitation of cumulative solitons bifurcating from the FW bands could be observed. The measured SH mode profiles confirmed, that both SH modes participated in the nonlinear interaction. Unfortunately, competition solitons could not be excited due to sample inhomogeneities. However, a region of mismatches was identified experimentally, where the competition of the SH interactions leads to an inhibition of spatial nonlinear effects. At these mismatches, beams propagate in a quasi-linear regime, showing linear diffraction even for high input powers. This effect may find an application in environments where high powers have to be delivered without beam reshaping.

The influence of the specific properties of higher order modes on the topology of nonlinearly propagating beams was also investigated. The impact of the different parameters of the modes was discussed and the linear coupling constant was identified as being a qualitative difference between first and higher order SH modes. For the tails of spatial solitons it was shown analytically, that the SH component may exist in two different states. For solitons with staggered FW component, the SH tails can switch between the staggered and unstaggered topology, depending on the FW power in the soliton tail. The threshold propagation constant for this transition depends sensitively on the linear coupling constant of the SH mode. For the uncoupled first order SH mode the transition does not take place. The existence of the transition was also verified for numerically obtained spatial solitons, confirming the analytically obtained threshold propagation constants for the soliton tails. However, in the center of odd solitons the transition takes place only for larger coupling constants, whereas it is inhibited completely in the center of even solitons due to symmetry constraints. The numerically calculated intensity profiles allowed for the identification of the localization of the solitons as the trigger mechanism of the topology transition. Furthermore, the analysis of the SH spatial spectra revealed, that the topology transition is accompanied by a shift of the intensity maximum from transverse wavenumbers at the center of the Brillouin zone to the edge of the Brillouin zone. This feature was used for the experimental verification of the effect.

Experiments confirming the topology transition were carried out utilizing the SH02 mode. First, the pulsed output of the WGA was analyzed in a time integrated form. In these experiments, the shift of the SH intensity from the center to the edge of the Brillouin zone could be measured in the spatial spectrum. The difference between odd and even beams could be shown by monitoring the SH spatial spectrum for different input beam symmetries. For even beams the staggered SH vanishes. Although the general predictions for the topology transition were reproduced in the experiments, the measured threshold powers and intensity distributions deviated from simulation results. This was attributed to the shortcomings of the time-integrated measurement technique, which cannot discriminate between the different SH modes present in the experiments.

To clarify the aforementioned discrepancies and to study the specific dynamic effects leading to the topology transition, a detailed analysis of the pulse dynamics in the sample was undertaken. Simulations revealed, that staggered SH is generated due to strong localization of the beams, however, spatial solitons were not excited. This is due to the strong group velocity mismatch between FW and SH components, which impedes the formation of a stable pulse with both FW and SH components. Furthermore, staggered SH is only generated at the phasematching wavelengths. This characteristic effect was confirmed in experiments measuring the spatio-temporal spectra of the SH. In these experiments the same threshold powers for the generation of staggered SH as in the simulations were obtained. Additionally, the experiments showed, that SH modes with very large phase mismatch take part in the nonlinear interaction, which were not taken into account in the simulations.

With the theoretical and experimental work presented in this thesis it was shown, that utilizing higher order SH modes in quadratic WGAs leads to a number of new effects. Although the studies explained here are of a fundamental nature, some of the investigated phenomena have the potential to be used in applications as well. Examples are the bandstructure measuring technique using SHG or the nonlinearity inhibition caused by two SH modes. Additionally, also the SH topology transition may be employed to generate or to switch between specific phase profiles. Effects similar to the described ones may also exist in other discrete systems. The coupled mode equations used to describe the evolution of cw-light in homogeneous WGAs in general describe a set of linearly coupled discrete chains, which interact nonlinearly. Specifically, one chain which corresponds to the FW, is connected by a second order nonlinearity to the other chains and can be regarded as a driving force. Although the specific form of the nonlinear interaction may be different, similar coupled system are expected to exist also in other fields of science.

Future work on the topic discussed in this thesis will be based on the high quality

of the described experimental system, which allows for the experimental investigation of complex nonlinear phenomena. Two different approaches may be considered, which both have promising scientific perspectives.

First, the complexity of the investigated system may be further increased by considering effects which have been neglected in the current thesis. The model of the system could be altered to allow for the description of arbitrary SH modes, including stronger coupled modes and closely spaced bands. This approach would allow for the description of effects resulting from the deviation of the bands from the cos-shape considered in this thesis. Furthermore, nonlinear coupling terms induced by the overlap of FW fields with SH fields in neighboring waveguides have been neglected in this thesis. In specific parameter ranges the inclusion of this term may yield interesting results and yet remains to be explored. Effects stemming from the aforementioned interactions could be easily confirmed experimentally with the existing setup after suitable parameters have been identified theoretically.

Secondly, more complex types of nonlinear excitations, studied only theoretically up to now, could be targeted also experimentally. This includes more exotic stationary solutions like front or twisted solitons [111, 112], which require higher order SH modes. Additionally, also interactions of several solitons as described theoretically in Ref. [101] could be investigated experimentally. To this end, improvements in the excitation scheme are necessary. The continuous excitation by Gaussian beams has to be substituted by an excitation with separate input spots corresponding to the different waveguides. This would enable the separate addressing of intensity and phase in each waveguide, allowing for the mandatory large complexity in the excitation. Practically, this can be achieved by using a spatial light modulator to shape the input beam. Apart from the additional freedom this type of excitation would create, it would further increase the quality of the experimental results by reducing the excitation of unwanted modes.

Finally, also the direct measurement of temporal effects will give additional insight into the light dynamics in WGAs. To realize an efficient spatio-temporal measurement scheme, pulse measurement techniques with spatial resolution and suitable reference laser pulses need to be utilized.

Zusammenfassung

Ziel der vorliegenden Arbeit sind die Untersuchung und das Verständnis von Effekten, welche durch die nichtlineare Propagation geführter Moden höherer Ordnung in evaneszent gekoppelten Wellenleiterarrays ermöglicht werden. Um dies zu erreichen wurde die Lichtausbreitung in mehrmodigen Wellenleiterarrays untersucht, welche durch Eindiffusion von Titan in Lithiumniobat hergestellt wurden. In diesen Wellenleiterarrays koppelt die optische Nichtlinearität zweiter Ordnung ein optisches Feld kleiner Frequenz, die sogenannte Fundamentalwelle, mit dem Feld der zweiten Harmonischen bei der doppelten Frequenz. Für die theoretische Beschreibung der untersuchten Propagationseffekte wurden die gekoppelten Modengleichungen benutzt, welche sowohl analytische Berechnungen als auch die Simulation der Experimente ermöglichen.

Die Anregung von höheren Moden der zweiten Harmonischen aus einer in die Wellenleiter eingekoppelten Fundamentalwelle wurde für geringe Leistungen sowohl in Einzelwellenleitern als auch in Wellenleiterarrays untersucht. Dabei wurde gezeigt, dass höhere Moden unter Berücksichtigung der entsprechenden Phasenanpassbedingungen kontrolliert angeregt werden können. In Wellenleiterarrays ist die Wellenlänge, für welche die Phasenanpassbedingung erfüllt wird, abhängig von der transversalen Wellenzahl der anregenden Fundamentalmode. Dies wurde ausgenutzt, um die Dispersions- und Beugungsrelation der höheren Moden der zweiten Harmonischen zu vermessen.

Im Allgemeinen kann eine propagierende Fundamentalmode mit mehreren Moden der zweiten Harmonischen nichtlinear wechselwirken. In der vorliegenden Arbeit wurde gezeigt, dass diskrete räumliche Solitonen mit zwei verschiedenen Moden der zweiten Harmonischen existieren. Dabei wurden zwei unterschiedliche Typen räumlicher Solitonen identifiziert, in denen die zwei nichtlinearen Wechselwirkungsprozesse miteinander konkurrieren oder sich gegenseitig verstärken. Die Solitonen mit konkurrierenden nichtlinearen Prozessen haben ähnliche Eigenschaften wie diskrete Solitonen in Wellenleiterarrays mit sättigbarer Nichtlinearität. Weiterhin konnte experimentell gezeigt werden, dass für bestimmte Wellenlängen der eingekoppelten Fundamentalmode dynamische räumlich-nichtlineare Effekte durch die konkurrierenden Prozesse unterdrückt werden.

Höhere Moden der zweiten Harmonischen in Wellenleiterarrays haben, im Gegensatz zur Grundmode, eine nichtverschwindende lineare Koppelstärke. In der vorliegenden Arbeit konnte gezeigt werden, dass diese lineare Kopplung der zweiten Harmonischen einen leistungsabhängigen Phasenübergang der diskreten räumlichen Solitonen ermöglicht. Dabei ändert sich, ausgelöst durch einen bestimmten Grad von Lokalisierung, die Topologie der zweiten Harmonischen im Soliton. Dieser Prozess wurde für dynamische Lichtausbreitung experimentell nachgewiesen, sobald räumlich lokalisierte Strahlen erzeugt wurden.

Bibliography

- [1] B. Denardo, B. Galvin, A. Greenfield, A. Larraza, S. Putterman, and W. Wright, “Observations of localized structures in nonlinear lattices: Domain walls and kinks,” *Phys. Rev. Lett.* **68**, 1730–1733 (1992).
- [2] M. Sato, B. E. Hubbard, A. J. Sievers, B. Ilic, D. A. Czaplewski, and H. G. Craighead, “Observation of locked intrinsic localized vibrational modes in a micro-mechanical oscillator array,” *Phys. Rev. Lett.* **90**, 044102 (2003).
- [3] T. Holstein, “Studies of polaron motion: Part I. The molecular-crystal model,” *Annals of Physics* **8**, 325 – 342 (1959).
- [4] A. J. Sievers and S. Takeno, “Intrinsic localized modes in anharmonic crystals,” *Phys. Rev. Lett.* **61**, 970–973 (1988).
- [5] B. I. Swanson, J. A. Brozik, S. P. Love, G. F. Strouse, A. P. Shreve, A. R. Bishop, W.-Z. Wang, and M. I. Salkola, “Observation of intrinsically localized modes in a discrete low-dimensional material,” *Phys. Rev. Lett.* **82**, 3288–3291 (1999).
- [6] B. P. Anderson and M. A. Kasevich, “Macroscopic quantum interference from atomic tunnel arrays,” *Science* **282**, 1686–1689 (1998).
- [7] A. Trombettoni and A. Smerzi, “Discrete solitons and breathers with dilute bose-einstein condensates,” *Phys. Rev. Lett.* **86**, 2353–2356 (2001).
- [8] T. Anker, M. Albiez, R. Gati, S. Hunsmann, B. Eiermann, A. Trombettoni, and M. K. Oberthaler, “Nonlinear self-trapping of matter waves in periodic potentials,” *Phys. Rev. Lett.* **94**, 020403 (2005).
- [9] A. Davydov, “The theory of contraction of proteins under their excitation,” *Journal of Theoretical Biology* **38**, 559 – 569 (1973).
- [10] A. Davydov, *Solitons in molecular systems*, Mathematics and its applications (Kluwer Academic Publishers).: Soviet series (Kluwer Academic Publishers, 1991).
- [11] W. P. Su, J. R. Schrieffer, and A. J. Heeger, “Solitons in polyacetylene,” *Phys. Rev. Lett.* **42**, 1698–1701 (1979).
- [12] P. Marquié, J. M. Bilbault, and M. Remoissenet, “Observation of nonlinear localized modes in an electrical lattice,” *Phys. Rev. E* **51**, 6127–6133 (1995).
- [13] A. Yariv, Y. Xu, R. K. Lee, and A. Scherer, “Coupled-resonator optical waveguide: a proposal and analysis,” *Opt. Lett.* **24**, 711–713 (1999).

- [14] P. Cheo, A. Liu, and G. King, “A high-brightness laser beam from a phase-locked multicore Yb-doped fiber laser array,” *Photonics Technology Letters, IEEE* **13**, 439–441 (2001).
- [15] D. N. Christodoulides and N. K. Efremidis, “Discrete temporal solitons along a chain of nonlinear coupled microcavities embedded in photonic crystals,” *Opt. Lett.* **27**, 568–570 (2002).
- [16] T. Pertsch, P. Dannberg, W. Elflein, A. Bräuer, and F. Lederer, “Optical Bloch oscillations in temperature tuned waveguide arrays,” *Phys. Rev. Lett.* **83**, 4752–4755 (1999).
- [17] H. Trompeter, T. Pertsch, F. Lederer, D. Michaelis, U. Streppel, A. Bräuer, and U. Peschel, “Visual observation of Zener tunneling,” *Phys. Rev. Lett.* **96**, 023901 (2006).
- [18] A. Szameit, I. L. Garanovich, M. Heinrich, A. A. Sukhorukov, F. Dreisow, T. Pertsch, S. Nolte, A. Tünnermann, and Y. S. Kivshar, “Polychromatic dynamic localization in curved photonic lattices,” *Nature Physics* **5**, 271–275 (2009).
- [19] S. Longhi, “Quantum-optical analogies using photonic structures,” *Laser & Photonics Reviews* **3**, 243–261 (2009).
- [20] A. L. Jones, “Coupling of optical fibers and scattering in fibers,” *J. Opt. Soc. Am.* **55**, 261–269 (1965).
- [21] A. Hardy, W. Streifer, and M. Osiński, “Coupled-mode equations for multimode waveguide systems in isotropic or anisotropic media,” *Opt. Lett.* **11**, 742–744 (1986).
- [22] A. A. Sukhorukov, Y. S. Kivshar, O. Bang, and C. M. Soukoulis, “Parametric localized modes in quadratic nonlinear photonic structures,” *Phys. Rev. E* **63**, 016615 (2000).
- [23] P. Yeh, A. Yariv, and C.-S. Hong, “Electromagnetic propagation in periodic stratified media. I. General theory,” *J. Opt. Soc. Am.* **67**, 423–438 (1977).
- [24] P. S. J. Russell, “Optics of Floquet-Bloch waves in dielectric gratings,” *Applied Physics B: Lasers and Optics* **39**, 231–246 (1986).
- [25] A. L. Schawlow and C. H. Townes, “Infrared and optical masers,” *Phys. Rev.* **112**, 1940–1949 (1958).
- [26] T. H. Maiman, “Stimulated optical radiation in ruby,” *Nature* **187**, 493–494 (1960).
- [27] P. A. Franken, A. E. Hill, C. W. Peters, and G. Weinreich, “Generation of optical harmonics,” *Phys. Rev. Lett.* **7**, 118–119 (1961).
- [28] J. A. Armstrong, N. Bloembergen, J. Ducuing, and P. S. Pershan, “Interactions between light waves in a nonlinear dielectric,” *Phys. Rev.* **127**, 1918–1939 (1962).
- [29] T. Y. Chang, “Fast self-induced refractive index changes in optical media: a survey,” *Opt. Eng.* **20**, 220–232 (1981).

- [30] P. Butcher and D. Cotter, *The Elements of Nonlinear Optics*, Cambridge Studies in Modern Optics (Cambridge University Press, 1991).
- [31] P. Yeh, *Introduction to photorefractive nonlinear optics*, Wiley series in pure and applied optics (J. Wiley & Sons, 1993).
- [32] R. Schiek, Y. Baek, G. Krijnen, G. I. Stegeman, I. Baumann, and W. Sohler, “All-optical switching in lithium niobate directional couplers with cascaded non-linearity,” *Opt. Lett.* **21**, 940–942 (1996).
- [33] G. Cerullo and S. D. Silvestri, “Ultrafast optical parametric amplifiers,” *Review of Scientific Instruments* **74**, 1–18 (2003).
- [34] S. Somekh, E. Garmire, A. Yariv, H. Garvin, and R. Hunsperger, “Channel optical waveguide directional couplers,” *Applied Physics Letters* **22**, 46–47 (1973).
- [35] H. Haus and L. Molter-Orr, “Coupled multiple waveguide systems,” *Quantum Electronics, IEEE Journal of* **19**, 840 – 844 (1983).
- [36] H. S. Eisenberg, Y. Silberberg, R. Morandotti, and J. S. Aitchison, “Diffraction management,” *Phys. Rev. Lett.* **85**, 1863–1866 (2000).
- [37] T. Pertsch, T. Zentgraf, U. Peschel, A. Bräuer, and F. Lederer, “Anomalous refraction and diffraction in discrete optical systems,” *Phys. Rev. Lett.* **88**, 093901 (2002).
- [38] D. Mandelik, H. S. Eisenberg, Y. Silberberg, R. Morandotti, and J. S. Aitchison, “Band-gap structure of waveguide arrays and excitation of Floquet-Bloch solitons,” *Phys. Rev. Lett.* **90**, 053902 (2003).
- [39] C. E. Rüter, J. Wisniewski, and D. Kip, “Prism coupling method to excite and analyze Floquet-Bloch modes in linear and nonlinear waveguide arrays,” *Opt. Lett.* **31**, 2768–2770 (2006).
- [40] C. E. Rüter and D. Kip, “Spectroscopy of nonlinear band structures of one-dimensional photonic crystals,” *Phys. Rev. A* **77**, 013818 (2008).
- [41] D. Blömer, A. Szameit, F. Dreisow, T. Schreiber, S. Nolte, and A. Tünnermann, “Nonlinear refractive index of fs-laser-written waveguides in fused silica,” *Opt. Express* **14**, 2151–2157 (2006).
- [42] A. Szameit and S. Nolte, “Discrete optics in femtosecond-laser-written photonic structures,” *Journal of Physics B: Atomic, Molecular and Optical Physics* **43**, 163001 (2010).
- [43] S. Jensen, “The nonlinear coherent coupler,” *Quantum Electronics, IEEE Journal of* **18**, 1580 – 1583 (1982).
- [44] A. A. Maier, “Self-switching of light in a directional coupler,” *Soviet Journal of Quantum Electronics* **14**, 101 (1984).
- [45] S. R. Friberg, Y. Silberberg, M. K. Oliver, M. J. Andrejco, M. A. Saifi, and P. W. Smith, “Ultrafast all-optical switching in a dual-core fiber nonlinear coupler,” *Applied Physics Letters* **51**, 1135 –1137 (1987).

- [46] R. Jin, J. P. Sokoloff, P. A. Harten, C. L. Chuang, S. G. Lee, M. Warren, H. M. Gibbs, N. Peyghambarian, J. N. Polky, and G. A. Pubanz, “Ultrafast modulation with subpicosecond recovery time in a GaAs/AlGaAs nonlinear directional coupler,” *Applied Physics Letters* **56**, 993–995 (1990).
- [47] D. N. Christodoulides and R. I. Joseph, “Discrete self-focusing in nonlinear arrays of coupled waveguides,” *Opt. Lett.* **13**, 794–796 (1988).
- [48] F. Lederer, G. I. Stegeman, D. N. Christodoulides, G. Assanto, M. Segev, and Y. Silberberg, “Discrete solitons in optics,” *Physics Reports* **463**, 1–126 (2008).
- [49] H. S. Eisenberg, Y. Silberberg, R. Morandotti, A. R. Boyd, and J. S. Aitchison, “Discrete spatial optical solitons in waveguide arrays,” *Phys. Rev. Lett.* **81**, 3383–3386 (1998).
- [50] R. Morandotti, U. Peschel, J. S. Aitchison, H. S. Eisenberg, and Y. Silberberg, “Dynamics of discrete solitons in optical waveguide arrays,” *Phys. Rev. Lett.* **83**, 2726–2729 (1999).
- [51] H. S. Eisenberg, R. Morandotti, Y. Silberberg, J. M. Arnold, G. Pennelli, and J. S. Aitchison, “Optical discrete solitons in waveguide arrays. I. Soliton formation,” *J. Opt. Soc. Am. B* **19**, 2938–2944 (2002).
- [52] S. Darmanyan, A. Kobayakov, E. Schmidt, and F. Lederer, “Strongly localized vectorial modes in nonlinear waveguide arrays,” *Phys. Rev. E* **57**, 3520–3530 (1998).
- [53] J. Meier, J. Hudock, D. Christodoulides, G. Stegeman, Y. Silberberg, R. Morandotti, and J. S. Aitchison, “Discrete vector solitons in Kerr nonlinear waveguide arrays,” *Phys. Rev. Lett.* **91**, 143907 (2003).
- [54] R. A. Vicencio, E. Smirnov, C. E. Rüter, D. Kip, and M. Stepić, “Saturable discrete vector solitons in one-dimensional photonic lattices,” *Phys. Rev. A* **76**, 033816 (2007).
- [55] D. Kip, C. E. Rüter, R. Dong, Z. Wang, and J. Xu, “Higher-band gap soliton formation in defocusing photonic lattices,” *Opt. Lett.* **33**, 2056–2058 (2008).
- [56] R. Dong, C. E. Rüter, D. Song, J. Xu, and D. Kip, “Formation of higher-band dark gap solitons in one dimensional waveguide arrays,” *Opt. Express* **18**, 27493–27498 (2010).
- [57] D. Mandelik, H. S. Eisenberg, Y. Silberberg, R. Morandotti, and J. S. Aitchison, “Observation of mutually trapped multiband optical breathers in waveguide arrays,” *Phys. Rev. Lett.* **90**, 253902 (2003).
- [58] R. Pezer, H. Buljan, G. Bartal, M. Segev, and J. W. Fleischer, “Incoherent white-light solitons in nonlinear periodic lattices,” *Phys. Rev. E* **73**, 056608 (2006).
- [59] K. Motzek, A. A. Sukhorukov, and Y. S. Kivshar, “Self-trapping of polychromatic light in nonlinear periodic photonic structures,” *Opt. Express* **14**, 9873–9878 (2006).

- [60] A. A. Sukhorukov, D. N. Neshev, A. Dreischuh, W. Krolikowski, J. Bolger, B. J. Eggleton, L. Bui, A. Mitchell, and Y. S. Kivshar, “Observation of polychromatic gap solitons,” *Opt. Express* **16**, 5991–5996 (2008).
- [61] L. A. Ostrovsky, “Self-action of light in crystals,” *JETP Lett.* **5**, 272 (1967).
- [62] D. N. Klyshko and B. F. Polkovnikov, “Phase modulation and self-modulation of light in three-photon processes,” *Soviet Journal of Quantum Electronics* **3**, 324 (1974).
- [63] G. R. Meredith, “Second-order cascading in third-order nonlinear optical processes,” *The Journal of Chemical Physics* **77**, 5863–5871 (1982).
- [64] A. Kobayakov and F. Lederer, “Cascading of quadratic nonlinearities: An analytical study,” *Phys. Rev. A* **54**, 3455–3471 (1996).
- [65] U. Trutschel, U. Langbein, F. Lederer, and H. Ponath, “Optical bistability in three-wave-mixing processes with guided waves,” *Quantum Electronics, IEEE Journal of* **21**, 1639 – 1643 (1985).
- [66] N. R. Belashenkov, S. V. Gagarski, and M. V. Inochkin, “On the nonlinear light refraction under the 2nd-harmonic generation,” *Opt. Spektrosk* **66**, 1383 (1989).
- [67] H. J. Bakker, P. C. M. Planken, L. Kuipers, and A. Lagendijk, “Phase modulation in second-order nonlinear-optical processes,” *Phys. Rev. A* **42**, 4085–4101 (1990).
- [68] R. DeSalvo, D. J. Hagan, M. Sheik-Bahae, G. Stegeman, E. W. Van Stryland, and H. Vanherzeele, “Self-focusing and self-defocusing by cascaded second-order effects in KTP,” *Opt. Lett.* **17**, 28–30 (1992).
- [69] G. I. Stegeman, M. Sheik-Bahae, E. V. Stryland, and G. Assanto, “Large nonlinear phase shifts in second-order nonlinear-optical processes,” *Opt. Lett.* **18**, 13–15 (1993).
- [70] R. Schiek, “Nonlinear refraction caused by cascaded second-order nonlinearity in optical waveguide structures,” *J. Opt. Soc. Am. B* **10**, 1848–1855 (1993).
- [71] M. L. Sundheimer, C. Bosshard, E. W. V. Stryland, G. I. Stegeman, and J. D. Bierlein, “Large nonlinear phase modulation in quasi-phase-matched KTP waveguides as a result of cascaded second-order processes,” *Opt. Lett.* **18**, 1397–1399 (1993).
- [72] G. Assanto, G. Stegeman, M. Sheik-Bahae, and E. V. Stryland, “All-optical switching devices based on large nonlinear phase shifts from second harmonic generation,” *Applied Physics Letters* **62**, 1323–1325 (1993).
- [73] C. Ironside, J. Aitchison, and J. Arnold, “An all-optical switch employing the cascaded second-order nonlinear effect,” *Quantum Electronics, IEEE Journal of* **29**, 2650 –2654 (1993).
- [74] D. C. Hutchings, J. S. Aitchison, and C. N. Ironside, “All-optical switching based on nondegenerate phase shifts from a cascaded second-order nonlinearity,” *Opt. Lett.* **18**, 793–795 (1993).

- [75] R. Schiek, Y. Baek, and G. I. Stegeman, “Second-harmonic generation and cascaded nonlinearity in titanium-indiffused lithium niobate channel waveguides,” *J. Opt. Soc. Am. B* **15**, 2255–2268 (1998).
- [76] R. Schiek, L. Friedrich, H. Fang, G. I. Stegeman, K. R. Parameswaran, M.-H. Chou, and M. M. Fejer, “Nonlinear directional coupler in periodically poled lithium niobate,” *Opt. Lett.* **24**, 1617–1619 (1999).
- [77] C. G. Trevino-Palacios, G. I. Stegeman, M. P. De Micheli, P. Baldi, S. Nouh, D. B. Ostrowsky, D. Delacourt, and M. Papuchon, “Intensity dependent mode competition in second harmonic generation in multimode waveguides,” *Appl. Phys. Lett.* **67**, 170–172 (1995).
- [78] Y. N. Karamzin and A. P. Sukhorukov, “Mutual focusing of high-power light beams in media with quadratic nonlinearity,” *Soviet Physics JETP* **41**, 414 (1975).
- [79] A. Kanashov and A. Rubenchik, “On diffraction and dispersion effect on three wave interaction,” *Physica D: Nonlinear Phenomena* **4**, 122 – 134 (1981).
- [80] K. Hayata and M. Koshihara, “Multidimensional solitons in quadratic nonlinear media,” *Phys. Rev. Lett.* **71**, 3275–3278 (1993).
- [81] M. J. Werner and P. D. Drummond, “Simulton solutions for the parametric amplifier,” *J. Opt. Soc. Am. B* **10**, 2390–2393 (1993).
- [82] A. V. Buryak and Y. S. Kivshar, “Spatial optical solitons governed by quadratic nonlinearity,” *Opt. Lett.* **19**, 1612–1614 (1994).
- [83] L. Torner, C. R. Menyuk, and G. I. Stegeman, “Excitation of solitons with cascaded $\chi(2)$ nonlinearities,” *Opt. Lett.* **19**, 1615–1617 (1994).
- [84] A. V. Buryak and Y. S. Kivshar, “Solitons due to second harmonic generation,” *Physics Letters A* **197**, 407 – 412 (1995).
- [85] A. A. Sukhorukov, “Approximate solutions and scaling transformations for quadratic solitons,” *Phys. Rev. E* **61**, 4530–4539 (2000).
- [86] W. E. Torruellas, Z. Wang, D. J. Hagan, E. W. VanStryland, G. I. Stegeman, L. Torner, and C. R. Menyuk, “Observation of two-dimensional spatial solitary waves in a quadratic medium,” *Phys. Rev. Lett.* **74**, 5036–5039 (1995).
- [87] B. Bourliaguet, V. Couderc, A. Barthélémy, G. W. Ross, P. G. R. Smith, D. C. Hanna, and C. D. Angelis, “Observation of quadratic spatial solitons in periodically poled lithium niobate,” *Opt. Lett.* **24**, 1410–1412 (1999).
- [88] R. Schiek, Y. Baek, and G. I. Stegeman, “One-dimensional spatial solitary waves due to cascaded second-order nonlinearities in planar waveguides,” *Phys. Rev. E* **53**, 1138–1141 (1996).
- [89] D. V. Skryabin and W. J. Firth, “Generation and stability of optical bullets in quadratic nonlinear media,” *Optics Communications* **148**, 79 – 84 (1998).

- [90] D. Mihalache, D. Mazilu, B. A. Malomed, and L. Torner, “Asymmetric spatiotemporal optical solitons in media with quadratic nonlinearity,” *Optics Communications* **152**, 365 – 370 (1998).
- [91] B. A. Malomed, P. Drummond, H. He, A. Berntson, D. Anderson, and M. Lisak, “Spatiotemporal solitons in multidimensional optical media with a quadratic nonlinearity,” *Phys. Rev. E* **56**, 4725–4735 (1997).
- [92] L. Torner, S. Carrasco, J. P. Torres, L.-C. Crasovan, and D. Mihalache, “Tandem light bullets,” *Optics Communications* **199**, 277 – 281 (2001).
- [93] L. Torner, C. R. Menyuk, and G. I. Stegeman, “Bright solitons with second-order nonlinearities,” *J. Opt. Soc. Am. B* **12**, 889–897 (1995).
- [94] L. Torner, D. Mazilu, and D. Mihalache, “Walking solitons in quadratic nonlinear media,” *Phys. Rev. Lett.* **77**, 2455–2458 (1996).
- [95] C. Etrich, U. Peschel, F. Lederer, and B. A. Malomed, “Stability of temporal chirped solitary waves in quadratically nonlinear media,” *Phys. Rev. E* **55**, 6155–6161 (1997).
- [96] A. D. Capobianco, B. Costantini, C. De Angelis, A. L. Palma, and G. F. Nallessio, “Role of walk-off in solitary-wave propagation in materials with quadratic nonlinearity,” *J. Opt. Soc. Am. B* **14**, 2602–2609 (1997).
- [97] D. Mihalache, D. Mazilu, L.-C. Crasovan, L. Torner, B. A. Malomed, and F. Lederer, “Three-dimensional walking spatiotemporal solitons in quadratic media,” *Phys. Rev. E* **62**, 7340–7347 (2000).
- [98] S. Carrasco, J. P. Torres, L. Torner, and F. W. Wise, “Walk-off acceptance for quadratic soliton generation,” *Optics Communications* **191**, 363 – 370 (2001).
- [99] X. Liu, L. J. Qian, and F. W. Wise, “Generation of optical spatiotemporal solitons,” *Phys. Rev. Lett.* **82**, 4631–4634 (1999).
- [100] O. Bang, P. L. Christiansen, and C. B. Clausen, “Stationary solutions and self-trapping in discrete quadratic nonlinear systems,” *Phys. Rev. E* **56**, 7257–7266 (1997).
- [101] T. Peschel, U. Peschel, and F. Lederer, “Discrete bright solitary waves in quadratically nonlinear media,” *Phys. Rev. E* **57**, 1127–1133 (1998).
- [102] S. Darmanyan, A. Kobayakov, and F. Lederer, “Strongly localized modes in discrete systems with quadratic nonlinearity,” *Phys. Rev. E* **57**, 2344–2349 (1998).
- [103] H. Susanto, R. L. Horne, N. Whitaker, and P. G. Kevrekidis, “Plane waves and localized modes in quadratic waveguide arrays,” *Physical Review A* **77**, 033805 (2008).
- [104] P. D. Miller and O. Bang, “Macroscopic dynamics in quadratic nonlinear lattices,” *Phys. Rev. E* **57**, 6038–6049 (1998).

- [105] R. Iwanow, R. Schiek, G. I. Stegeman, T. Pertsch, F. Lederer, Y. Min, and W. Sohler, “Observation of discrete quadratic solitons,” *Phys. Rev. Lett.* **93**, 113902 (2004).
- [106] R. Iwanow, G. I. Stegeman, R. Schiek, T. Pertsch, F. Lederer, Y. Min, and W. Sohler, “Highly localized discrete quadratic solitons,” *Opt. Lett.* **30**, 1033–1035 (2005).
- [107] B. A. Malomed, P. G. Kevrekidis, D. J. Frantzeskakis, H. E. Nistazakis, and A. N. Yannacopoulos, “One- and two-dimensional solitons in second-harmonic-generating lattices,” *Phys. Rev. E* **65**, 056606 (2002).
- [108] Z. Xu, Y. V. Kartashov, L.-C. Crasovan, D. Mihalache, and L. Torner, “Spatiotemporal discrete multicolor solitons,” *Phys. Rev. E* **70**, 066618 (2004).
- [109] Y. S. Kivshar and D. K. Campbell, “Peierls-Nabarro potential barrier for highly localized nonlinear modes,” *Phys. Rev. E* **48**, 3077–3081 (1993).
- [110] D. Cai, A. R. Bishop, and N. Grønbech-Jensen, “Localized states in discrete nonlinear Schrödinger equations,” *Phys. Rev. Lett.* **72**, 591–595 (1994).
- [111] A. Kobayakov, S. Darmanyan, T. Pertsch, and F. Lederer, “Stable discrete domain walls and quasi-rectangular solitons in quadratically nonlinear waveguide arrays,” *J. Opt. Soc. Am. B* **16**, 1737–1742 (1999).
- [112] Z. Xu and A. A. Sukhorukov, “Spatial-spectral vortex solitons in quadratic lattices,” *Opt. Lett.* **34**, 1168–1170 (2009).
- [113] G. I. Stegeman, D. J. Hagan, and L. Torner, “ $\chi(2)$ cascading phenomena and their applications to all-optical signal processing, mode-locking, pulse compression and solitons,” *Optical and Quantum Electronics* **28**, 1691–1740 (1996).
- [114] A. V. Buryak, P. D. Trapani, D. V. Skryabin, and S. Trillo, “Optical solitons due to quadratic nonlinearities: from basic physics to futuristic applications,” *Phys. Reports* **370**, 63 – 235 (2002).
- [115] F. Lederer and Y. Silberberg, “Discrete solitons,” *Opt. Photon. News* **13**, 48–53 (2002).
- [116] A. Sukhorukov, Y. Kivshar, H. Eisenberg, and Y. Silberberg, “Spatial optical solitons in waveguide arrays,” *Quantum Electronics, IEEE Journal of* **39**, 31 – 50 (2003).
- [117] D. N. Christodoulides, F. Lederer, and Y. Silberberg, “Discretizing light behaviour in linear and nonlinear waveguide lattices,” *Nature* **424**, 817–823 (2003).
- [118] Y. V. Kartashov, B. A. Malomed, and L. Torner, “Solitons in nonlinear lattices,” *Rev. Mod. Phys.* **83**, 247–306 (2011).
- [119] V. V. Konotop, M. D. Cunha, P. L. Christiansen, and C. B. Clausen, “Three-wave interaction in two-component quadratic nonlinear lattices,” *Phys. Rev. E* **60**, 6104–6110 (1999).

- [120] J. R. Pierce, “Coupling of modes of propagation,” *Journal of Applied Physics* **25**, 179–183 (1954).
- [121] E. A. J. Marcatili, “Dielectric rectangular waveguide and directional coupler for integrated optics,” *Bell Systems Technical Journal* **48**, 2071–2102 (1969).
- [122] A. Yariv, “Coupled-mode theory for guided-wave optics,” *Quantum Electronics, IEEE Journal of* **9**, 919–933 (1973).
- [123] H. Taylor and A. Yariv, “Guided wave optics,” *Proceedings of the IEEE* **62**, 1044–1060 (1974).
- [124] D. Marcuse, *Light transmission optics*, Van Nostrand Reinhold electrical/computer science and engineering series (Van Nostrand Reinhold, 1982).
- [125] H. Haus and W. Huang, “Coupled-mode theory,” *Proceedings of the IEEE* **79**, 1505–1518 (1991).
- [126] T. Pertsch, “Discrete localization in linear and nonlinear optical waveguide arrays,” Ph.D. thesis, Friedrich-Schiller-Universität Jena (2003).
- [127] A. Snyder and J. Love, *Optical waveguide theory*, Science paperbacks (Chapman and Hall, 1983).
- [128] G. Agrawal, *Nonlinear fiber optics*, Optics and Photonics (Academic Press, 2007).
- [129] W. Karthe and R. Müller, *Integrierte Optik*, Technisch-physikalische Monographien (Geest & Portig, 1991).
- [130] K. S. Chiang, “Review of numerical and approximate methods for the modal analysis of general optical dielectric waveguides,” *Optical and Quantum Electronics* **26**, S113–S134 (1994).
- [131] G. Dahlquist and Å. Björck, *Numerical methods*, Dover Books on Mathematics (Dover Publications, 2003).
- [132] S. Johnson and J. Joannopoulos, “Block-iterative frequency-domain methods for maxwell’s equations in a planewave basis,” *Opt. Express* **8**, 173–190 (2001).
- [133] T. Tamir and R. Alferness, *Guided-wave optoelectronics*, Springer series in electronics and photonics (Springer, 1988).
- [134] M. Börner, R. Müller, R. Schiek, and G. Trommer, *Elemente der integrierten Optik* (Teubner, 1990).
- [135] B. E. A. Saleh and M. C. Teich, *Fundamentals of photonics* (Wiley, New York [u.a.], 1991).
- [136] J. Manley and H. Rowe, “Some general properties of nonlinear elements-part I. General energy relations,” *Proceedings of the IRE* **44**, 904–913 (1956).
- [137] R. S. Weis and T. K. Gaylord, “Lithium niobate: Summary of physical properties and crystal structure,” *Applied Physics A: Materials Science & Processing* **37**, 191–203 (1985).

- [138] R. Schiek and T. Pertsch, “Absolute measurement of the quadratic nonlinear susceptibility of lithium niobate in waveguides,” *Opt. Mater. Express* **2**, 126–139 (2012).
- [139] R. Sutherland, D. McLean, and S. Kirkpatrick, *Handbook of nonlinear optics*, Optical engineering (Marcel Dekker, 2003).
- [140] M. Houe and P. D. Townsend, “An introduction to methods of periodic poling for second-harmonic generation,” *Journal of Physics D: Applied Physics* **28**, 1747 (1995).
- [141] C. B. Clausen, O. Bang, and Y. S. Kivshar, “Spatial solitons and induced Kerr effects in quasi-phase-matched quadratic media,” *Phys. Rev. Lett.* **78**, 4749–4752 (1997).
- [142] A. Kobayakov, F. Lederer, O. Bang, and Y. S. Kivshar, “Nonlinear phase shift and all-optical switching in quasi-phase-matched quadratic media,” *Opt. Lett.* **23**, 506–508 (1998).
- [143] C. De Angelis, F. Gringoli, and G. Nalesso, “Multiple scale analysis of quasi-phase-matched quadratic dielectrics for second harmonic generation,” *Optical and Quantum Electronics* **33**, 1149–1161 (2001).
- [144] A. Hardy and W. Streifer, “Analysis of phased-array diode lasers,” *Opt. Lett.* **10**, 335–337 (1985).
- [145] A. Hardy and W. Streifer, “Coupled mode theory of parallel waveguides,” *Lightwave Technology, Journal of* **3**, 1135 – 1146 (1985).
- [146] A. Hardy and W. Streifer, “Coupled modes of multiwaveguide systems and phased arrays,” *Lightwave Technology, Journal of* **4**, 90 – 99 (1986).
- [147] A. Hardy and W. Streifer, “Coupled mode solutions of multiwaveguide systems,” *Quantum Electronics, IEEE Journal of* **22**, 528 – 534 (1986).
- [148] Y. Shama, A. Hardy, and E. Marom, “Multimode coupling of unidentical waveguides,” *Lightwave Technology, Journal of* **7**, 420 – 425 (1989).
- [149] N. K. Efremidis, S. Sears, D. N. Christodoulides, J. W. Fleischer, and M. Segev, “Discrete solitons in photorefractive optically induced photonic lattices,” *Phys. Rev. E* **66**, 046602 (2002).
- [150] P. Kevrekidis, B. Malomed, A. Saxena, A. Bishop, and D. Frantzeskakis, “Higher-order lattice diffraction: solitons in the discrete NLS equation with next-nearest-neighbor interactions,” *Physica D: Nonlinear Phenomena* **183**, 87 – 101 (2003).
- [151] R. Iyer, J. S. Aitchison, J. Wan, M. M. Dignam, and C. M. de Sterke, “Exact dynamic localization in curved AlGaAs optical waveguide arrays,” *Opt. Express* **15**, 3212–3223 (2007).
- [152] F. Dreisow, A. Szameit, M. Heinrich, T. Pertsch, S. Nolte, and A. Tünnermann, “Second-order coupling in femtosecond-laser-written waveguide arrays,” *Opt. Lett.* **33**, 2689–2691 (2008).

- [153] C. Minot, N. Belabas, J. A. Levenson, and J.-M. Moison, “Analytical first-order extension of coupled-mode theory for waveguide arrays,” *Opt. Express* **18**, 7157–7172 (2010).
- [154] *TSL210F - Full band tunable semiconductor laser*. Operation manual, Santec Corporation.
- [155] W. Miniscalco, “Erbium-doped glasses for fiber amplifiers at 1500 nm,” *Lightwave Technology, Journal of* **9**, 234–250 (1991).
- [156] P. Becker, N. Olsson, and J. Simpson, *Erbium-doped fiber amplifiers: fundamentals and technology*, no. Bd. 1 in *Optics and photonics* (Academic Press, 1999).
- [157] R. Baumgartner and R. Byer, “Optical parametric amplification,” *Quantum Electronics, IEEE Journal of* **15**, 432–444 (1979).
- [158] M. Breuer, C. Homann, and E. Riedle, *Noncollinear optical parametric amplification of cw light, continua and vacuum fluctuations* (Springer Berlin Heidelberg, 2009), vol. 92 of *Springer Series in Chemical Physics*, pp. 771–773.
- [159] G. M. Gale, M. Cavallari, T. J. Driscoll, and F. Hache, “Sub-20-fs tunable pulses in the visible from an 82-MHz optical parametric oscillator,” *Opt. Lett.* **20**, 1562–1564 (1995).
- [160] T. Wilhelm, J. Piel, and E. Riedle, “Sub-20-fs pulses tunable across the visible from a blue-pumped single-pass noncollinear parametric converter,” *Opt. Lett.* **22**, 1494–1496 (1997).
- [161] G. M. Gale, M. Cavallari, and F. Hache, “Femtosecond visible optical parametric oscillator,” *J. Opt. Soc. Am. B* **15**, 702–714 (1998).
- [162] M. Fiebig, V. V. Pavlov, and R. V. Pisarev, “Second-harmonic generation as a tool for studying electronic and magnetic structures of crystals: review,” *J. Opt. Soc. Am. B* **22**, 96–118 (2005).
- [163] G. Schreiber, H. Suche, Y. Lee, W. Grundkötter, V. Quiring, R. Ricken, and W. Sohler, “Efficient cascaded difference frequency conversion in periodically poled Ti:LiNbO₃ waveguides using pulsed and cw pumping,” *Applied Physics B: Lasers and Optics* **73**, 501–504 (2001).
- [164] R. Iwanow, R. Schiek, G. Stegeman, T. Pertsch, F. Lederer, Y. Min, and W. Sohler, “Arrays of weakly coupled, periodically poled lithium niobate waveguides: beam propagation and discrete spatial quadratic solitons,” *Opto-Electronics Review* **13**, 113 (2005).
- [165] W. Sohler, H. Hu, R. Ricken, V. Quiring, C. Vannahme, H. Herrmann, D. Büchter, S. Reza, W. Grundkötter, S. Orlov, H. Suche, R. Nouroozi, and Y. Min, “Integrated optical devices in lithium niobate,” *Opt. Photon. News* **19**, 24–31 (2008).
- [166] G. P. Bava, I. Montrosset, W. Sohler, and H. Suche, “Numerical modeling of Ti:LiNbO₃ integrated optical parametric oscillators,” *IEEE J. Quant. Elect.* **23**, 42 (1987).

- [167] E. Strake, G. Bava, and I. Montrosset, “Guided modes of Ti:LiNbO₃ channel waveguides: a novel quasi-analytical technique in comparison with the scalar finite-element method,” *J. Lightwave Technol.* **6**, 1126 (1988).
- [168] D. Kip, B. Gather, H. Bendig, and E. Krätzig, “Concentration and refractive index profiles of titanium- and iron-diffused planar LiNbO₃ waveguides,” *physica status solidi (a)* **139**, 241–248 (1993).
- [169] M. Fukuma, J. Noda, and H. Iwasaki, “Optical properties in titanium-diffused Ti:LiNbO₃ strip waveguides,” *Journal of Applied Physics* **49**, 3693–3698 (1978).
- [170] W. K. Burns, P. H. Klein, E. J. West, and L. E. Plew, “Ti diffusion in Ti:LiNbO₃ planar and channel optical waveguides,” *J. Appl. Phys.* **50**, 6175 (1979).
- [171] R. Schiek, “Diffusionskonstanten in Ti:LiNbO₃,” (2001). Internal ROSA report.
- [172] G. J. Edwards and M. Lawrence, “A temperature-dependent dispersion equation for congruently grown lithium niobate,” *Optical and Quantum Electronics* **16**, 373–375 (1984).
- [173] R. W. Boyd, *Nonlinear Optics* (Academic Press, 2008), 3rd ed.
- [174] A. Szameit, T. Pertsch, F. Dreisow, S. Nolte, A. Tünnermann, U. Peschel, and F. Lederer, “Light evolution in arbitrary two-dimensional waveguide arrays,” *Phys. Rev. A* **75**, 053814 (2007).
- [175] M. Roussey, M.-P. Bernal, N. Courjal, and F. I. Baida, “Experimental and theoretical characterization of a lithium niobate photonic crystal,” *Applied Physics Letters* **87**, 241101 (2005).
- [176] K. Rivoire, Z. Lin, F. Hatami, W. T. Masselink, and J. Vučković, “Second harmonic generation in gallium phosphide photonic crystal nanocavities with ultralow continuous wave pump power,” *Opt. Express* **17**, 22609–22615 (2009).
- [177] R. Geiss, S. Diziain, R. Iliew, C. Etrich, H. Hartung, N. Janunts, F. Schrepel, F. Lederer, T. Pertsch, and E.-B. Kley, “Light propagation in a free-standing lithium niobate photonic crystal waveguide,” *Applied Physics Letters* **97**, 131109 (2010).
- [178] S. Fan, I. Appelbaum, and J. D. Joannopoulos, “Near-field scanning optical microscopy as a simultaneous probe of fields and band structure of photonic crystals: A computational study,” *Applied Physics Letters* **75**, 3461–3463 (1999).
- [179] D. Labilloy, H. Benisty, C. Weisbuch, C. J. M. Smith, T. F. Krauss, R. Houdré, and U. Oesterle, “Finely resolved transmission spectra and band structure of two-dimensional photonic crystals using emission from inas quantum dots,” *Phys. Rev. B* **59**, 1649–1652 (1999).
- [180] N. L. Thomas, R. Houdré, M. V. Kotlyar, D. O’Brien, and T. F. Krauss, “Exploring light propagating in photonic crystals with fourier optics,” *J. Opt. Soc. Am. B* **24**, 2964–2971 (2007).

- [181] G. Assanto and G. Stegeman, “Simple physics of quadratic spatial solitons,” *Opt. Express* **10**, 388–396 (2002).
- [182] N. I. Nikolov, D. Neshev, O. Bang, and W. Z. Królikowski, “Quadratic solitons as nonlocal solitons,” *Phys. Rev. E* **68**, 036614 (2003).
- [183] Y. S. Kivshar, “Self-localization in arrays of defocusing waveguides,” *Opt. Lett.* **18**, 1147–1149 (1993).
- [184] J. W. Fleischer, T. Carmon, M. Segev, N. K. Efremidis, and D. N. Christodoulides, “Observation of discrete solitons in optically induced real time waveguide arrays,” *Phys. Rev. Lett.* **90**, 023902 (2003).
- [185] M. Stepić, D. Kip, L. Hadžievski, and A. Maluckov, “One-dimensional bright discrete solitons in media with saturable nonlinearity,” *Phys. Rev. E* **69**, 066618 (2004).
- [186] Y. S. Kivshar and G. Agrawal, *Optical Solitons: From Fibers to Photonic Crystals* (Academic Press, 2003), 1st ed.
- [187] N. G. Vakhitov and A. A. Kolokolov, “Stationary solutions of the wave equation in a medium with nonlinearity saturation,” *Radiophysics and Quantum Electronics* **16**, 783–789 (1973).
- [188] A. A. Sukhorukov and Y. S. Kivshar, “Nonlinear localized waves in a periodic medium,” *Phys. Rev. Lett.* **87**, 083901 (2001).
- [189] D. E. Pelinovsky, A. A. Sukhorukov, and Y. S. Kivshar, “Bifurcations and stability of gap solitons in periodic potentials,” *Phys. Rev. E* **70**, 036618 (2004).
- [190] D. E. Pelinovsky, A. V. Buryak, and Y. S. Kivshar, “Instability of solitons governed by quadratic nonlinearities,” *Phys. Rev. Lett.* **75**, 591–595 (1995).
- [191] S. Darmanyan, A. Kobayakov, F. Lederer, and L. Vázquez, “Discrete fronts and quasirectangular solitons,” *Phys. Rev. B* **59**, 5994–5997 (1999).
- [192] F. H. Bennet, T. J. Alexander, F. Haslinger, A. Mitchell, D. N. Neshev, and Y. S. Kivshar, “Observation of nonlinear self-trapping of broad beams in defocusing waveguide arrays,” *Phys. Rev. Lett.* **106**, 093901 (2011).
- [193] L. Torner, J. P. Torres, D. Artigas, D. Mihalache, and D. Mazilu, “Soliton content with quadratic nonlinearities,” *Optics Communications* **164**, 153 – 159 (1999).
- [194] J. T. Manassah, “Effects of velocity dispersion on a generated second harmonic signal,” *Appl. Opt.* **27**, 4365–4367 (1988).
- [195] L. D. Noordam, H. J. Bakker, M. P. de Boer, and H. B. van Linden van den Heuvell, “Second-harmonic generation of femtosecond pulses: observation of phase-mismatch effects,” *Opt. Lett.* **15**, 1464–1466 (1990).
- [196] F. Baronio, A. Barthelémy, S. Carrasco, V. Couderc, C. De Angelis, L. Lefort, Y. Min, P. H. Pioger, V. Quiring, L. Torner, and W. Sohler, “Generation of quadratic spatially trapped beams with short pulsed light,” *Journal of Optics B: Quantum and Semiclassical Optics* **6**, 182–189 (2004).

- [197] S. Carrasco, J. P. Torres, D. Artigas, and L. Torner, “Generation of multicolor spatial solitons with pulsed light,” *Optics Communications* **192**, 347–355 (2001).
- [198] P. Pioger, V. Couderc, L. Lefort, A. Barthelemy, F. Baronio, C. De Angelis, Y. Min, V. Quiring, and W. Sohler, “Spatial trapping of short pulses in ti-indiffused LiNbO₃ waveguides,” *Opt. Lett.* **27**, 2182–2184 (2002).
- [199] I. V. Shadrivov and A. A. Zharov, “Dynamics of optical spatial solitons near the interface between two quadratically nonlinear media,” *J. Opt. Soc. Am. B* **19**, 596–602 (2002).
- [200] C. Conti, M. Peccianti, and G. Assanto, “Route to nonlocality and observation of accessible solitons,” *Phys. Rev. Lett.* **91**, 073901 (2003).
- [201] P. V. Larsen, M. P. Sørensen, O. Bang, W. Z. Królikowski, and S. Trillo, “Non-local description of X waves in quadratic nonlinear materials,” *Phys. Rev. E* **73**, 036614 (2006).
- [202] M. I. Molina, R. A. Vicencio, and Y. S. Kivshar, “Two-color discrete localized modes and resonant scattering in arrays of nonlinear quadratic optical waveguides,” *Phys. Rev. E* **72**, 036622 (2005).
- [203] M. J. D. Powell, *A fortran subroutine for solving systems of non-linear algebraic equations* (Gordon and Breach Science Publishers, 1970), chap. 7.
- [204] P. Di Trapani, A. Bramati, S. Minardi, W. Chinaglia, C. Conti, S. Trillo, J. Kilius, and G. Valiulis, “Focusing versus defocusing nonlinearities due to parametric wave mixing,” *Phys. Rev. Lett.* **87**, 183902 (2001).
- [205] A. A. Sukhorukov, D. N. Neshev, and Y. S. Kivshar, “Shaping and control of polychromatic light in nonlinear photonic lattices,” *Opt. Express* **15**, 13058–13076 (2007).
- [206] L. Torner and E. M. Wright, “Soliton excitation and mutual locking of light beams in bulk quadratic nonlinear crystals,” *J. Opt. Soc. Am. B* **13**, 864–875 (1996).
- [207] E. López-Lago, C. Simos, V. Couderc, A. Barthélémy, D. Artigas, and L. Torner, “Efficiency of quadratic soliton generation,” *Opt. Lett.* **26**, 1277–1279 (2001).
- [208] S. Carrasco, L. Torner, J. Torres, D. Artigas, E. Lopez-Lago, V. Couderc, and A. Barthelemy, “Quadratic solitons: existence versus excitation,” *Selected Topics in Quantum Electronics, IEEE Journal of* **8**, 497–505 (2002).
- [209] W. Press, S. Teukolsky, W. Vetterling, and B. Flannery, *Numerical Recipes in C* (Cambridge University Press, Cambridge, UK, 1992), 2nd ed.
- [210] T. Kaiser, D. Flamm, S. Schröter, and M. Duparré, “Complete modal decomposition for optical fibers using CGH-based correlation filters,” *Opt. Express* **17**, 9347–9356 (2009).
- [211] G. Bosman, *Ultrashort optical pulse characterization* (University of Stellenbosch, 2008).

- [212] F. Eilenberger, S. Minardi, A. Szameit, U. Röpke, J. Kobelke, K. Schuster, H. Bartelt, S. Nolte, L. Torner, F. Lederer, A. Tünnermann, and T. Pertsch, “Evolution dynamics of discrete-continuous light bullets,” *Phys. Rev. A* **84**, 013836 (2011).
- [213] C. Simos, V. Couderc, and A. Barthelemy, “Temporal reshaping of optical pulses using quadratic spatial soliton generation and spatial filtering,” *Photonics Technology Letters, IEEE* **14**, 636–638 (2002).
- [214] S. Droulias, K. Hizanidis, J. Meier, and D. Christodoulides, “X - waves in nonlinear normally dispersive waveguide arrays,” *Opt. Express* **13**, 1827–1832 (2005).
- [215] Y. Lahini, E. Frumker, Y. Silberberg, S. Droulias, K. Hizanidis, R. Morandotti, and D. N. Christodoulides, “Discrete X-wave formation in nonlinear waveguide arrays,” *Phys. Rev. Lett.* **98**, 023901 (2007).
- [216] M. Heinrich, A. Szameit, F. Dreisow, R. Keil, S. Minardi, T. Pertsch, S. Nolte, A. Tünnermann, and F. Lederer, “Observation of three-dimensional discrete-continuous X waves in photonic lattices,” *Phys. Rev. Lett.* **103**, 113903 (2009).
- [217] R. Schiek, R. Iwanow, T. Pertsch, G. I. Stegeman, G. Schreiber, and W. Sohler, “One-dimensional spatial soliton families in optimally engineered quasi-phase-matched lithium niobate waveguides,” *Opt. Lett.* **29**, 596–598 (2004).
- [218] M. Marangoni, C. Manzoni, R. Ramponi, G. Cerullo, F. Baronio, C. De Angelis, and K. Kitamura, “Group-velocity control by quadratic nonlinear interactions,” *Opt. Lett.* **31**, 534–536 (2006).
- [219] F. Baronio, C. De Angelis, M. Marangoni, C. Manzoni, R. Ramponi, and G. Cerullo, “Spectral shift of femtosecond pulses in nonlinear quadratic ppslt crystals,” *Opt. Express* **14**, 4774–4779 (2006).
- [220] C. Conti and S. Trillo, “X waves generated at the second harmonic,” *Opt. Lett.* **28**, 1251–1253 (2003).
- [221] O. Jedrkiewicz, J. Trull, G. Valiulis, A. Piskarskas, C. Conti, S. Trillo, and P. Di Trapani, “Nonlinear X waves in second-harmonic generation: Experimental results,” *Phys. Rev. E* **68**, 026610 (2003).
- [222] G. Valiulis, V. Jukna, O. Jedrkiewicz, M. Clerici, E. Rubino, and P. DiTrapani, “Propagation dynamics and X-pulse formation in phase-mismatched second-harmonic generation,” *Phys. Rev. A* **83**, 043834 (2011).

List of own publications

Journal publications

- [FS1] M. Augustin, R. Iliew, C. Etrich, F. Setzpfandt, H.-J. Fuchs, E.-B. Kley, S. Nolte, T. Pertsch, F. Lederer, and A. Tünnermann, “Dispersion properties of photonic crystal waveguides with a low in-plane index contrast,” *New Journal of Physics* **8**, 210 (2006).
- [FS2] F. Garwe, C. Rockstuhl, C. Etrich, U. Hübner, U. Bauerschäfer, F. Setzpfandt, M. Augustin, T. Pertsch, A. Tünnermann, and F. Lederer, “Evaluation of gold nanowire pairs as a potential negative index material,” *Applied Physics B* **84**, 139 (2006).
- [FS3] F. Setzpfandt, D. N. Neshev, R. Schiek, F. Lederer, A. Tünnermann, and T. Pertsch, “Competing nonlinearities in quadratic nonlinear waveguide arrays,” *Opt. Lett.* **34**, 3589–3591 (2009).
- [FS4] E. Pshenay-Severin, F. Setzpfandt, C. Helgert, U. Hübner, C. Menzel, A. Chipouline, C. Rockstuhl, A. Tünnermann, F. Lederer, and T. Pertsch, “Experimental determination of the dispersion relation of light in metamaterials by white-light interferometry,” *J. Opt. Soc. Am. B* **27**, 660–666 (2010).
- [FS5] F. Setzpfandt, A. A. Sukhorukov, D. N. Neshev, R. Schiek, Y. S. Kivshar, and T. Pertsch, “Phase transitions of nonlinear waves in quadratic waveguide arrays,” *Phys. Rev. Lett.* **105**, 233905 (2010).
- [FS6] O. Kashin, M. Homann, V. Matusevich, F. Setzpfandt, T. Pertsch, and R. Kowarschik, “Change of the refractive index in PPLN waveguides due to the photorefractive effect,” *Applied Physics B: Lasers and Optics* **104**, 547 (2011).
- [FS7] F. Setzpfandt, D. N. Neshev, A. A. Sukhorukov, R. Schiek, R. Ricken, Y. Min, Y. S. Kivshar, W. Sohler, F. Lederer, A. Tünnermann, and T. Pertsch, “Nonlinear dynamics with higher-order modes in lithium niobate waveguide arrays,” *Applied Physics B: Lasers and Optics* **104**, 487–493 (2011).
- [FS8] F. Setzpfandt, A. A. Sukhorukov, D. N. Neshev, R. Schiek, A. S. Solntsev, R. Ricken, Y. Min, W. Sohler, Y. S. Kivshar, and T. Pertsch, “Spectral pulse transformations and phase transitions in quadratic nonlinear waveguide arrays,” *Opt. Express* **19**, 23188–23201 (2011).
- [FS9] F. Setzpfandt, A. A. Sukhorukov, and T. Pertsch, “Discrete quadratic solitons with competing second-harmonic components,” *Phys. Rev. A* **84**, 053843 (2011).

- [FS10] M. C. Rechtsman, Y. V. Kartashov, F. Setzpfandt, H. Trompeter, L. Torner, T. Pertsch, U. Peschel, and A. Szameit, “Negative Goos–Hänchen shift in periodic media,” *Opt. Lett.* **36**, 4446–4448 (2011).

Invited talks in international conferences

- [FS11] T. Pertsch and F. Setzpfandt, “Spatial nonlinear effects with higher order modes in LiNbO₃ waveguide arrays,” in “Nonlinear Photonics (NLP), 2011 International Workshop,” (2011), invited.

Contributions to international conferences

- [FS12] F. Garwe, C. Rockstuhl, C. Etrich, U. Hübner, U. Bauerschäfer, F. Setzpfandt, M. Augustin, T. Pertsch, A. Tünnermann, and F. Lederer, “Engineering resonances in nanorod left-handed metamaterials,” in “Conference on Lasers and Electro-Optics and 2006 Quantum Electronics and Laser Science Conference. CLEO/QELS 2006.”, (2006).
- [FS13] F. Garwe, C. Rockstuhl, C. Etrich, U. Hübner, U. Bauerschäfer, F. Setzpfandt, M. Augustin, A. Chipouline, T. Pertsch, and F. Lederer, “Towards a negative index material using pairs of nanowires,” in “Photonic Metamaterials: From Random to Periodic,” (Optical Society of America, 2006), TuC6.
- [FS14] F. Garwe, C. Rockstuhl, C. Etrich, M. Augustin, F. Setzpfandt, U. Hübner, J. Bergmann, U. Bauerschäfer, U. Peschel, T. Pertsch, and F. Lederer, “Configurations of elongated gold nanostructures on silica as metamaterials: theory, technology, and optical properties,” (SPIE, 2006), vol. 6195, p. 61950H.
- [FS15] R. Geiss, H. Hartung, R. Iliew, T. Gischkat, F. Schrepel, F. Setzpfandt, T. Pertsch, E.-B. Kley, F. Lederer, W. Wesch, and A. Tünnermann, “Radiation losses of photonic crystal waveguides in LiNbO₃ Membranes,” in “Nonlinear Optics: Materials, Fundamentals and Applications,” (Optical Society of America, 2009), NMD2.
- [FS16] F. Setzpfandt, R. Schiek, R. Geiss, W. Sohler, A. Tünnermann, and T. Pertsch, “Discrete quadratic solitons with higher order modes in lithium niobate waveguide arrays,” in “Nonlinear Optics: Materials, Fundamentals and Applications,” (Optical Society of America, 2009), NMB6.
- [FS17] F. Setzpfandt, D.N. Neshev, R. Schiek, F. Lederer, A. Tünnermann, and T. Pertsch, “Observation of competing quadratic nonlinearities in lithium niobate waveguide arrays,” in “Australasian Conference on Optics, Lasers and Spectroscopy and Australian Conference on Optical Fibre Technology (ACOFT),” (2009).

- [FS18] E. Pshenay-Severin, F. Setzpfandt, C. Helgert, U. Hübner, C. Menzel, C. Rockstuhl, A. Tünnermann, F. Lederer, and T. Pertsch, “Direct experimental optical characterization of metamaterials,” in “2nd International Conference on Metamaterials, Photonic crystals and Plasmonics,” (2010).
- [FS19] F. Setzpfandt, A. A. Sukhorukov, D. N. Neshev, R. Schiek, A. Tünnermann, and T. Pertsch, “Phase transition of discrete quadratic solitons,” in “Conference on Lasers and Electro-Optics (CLEO) and the Quantum Electronics and Laser Science Conference (QELS),” (Optical Society of America, 2010), QTuC1.
- [FS20] F. Setzpfandt, A. A. Sukhorukov, D. N. Neshev, R. Schiek, A. Tünnermann, Y. S. Kivshar, and T. Pertsch, “Multiband quadratic solitons in waveguide arrays,” in “Nonlinear Photonics,” (Optical Society of America, 2010), NWC7.
- [FS21] F. Setzpfandt, A.A. Sukhorukov, D.N. Neshev, R. Schiek, Y.S. Kivshar, and T. Pertsch, “Phase transitions of nonlinear waves in lithium niobate waveguide arrays,” in “Optical Fibre Technology (ACOFT), 2010 35th Australian Conference on,” (2010).
- [FS22] A. A. Sukhorukov, F. Setzpfandt, D. N. Neshev, R. Schiek, A. Tünnermann, Y. S. Kivshar, and T. Pertsch, “Properties of discrete quadratic multiband solitons,” in “The 2nd international conference: Nonlinear waves – Theory and applications,” (2010).
- [FS23] F. Eilenberger, S. Minardi, F. Setzpfandt, and T. Pertsch, “Superluminally decaying light bullets in periodic media,” in “Nonlinear Optics: Materials, Fundamentals and Applications,” (Optical Society of America, 2011), NThB6.
- [FS24] E. Pshenay-Severin, A. Chipouline, J. Petschulat, U. Hübner, F. Eilenberger, F. Setzpfandt, T. Pertsch, and A. Tünnermann, “Magnetic properties of asymmetric double-wire structures,” in “Quantum Electronics and Laser Science Conference,” (Optical Society of America, 2011), QTuD7.
- [FS25] F. Setzpfandt, A. A. Sukhorukov, and T. Pertsch, “Solitons in waveguide arrays with competing quadratic nonlinearities,” in “CLEO/Europe and EQEC 2011 Conference Digest,” (Optical Society of America, 2011), EFP7.
- [FS26] F. Setzpfandt, M. Falkner, R. Schiek, F. Eilenberger, E. Pshenay-Severin, and T. Pertsch, “Bandstructure measurements of lithium niobate waveguide arrays,” in “Quantum Electronics and Laser Science Conference,” (Optical Society of America, 2011), QMD3.

- [FS27] F. Setzpfandt, A. A. Sukhorukov, D. N. Neshev, R. Schiek, A. S. Solntsev, Y. S. Kivshar, and T. Pertsch, “Nonlinear pulse transformation and phase transitions in LiNbO_3 waveguide arrays,” in “CLEO/Europe and EQEC 2011 Conference Digest,” (Optical Society of America, 2011).
- [FS28] F. Setzpfandt, A. A. Sukhorukov, D. N. Neshev, R. Schiek, A. S. Solntsev, F. Eilenberger, S. Minardi, R. Ricken, Y. Min, W. Sohler, Y. S. Kivshar, and T. Pertsch, “Nonlinear evolution of laser pulses in lithium niobate waveguide arrays,” in “Nonlinear Optics: Materials, Fundamentals and Applications,” (Optical Society of America, 2011), NThB7.
- [FS29] F. Setzpfandt, A. A. Sukhorukov, and T. Pertsch, “Discrete solitons with competing second harmonic components in lithium niobate waveguide arrays,” in “Nonlinear Optics: Materials, Fundamentals and Applications,” (Optical Society of America, 2011), NWE17.
- [FS30] F. Setzpfandt, A. A. Sukhorukov, D. N. Neshev, R. Schiek, A. S. Solntsev, R. Ricken, Y. Min, W. Sohler, Y. S. Kivshar, and T. Pertsch, “Spatio-temporal dynamics of laser pulses in lithium niobate waveguide arrays,” in “IQEC / CLEO Pacific Rim Conference Digest,” (Australian Optical Society, 2011), pp. 3660–CT–2.

Appendix A

Symbols and conventions

Symbols

A^μ	normalized slowly varying amplitude
A_0^μ	amplitude of stationary solutions
A_+^μ, A_-^μ	amplitude of perturbations to stationary solutions
α^μ	damping of waveguide mode μ
$\bar{\alpha}^\mu$	normalized damping of waveguide mode μ
b	propagation constant of stationary solution
B_0	compensation propagation constant for soliton solutions
β_0	propagation constant of waveguide mode μ at frequency ω_0
$\beta_{\text{lin}}^\mu(z)$	linear detuning of waveguide mode μ
β^μ	propagation constant of waveguide mode μ
c^μ	coupling constant of mode μ
C_{mix}	intermode coupling constant
C^μ	normalized coupling constant of mode μ
c_0	speed of light in vacuum
$\chi^{(2)}$	2nd order susceptibility tensor
χ_{eff}^ν	effective susceptibility of interaction with SH mode ν
d	pitch of the waveguide array
D^μ	group velocity dispersion of mode μ
\bar{D}^μ	normalized group velocity dispersion of mode μ
$\Delta\beta^\nu$	phase mismatch of interaction with SH mode ν
$\Delta\hat{\epsilon}$	spatial inhomogeneity defining a waveguide
δ^ν	group velocity mismatch between FW mode and SH mode ν
$\bar{\delta}^\nu$	normalized group velocity mismatch between FW mode and SH mode ν
Δ^ν	normalized phase mismatch of interaction with SH mode ν
$\Delta\hat{\epsilon}$	refractive index change defining single waveguide
$\Delta\hat{\epsilon}_n$	refractive index change defining n th waveguide in WGA
$\Delta\mathbf{P}$	perturbation of polarization vector \mathbf{P}
$\Delta\bar{\mathbf{P}}$	slowly varying envelope of the perturbing polarization
D_x, D_y	diffusion constants of titanium in lithium niobate
\mathbf{E}, \mathbf{H}	electric field vector, magnetic field vector
$\mathbf{e}_{\text{array}}$	electric field profile of array supermode
\mathbf{e}^μ	electric field profile of waveguide mode μ
\mathbf{e}_0^μ	electric field profile of waveguide mode μ at frequency ω_0

$\hat{\epsilon}$	dielectric tensor of medium
ϵ_0	electric permittivity of vacuum
f_e	dispersion factor of waveguide refractive index profile
F_e	concentration constant of waveguide refractive index profile
Γ	effective cascaded nonlinearity
γ^ν	normalized nonlinearity
\mathbf{H}_{ext}	external field exciting a waveguide
k^μ	longitudinal wave number of mode μ in waveguide array
K	nonlinear overlap integral
κ^μ	transverse wave number of mode μ in waveguide array
L	sample length
λ	wavelength of electric field
λ_{PM}	phasematching wavelength
λ_{rel}	wavelength relative to input fundamental wavelength
Λ^{QPM}	period of phase-matching grating
μ_0	magnetic permeability of vacuum
μ	index running over all waveguide modes at any frequency
n	waveguide number
N	number of waveguides in waveguide array
n_{eff}^μ	effective refractive index of mode μ
$n_{\text{ndeg}}^{\text{FW}}$	combined effective index of two FW modes
n_{QPM}^ν	effective index of SH mode ν accounting for periodic poling
ν	index running over all waveguide modes with SH frequency
ω	radial frequency of electric field
ω_0	center frequency of narrow spectrum
ω_σ	frequency of induced polarization
\mathbf{P}	polarization vector
P_0	power to normalize mode profiles
Φ	amplitude in ansatz for linear multimode coupling
φ^μ	fast varying amplitude of mode μ
Ψ	relative averaged nonlinearity
\mathbf{r}, x, y, z	coordinate vector in space, Cartesian coordinates
r_{Ti}	thickness of titanium stripe
ρ	concentration of titanium after indiffusion
ρ_0	concentration of titanium at origin
σ	perturbation in propagation constant of stationary solutions
T_0	normalization timespan
τ	normalized time in moving time frame
u^μ	slowly varying amplitude of waveguide mode μ , $u^\mu(z, t) = \varphi^\mu(z, t) \exp(-i\beta_0 z)$
v_g^μ	group velocity of mode μ
w_{Ti}	width of titanium stripe
ξ	index running over all waveguide modes with FW frequency
\bar{z}	normalized propagation distance
Z_0	normalization length

Conventions

x^*	complex conjugate of x
$\Re(x)$	real part of x
$\Im(x)$	imaginary part of x
c.c.	complex conjugate of preceding term
\tilde{x}	Fourier transform of x
\mathbf{x}	x is a vector
\hat{x}	x is a tensor
\mathbf{x}_t	transverse components of \mathbf{x}

Appendix B

Sample characterization

In this thesis, the coupled mode equations were used to describe light propagation in WGAs. In this formalism, the properties of the investigated sample are reduced to a number of scalar coefficients. The precise knowledge of the magnitude of these coefficients is crucial if experimental result should be explained with the help of simulations. To achieve this knowledge, a number of techniques have been used to measure the coefficients connected to the different effects taken into account. These methods, which have been known before the work on this thesis begun, are described in the following.

Diffusion constants

The diffusion constants of titanium in lithium niobate in the x - and y -directions, D_x and D_y , do not directly appear in the coupled mode equations. However, they are crucial in describing the refractive index profile of the waveguides, which is needed for simulation of the modal dispersion. The refractive index profile is governed by the titanium concentration [166–168]

$$\rho(x, y) = \frac{1}{2}\rho_0 \left(\operatorname{erf} \left[\frac{w_{\text{Ti}}}{2D_x} \left(1 + \frac{2x}{w_{\text{Ti}}} \right) \right] + \operatorname{erf} \left[\frac{w_{\text{Ti}}}{2D_x} \left(1 - \frac{2x}{w_{\text{Ti}}} \right) \right] \right) \exp \left(-\frac{y^2}{D_y^2} \right), \quad (\text{B.1})$$

as already explained in Section 3.1.1. Here $\rho_0 = 6.412 \cdot 10^{22} \text{ cm}^{-3} d_{\text{Ti}}/D_y$ is the concentration at the surface of the substrate with the thickness of the titanium stripe r_{Ti} . w_{Ti} is the width of the titanium stripe. Thickness and width are known from the manufacturing process. The diffusion coefficients need to be determined in every sample. This is not possible directly. Instead, FW and SH mode profiles of a single waveguide are measured. From the captured images the widths of the modes in x - and y -direction are determined. These parameters are compared with the corresponding values of mode profiles simulated with a certain set of diffusion constants. To calculate the modes, FEM or the Plane Wave Expansion method are employed. The mode calculations are repeated with iterative changes of the diffusion constants until agreement

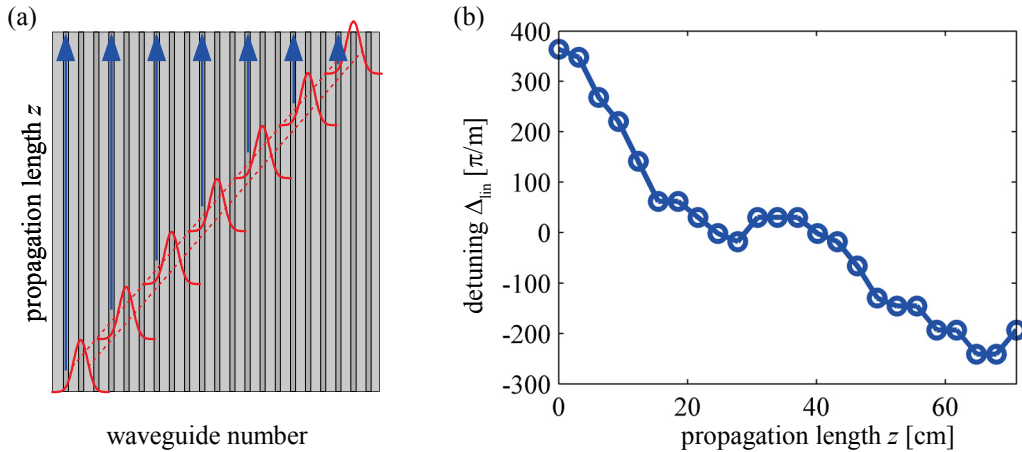


Figure B.1: (a) Scheme of the measurement. The FW beam is shown in red, the SH signal is denoted by the blue arrows. (b) Measured longitudinal inhomogeneity for the sample used for the experiments presented in Chapter 4 and Chapter 5. The circles represent the measured detuning in the different waveguides, the connecting line is just a guide to the eye.

between measured and simulated modes is achieved.

Sample inhomogeneity

To enable simulations which quantitatively agree with measurement results, it is necessary to know the longitudinal sample inhomogeneities $\Delta_{\text{lin}}^{\mu}$. These are induced by the sample fabrication and by the inhomogeneous temperature profile of the sample oven. To measure the inhomogeneity profile, the peculiar properties of the WGA diffraction relation are utilized. For transverse wavenumbers $\kappa^{\text{FW}} = \pm 0.5\pi$, the transverse velocity of the beam has its maximum whereas the diffraction coefficient vanishes [37]. Hence beams can propagate across the WGA without diffraction as sketched in Fig. B.1(a). In each waveguide the FW beam nonlinearly interacts with the SH. This interaction takes place at a defined longitudinal position due to the FW transverse velocity. In the measurements, the interaction with the uncoupled SH00 mode is used. To measure the inhomogeneity, the FW wavelength is swept and the SH power at each waveguide output is measured. The resulting tuningcurves have their maximum at the wavelength where the mismatch in the interaction region vanishes. Hence, from comparing the phasematching wavelengths in the different waveguides an information about the longitudinal change of the phasematching is derived. Here it is assumed that the WGA is homogeneous in the transverse direction. The measured changes in the phasematching wavelengths can be converted in detunings if the dispersion of FW and SH is known. In the data used here, the dispersion of bulk lithium niobate [172] has been used to calculate the dependence of the phase mismatch on the detuning. However, the measurement scheme can not distinguish between detunings $\Delta_{\text{lin}}^{\text{FW}}$ of the FW

and $\Delta_{\text{lin}}^{\text{SH}}$ of the SH. In the simulations discussed in this thesis, the measured detuning has always been attributed to the SH components. The measured detuning for the sample used in Chapter 4 and Chapter 5 is shown in Fig. B.1(b). Additionally it was assumed, that this detuning is the same for all SH modes.

Dispersion coefficients

To determine the modal dispersion, FEM calculations of the modes for different frequencies are utilized. The specific refractive index profile of the sample under investigation and the known dispersion of bulk lithium niobate are taken into account. These calculations result in the mode propagation constants $\beta^\mu(\omega)$. To calculate the dispersion coefficients for the frequency ω_0 , the Taylor-expansion

$$\beta^\mu(\omega) \approx \beta_0^\mu + \frac{1}{v_g^\mu}(\omega - \omega_0) + \frac{D^\mu}{2}(\omega - \omega_0)^2. \quad (\text{B.2})$$

with the coefficients

$$\beta_0^\mu = \beta^\mu(\omega_0), \quad \frac{1}{v_g^\mu} = \left. \frac{\partial \beta^\mu}{\partial \omega} \right|_{\omega_0}, \quad \text{and} \quad D^\mu = \left. \frac{\partial^2 \beta^\mu}{\partial \omega^2} \right|_{\omega_0}. \quad (\text{B.3})$$

is fitted to the propagation constants. Here v_g^μ is the group velocity and D^μ the group velocity dispersion (GVD) of the mode μ . The results for the coefficients of group velocity and GVD are precisely determined by this method, as is evidenced in Section 3.2.3. However, the propagation constant β_0^μ of the modes depends very sensitively on the mode profile. The error in the determination of the mode profile leads to errors in the simulated phasematching wavelength, which are in the range of a few nm. Especially for simulations of processes involving several SH modes this is not sufficient. Here one of the SH mode propagation constants is adjusted to comply with the measured differences in the phasematching wavelengths of the SH interactions.

Effective nonlinearity

The effective nonlinear coefficient in the coupled mode equations depend on the nonlinear susceptibility of bulk lithium niobate and on the nonlinear overlap of the participating FW and SH modes. The former value is known from the literature [138]. The latter coefficient is different for the various SH modes and is determined utilizing tuning curve measurements. To this end the SH power in single waveguide is measured precisely in dependence on the FW wavelengths. These results are then compared to simulation results, where the nonlinear overlap in the simulation is adjusted iteratively until agreement is achieved. The simulations take into account losses and the longitudinal inhomogeneity of the sample.

Coupling constants

To determine the linear coupling coefficients, two different methods are employed for the FW and SH. For the FW, only the coupling constant of the fundamental band was obtained by measuring the Greens function of the WGA. To this end, a single waveguide of the WGA with length L is excited and the discrete diffraction pattern at the output is recorded. The output amplitudes at the output obey [20, 174]

$$u_{n,n'}^\mu(L) = i^{n-n'} J_{n-n'}(2c^\mu L), \quad (\text{B.4})$$

as was explained in Section 4.1. Here n and n' denote the excited and observed waveguide, respectively and $J_{n-n'}$ is the Bessel function of the first kind of $(n - n')$ th order. To determine the FW coupling constant, Eq. (B.4) is fitted to the measured output amplitudes. This scheme is repeated for every desired wavelength.

The SH coupling constants cannot be obtained in the described way, since a specific mode cannot be linearly excited by excitation from the end-face of the sample in a reproducible fashion. For the measurement of these coupling constants the procedure outlined in Section 3.2.3 is used, which relies on nonlinear excitation of certain SH bands by SHG.

Appendix C

Acknowledgements

A work like this is not possible without contributions from many people. I only succeeded because of the support and the ideas of the persons surrounding me. For this I would like to thank

- Prof. Thomas Pertsch for allowing me to work on this topic, for always having an open ear to problems and asking the right questions, and for creating a surrounding which made work fun.
- Prof. Roland Schiek for sharing all the secrets of the experimental work in lithium niobate waveguides, for teaching me patience and precision, and for widening my view on the science world.
- Dr. Dragomir N. Neshev for helping me in turning results into science, for opening my eyes to many new ideas, and for giving me the opportunity to work in his labs.
- Dr. Andrey A. Sukhorukov for teaching me some theoretical basics and not giving up in the process and for showing me how to connect equations and measurement results.
- Prof. Wolfgang Sohler and his co-workers for putting such effort into the fabrication of the samples, this work would not have been possible without the exceptional quality of the waveguide arrays.
- Matthias Falkner, Alexander S. Solntsev, and Pilar Rodriguez for lending me a hand in performing specific measurement tasks.

- Falk Eilenberger, Reinhard Geiss, Thomas Kaiser, Dr. Ekaterina A. Pshenay-Severin and Carsten Schmidt for proofreading of this work and providing many valuable comments.
- All my colleagues, who were always helpful and enthusiastic to share their thoughts and ideas on almost everything (portable black holes included).
- Katja for enriching my life in countless ways and for always doing the right thing.
- My parents for not asking too much what strange things I am doing all that years.
- Everybody I may have forgotten unintentionally

Appendix D

Curriculum Vitae

Name: Frank Setzpfandt
Date of birth: 31.10.1981
Place of birth: Oranienburg
Nationality: German

EDUCATION

since 03/2006 Ph.d. student at the Institute of Applied Physics,
Friedrich-Schiller-Universität Jena, Germany.
10/2000 - 12/2005 Physikalisch-Astronomische Fakultät,
Friedrich-Schiller-Universität Jena.

DEGREES

12/2005 Dipl.-Phys.,
Title of Diploma thesis: 'Development of a measurement scheme to evaluate the dispersion relation of photonic crystal waveguides'.

EMPLOYMENT

since 01/2006 scientific assistant at the Institute of Applied Physics,
Friedrich-Schiller-Universität Jena, Germany.

Appendix E

Ehrenwörtliche Erklärung

Ich erkläre hiermit ehrenwörtlich, dass ich die vorliegende Arbeit selbständig, ohne unzulässige Hilfe Dritter und ohne Benutzung anderer als der hier genannten Hilfsmittel und Literatur angefertigt habe. Die aus anderen Quellen direkt oder indirekt übernommenen Daten und Konzepte sind unter Angabe der Quellen gekennzeichnet. Die Arbeit wurde bisher weder in In- noch im Ausland in gleicher oder ähnlicher Form einer anderen Prüfungsbehörde vorgelegt. Die geltende Promotionsordnung der Physikalisch - Astronomischen Fakultät ist mir bekannt. Ich versichere ehrenwörtlich, dass ich nach bestem Wissen die reine Wahrheit gesagt und nichts verschwiegen habe.

Jena, 28.03.2012

Frank Setzpfandt